

Re-submitted November, 2006 for ApJ

**The young stellar population in M17 revealed by *Chandra***Patrick S. Broos<sup>1\*</sup>, Eric D. Feigelson<sup>1</sup>, Leisa K. Townsley<sup>1</sup>, Konstantin V. Getman<sup>1</sup>, Junfeng Wang<sup>1</sup>,  
Gordon P. Garmire<sup>1</sup>, Zhibo Jiang<sup>2</sup>, Yohko Tsuboi<sup>3</sup>**ABSTRACT**

We report here results from a *Chandra* ACIS observation of the stellar populations in and around the Messier 17 HII region. The field reveals 886 sources with observed X-ray luminosities (uncorrected for absorption) between  $\sim 29.3 < \log L_x < 32.8$  ergs s<sup>-1</sup>, 771 of which have stellar counterparts in infrared images. In addition to comprehensive tables of X-ray source properties, several results are presented:

1. The X-ray Luminosity Function is calibrated to that of the Orion Nebula Cluster population to infer a total population of roughly 8000–10,000 stars in M17, one-third lying in the central NGC 6618 cluster.
2. About 40% of the ACIS sources are heavily obscured with  $A_V > 10$  mag. Some are concentrated around well-studied star-forming regions—IRS 5/UC1, the Kleinmann-Wright Object, and M17-North—but most are distributed across the field. As previously shown, star formation appears to be widely distributed in the molecular clouds. X-ray emission is detected from 64 of the hundreds of Class I protostar candidates that can be identified by near- and mid-infrared colors. These constitute the most likely protostar candidates known in M17.
3. The spatial distribution of X-ray stars is complex: in addition to the central NGC 6618 cluster and well-known embedded groups, we find a new embedded cluster (designated M17-X), a 2 pc-long arc of young stars along the southwest edge of the M17 HII region, and 0.1 pc substructure within various populations. These structures may indicate that the populations are dynamically young.
4. All (14/14) of the known O stars but only about half (19/34) of the known B0–B3 stars in the M17 field are detected. These stars exhibit the long-reported correlation between X-ray and bolometric luminosities of  $L_x \sim 10^{-7} L_{bol}$ . While many O and early B stars show the soft X-ray emission expected from microshocks in their winds or moderately hard emission that could be caused by magnetically channeled wind shocks, six of these stars exhibit very hard thermal plasma components ( $kT > 4$  keV) that may be due to colliding wind binaries. More than 100 candidate new OB stars are found, including 28 X-ray detected intermediate- and high-mass protostar candidates with infrared excesses.

---

\*Send requests to P. Broos at patb@astro.psu.edu.

<sup>1</sup>Department of Astronomy & Astrophysics, 525 Davey Laboratory, Pennsylvania State University, University Park, PA 16802

<sup>2</sup>Purple Mountain Observatory, National Astronomical Observatories, Chinese Academy of Sciences, 2 Beijing Xi Lu, Nanjing, Jiangsu 210008, China

<sup>3</sup>Department of Physics, Faculty of Science and Engineering, Chuo University, 1-13-27 Kasuga, Bunkyo-ku, Tokyo 112-8551, Japan

5. Only a small fraction (perhaps 10%) of X-ray selected high- and intermediate-mass stars exhibit  $K$ -band emitting protoplanetary disks, providing further evidence that inner disks evolve very rapidly around more massive stars.

*Subject headings:* open clusters and associations: individual (M17) — X-rays: individual (M17)  
 — stars: early-type — stars: pre-main-sequence — X-Rays: stars

## 1. Introduction

In the last 30 years, most observational studies of the stellar denizens of massive star-forming regions (MSFRs) were based on broadband visual photometry, supplemented by occasional visual spectroscopy of the most massive cluster members, and near-infrared (NIR) photometry of small regions ( $< 10'$ ) situated on the cluster cores. In a few visually obscured regions this was augmented by NIR spectroscopy of the brightest OB cluster members. The surrounding HII regions and molecular clouds were often well-studied in radio/millimeter wavelengths, including arcminute-scale maps of molecular line emission and arcsecond-scale maps of continuum structures. More recently, heated dust structures have been mapped in the mid-infrared (MIR) with space-based instruments on the *Midcourse Space Experiment (MSX)* (e.g. Kraemer et al. 2003) and the *Spitzer Space Telescope* (e.g. Churchwell et al. 2004; Allen et al. 2005).

In the high-energy regime, lower-mass young stars in nearby star-forming regions were studied extensively with X-ray missions during the 1980-90s (Feigelson & Montmerle 1999), but studies of the more distant MSFRs were hampered by the limited spatial resolution of these telescopes. The launch of the *Chandra X-ray Observatory* (Weisskopf et al. 2002) in 1999 makes X-ray studies of MSFRs much more feasible, due to the sub-arcsecond spatial resolution of its mirrors, their high reflectivity at shorter wavelengths that penetrate interstellar absorption, and the excellent noise characteristics of its primary imaging camera, the Advanced CCD Imaging Spectrometer (ACIS). High-resolution X-ray images of MSFRs can reveal a complex menagerie of hundreds of stellar sources (protostars, pre-main sequence stars, and OB/Wolf-Rayet stars) and diffuse structures such as wind-swept bubbles, superbubbles, chimneys, and supernova remnants (see review by Feigelson et al. 2006). X-ray selected samples are surprisingly advantageous for uncovering the stellar populations of young clusters. By studying a number of these fields with varying ages and stellar content with *Chandra*, we hope to characterize these stellar populations and to learn more about the origins of any diffuse X-ray emission that may be present. Some of the most recent *Chandra* MSFR studies include NGC 6193 (Skinner et al. 2005), NGC 6334 (Ezoe et al. 2006), 30 Doradus (Townsend et al. 2006a,b), Cepheus B/OB3b (Getman et al. 2006a), RCW 38 (Wolk et al. 2006), Westerlund 1 (Skinner et al. 2006; Muno et al. 2006b), W 49A (Tsujimoto et al. 2006), and NGC 6357 (Wang et al. 2006). These studies all show rich stellar populations, many uniquely revealed by the high-resolution *Chandra* observations.

These X-ray observations are complementary to high-resolution IR imaging data from 2MASS, *Spitzer*, and modern ground-based facilities. We have shown that *Chandra* observations of Galactic MSFRs are not strongly contaminated by X-ray sources that are not cluster members; in a typical *Chandra* observation of a cluster around 1 – 2 kpc distant, simulations and data show that only a handful of foreground stars and background active galactic nuclei (AGN) are present ( $\sim 5\%$  of the X-ray sources), while hundreds of cluster members are revealed (Getman et al. 2005a, 2006a; Wang et al. 2006). These X-ray detections can be used to identify cluster members for further IR study without the usual selection by IR excess. This provides a disk-unbiased sample for further IR study, at least for lower-mass T Tauri (pre-main sequence) stars. X-ray observations also are not hampered by the confusion due to bright dust and gas emission that plagues IR

and visual studies of HII regions. X-rays are often the only way to detect fainter cluster members along ionization fronts or in the vicinity of bright OB stars.

Here we present the first high-spatial-resolution X-ray point source study of M17 ( $\Leftrightarrow$  W 38  $\Leftrightarrow$  S 45  $\Leftrightarrow$  RCW 160  $\Leftrightarrow$  the Omega Nebula), a famous and spectacular nearby MSFR (Figure 1). M17 is a blister HII region at the northeast edge of one of the largest giant molecular clouds in the Galaxy, with an extent of  $4^\circ$  ( $\sim 110$  pc, Elmegreen et al. 1979). The local geometry resembles the Orion Nebula HII region except that it is viewed edge-on rather than face-on (Meixner et al. 1992). Molecular material is concentrated in a clumpy structure known as M17-SW. Active star formation is concentrated in three molecular cores (Figure 1a): around the ultracompact HII region M17-UC1 and its associated masers, the double B star known as the Kleinmann-Wright Object (KWO) and its associated cluster (Chini et al. 2004a), and the protostars in M17-North. Historically, their proximity to the HII region was attributed to sequential triggering of star formation (Elmegreen & Lada 1977), although this link has been challenged for M17-SW by Wilson et al. (2003), who note that the KWO is too far from the OB cluster and too evolved for its formation to have been caused by the cluster. The clumpy molecular structure of the cloud (Figure 1b) and infrared protostars indicate that star formation is still in progress all around the HII region (Jiang et al. 2002; Wilson et al. 2003; Chini et al. 2005; Reid & Wilson 2006).

NGC 6618, the central cluster that illuminates M17, has 100 stars earlier than B9 (Lada et al. 1991); for comparison, Orion has a dozen. Several obscured O4-O5 stars form a central  $1'$  ring and are principally responsible for ionizing the nebula (Hanson, Howarth, & Conti 1997). NGC 6618 is estimated to be no more than 1 Myr old; this extreme youth and the absence of evolved stars in the region give good circumstantial evidence that we are seeing this cluster before its first supernova, making M17 an ideal place to study the interactions of massive stars with their environment and stellar disks before they are affected by nearby supernovae. We give a more extensive description of past observations of M17 and NGC 6618 in our earlier analysis of this *Chandra* observation, which focused on the diffuse X-ray emission produced by the cluster OB winds (Townesley et al. 2003, henceforth TFM03).

Distance estimates for M17 range from 1.3 kpc (Hanson, Howarth, & Conti 1997) to 2.2 kpc (Chini, Elsaesser, & Neckel 1980). A thorough study by Nielbock et al. (2001) gives a distance of  $1.6 \pm 0.3$  kpc; we adopt this value here. This is consistent with TFM03 and with the NIR study of Jiang et al. (2002), whose data are used in this paper.

The present *Chandra* study is based on a 40 ks pointing with the ACIS camera in March 2002; this is the same dataset analyzed by TFM03. This image locates over 800 stellar X-ray sources in the NGC 6618 cluster and cloud population with sub-arcsecond accuracy (Figure 2). *Chandra* detects all of the known O stars and about half the cataloged early B stars in NGC 6618, and adds dozens of likely new massive, intermediate-mass, and protostellar members as well as hundreds of T Tauri stars. Sparse clusters around M17-UC1, the KWO, and M17-North are found. Soft diffuse X-ray emission arising from thermalized O-star winds pervades the HII region, as discussed by TFM03.

This paper begins with a description of the X-ray sources and their stellar counterparts (§2). We quantify the stellar population and its spatial structure in §3. Two important subpopulations, the embedded stars and the massive OB stars, are discussed in detail in the next two sections (§4-5). We summarize our findings in §6.

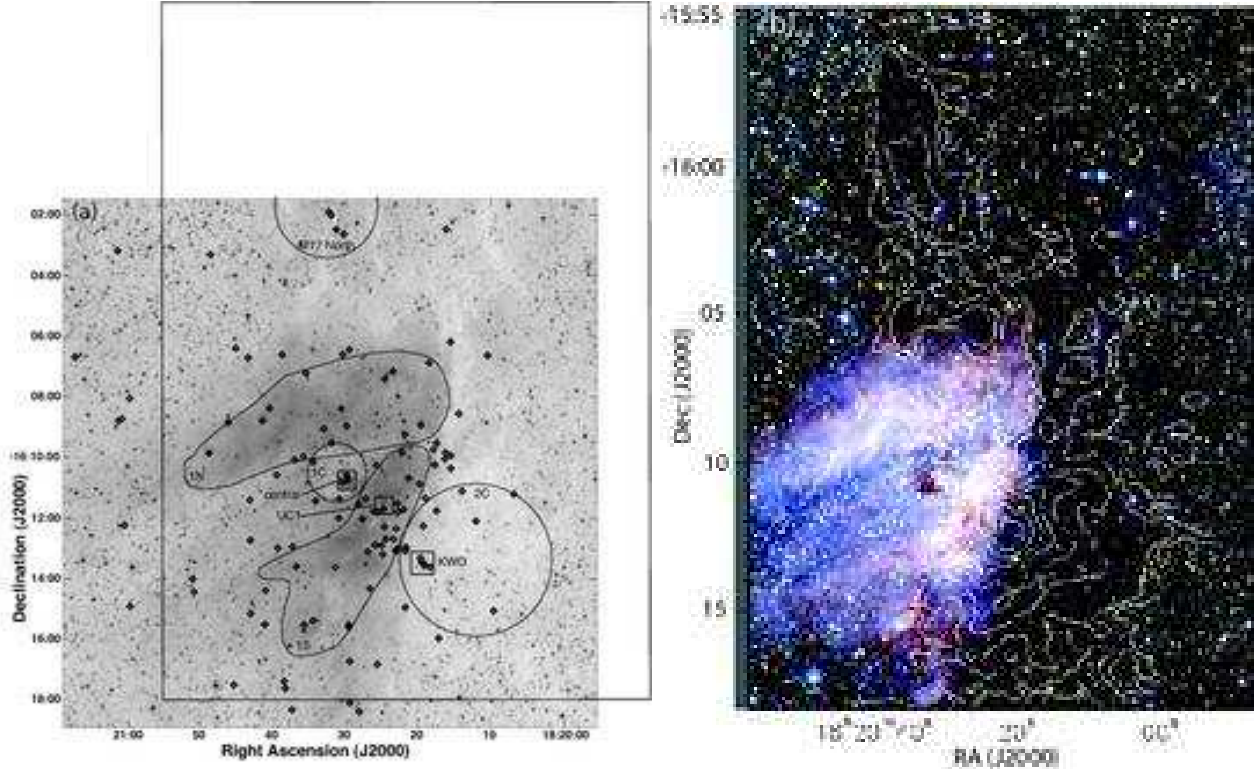


Fig. 1.— (a) 2MASS  $K$ -band mosaic of M17 covering the  $17' \times 17'$  *Chandra* field. The 115 small diamonds mark ACIS sources without identified counterparts (§2.4.1). Two polygons, reproduced with their labels from Figure 2c in Jiang et al. (2002), outline the North Bar and South Bar in the HII region. Two circles, reproduced with their labels from the same figure, outline the central NGC 6618 stellar cluster core and the embedded M17-SW region. A third circle outlines the embedded M17-North region described by Henning et al. (1998). Three small boxes indicate the expanded views in Figures 10 and 11. (b)  $C^{18}O$  contours ( $-5, -2, 2, 4, 10, 20, 30, 40, 50,$  and  $60 \text{ K km s}^{-1}$ ) shown on an image from the 2MASS survey, taken from the right-hand panel in Figure 1 of Wilson et al. (2003) and reproduced here with permission of the authors. This field of view is marked by a large rectangle in panel *a*.

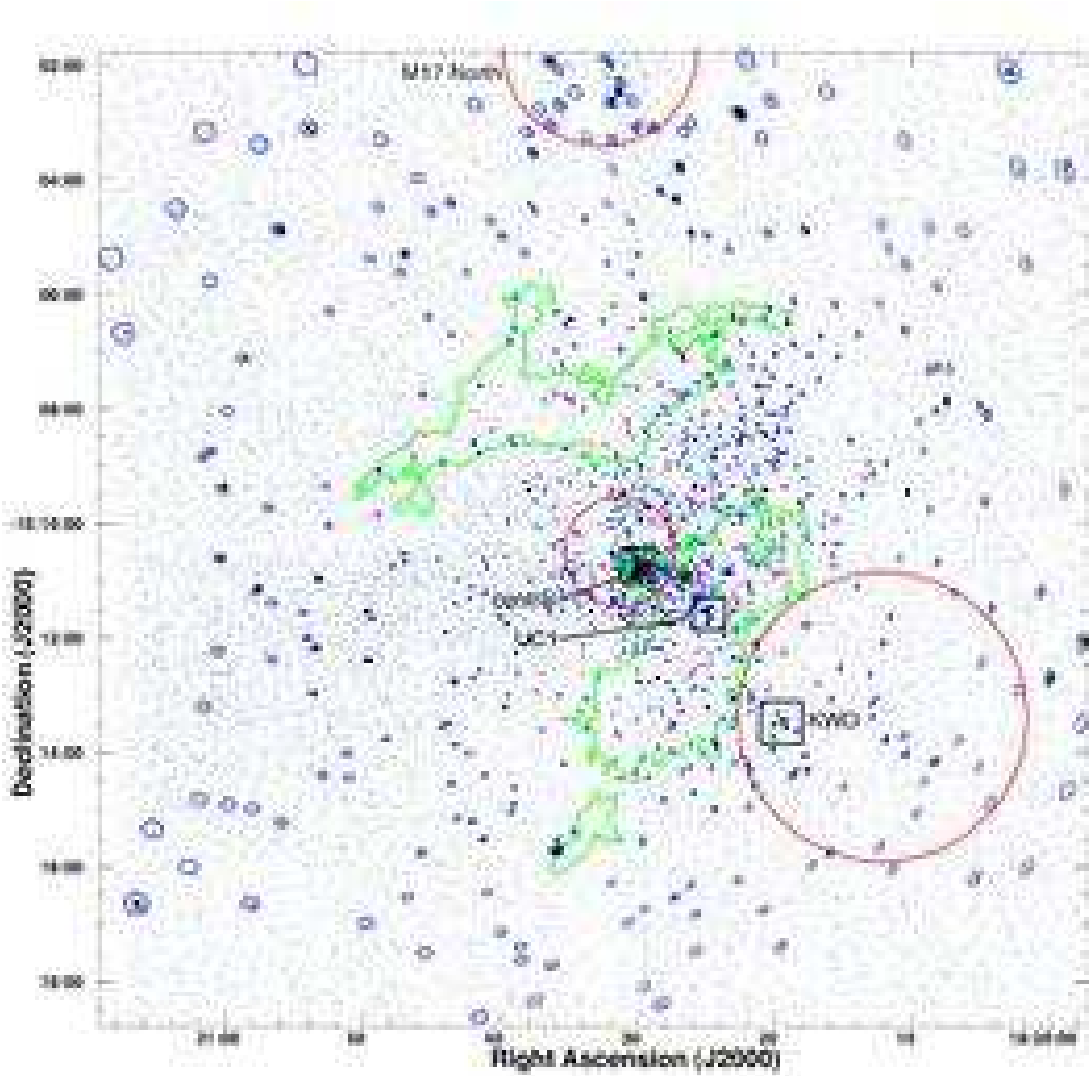


Fig. 2.— A *Chandra* ACIS-I binned image of M17 with 886 source extraction regions designed to match the *Chandra* Point Spread Function (PSF) shown in blue. The PSF is a complex function of position and photon energy; for example the 90% encircled energy radius at 1.5 keV varies from  $\sim 0.9''$  on axis to  $\sim 6''$  at the field edge (see §4 of The *Chandra* Proposers' Observatory Guide at <http://asc.harvard.edu/proposer/>). Contours (green) of bright dust emission from *Spitzer*  $3.6\mu\text{m}$  data outline the North Bar and South Bar in the HII region. The circles and squares are reproduced from Figure 1.

## 2. X-ray Observation, Data Analysis, and Initial Results

M17 was observed with the Imaging Array of the *Chandra*/ACIS camera (ACIS-I,  $17' \times 17'$  field of view) for roughly 40 ks in March 2002. The aim point was centered on the source with the earliest spectral type in NGC 6618’s central ring of O stars, the O4+O4 visual binary (§5.2) called “Kleinmann’s Anonymous Star” (Kleinmann 1973).

Our data reduction methods are described in detail in Appendix B of TFM03; the same reduced dataset used in that study was also used for this one, so we refer the reader to that description for details of the dataset and our data analysis. Briefly, the data were corrected for charge transfer inefficiency (CTI) problems in the CCDs using the Penn State CTI corrector (Townsend et al. 2002); the  $0.5''$  event position randomization added in the *Chandra* X-ray Center’s standard data processing was removed; a sub-pixel positioning scheme (Tsunemi et al. 2001) was applied to improve source positions. We then created twelve different images of the ACIS field: soft (0.5–2 keV), hard (2–8 keV), and full (0.5–8 keV) X-ray wavebands with four different pixel binning scales ( $4\times$ ,  $2\times$ ,  $1\times$ , and  $0.5\times$  the nominal  $0.5''$  ACIS sky pixel) to cover the full ACIS field, the ACIS Imaging Array, the central  $8'$ , and the central  $4'$ , respectively.

### 2.1. Source Detection and Extraction

A list of candidate point sources was then obtained in each of these band-limited images using the *wavdetect* wavelet source detection algorithm (Freeman et al. 2002). The algorithm was purposefully run with a low threshold ( $P = 10^{-5}$ ) that is sensitive to very faint sources but also identifies some spurious noise features. The  $10^{-5}$  *wavdetect* threshold is used because experience has shown that more stringent thresholds (e.g. the more typical  $10^{-6}$ ) result in many missed sources in regions with complex backgrounds, such as M17’s diffuse X-ray emission. These twelve source lists were merged (keeping the source position from the highest-resolution image) to generate the master list of candidate sources for the full observation. The field was visually examined and a few possible faint sources missed by the algorithm were added, resulting in 933 candidate source positions.

Photons were extracted using the ACIS Extract<sup>1</sup> (AE) software package (Broos et al. 2002). The procedures used in AE are described in TFM03 and Getman et al. (2005b). The source extraction regions were usually defined to be  $\sim 90\%$  contours of the local Point Spread Function (PSF) at 1 keV; crowded sources were assigned smaller extraction regions following visual review. AE applies an energy-dependent correction to each source’s calibration, via the Ancillary Response Function (ARF) file, to account for its finite extraction region.

The background event data set from which local background spectra were constructed was obtained by masking regions around all the sources in the catalog via a process that involved two passes through AE. First, conservative circular masks covering  $> 99\%$  of each source PSF were constructed, local backgrounds were extracted, and source fluxes were estimated. Then, each source mask was redefined using the generally less restrictive criteria that: (a) the mask shall include the source extraction region (polygon) itself; and (b) the mask shall also include the region where the expected surface brightness from the point source is larger than one half the observed smoothed local background. A circular background region was then defined

---

<sup>1</sup>The ACIS Extract software package and User’s Guide have been available online at [http://www.astro.psu.edu/xray/docs/TARA/ae\\_users\\_guide.html](http://www.astro.psu.edu/xray/docs/TARA/ae_users_guide.html) since February 2003.

independently for each source such that the region enclosed  $\sim 100$  events in the source-free masked data set.

For each candidate source AE computed the quantity  $P_B$ , the Poisson probability associated with the “null hypothesis” that no source exists with respect to the local background level. We chose two thresholds on  $P_B$  to define the final source list:  $P_B < 0.003$  for 845 “primary” sources and  $0.003 < P_B < 0.01$  for 41 “tentative” sources. Counterparts were identified for 31 of these tentative sources (§2.4), adding confidence that these sources are real. The remaining 47 candidate sources had  $P_B > 0.01$  and were rejected as likely background fluctuations.

These 886 sources are shown superposed on the ACIS-I field in Figure 2. AE and the *Chandra* software package CIAO (version 3.2) were used to compute source and local background spectra, calibration files<sup>2</sup>, background-corrected median energies, light curves, variability estimates, broad-band photometry, and other quantitative information for each source. Basic properties of the primary and tentative sources are presented in Tables 1 and 2. Sources are listed by increasing right ascension and can be identified by their sequence number (e.g. #358) or their IAU designation (e.g. CXOU J182025.70–161649.9). Please see the table notes for definitions of the columns and see Getman et al. (2005b) and Townsley et al. (2006b) for further details on the derivations of the properties. The positions reported are estimated by AE; the *Chandra* coordinate system was aligned to the *Hipparcos* reference frame using 51 matches between strong on-axis ACIS sources and reliable 2MASS stars (§2.4). The formal uncertainty in the remaining systematic reference frame offset between *Chandra* and 2MASS is  $\sim 0.04''$  in each axis.

## 2.2. Source Variability

Thirty-nine of the M17 ACIS sources show significant X-ray variability ( $P_{KS} < 0.005$  in column 15 of Table 1). We display some of these variable light curves in Figure 3. Many show the high-amplitude, fast-rise-slow-decay morphology characteristic of solar-type magnetic reconnection flares (Reale et al. 2001). Some show secondary flares superposed on the decays of primary flares. Others show a poorly understood slow rise over several hours. This wide range of flare morphologies is characteristic of X-ray luminous pre-main sequence stars (e.g. Imanishi et al. 2001; Grosso et al. 2004; Favata et al. 2005; Wolk et al. 2005). A few sources show more random variability not characteristic of T Tauri flares. One bright variable star (#396) is not shown here, but is discussed in Section 5.3; light curves for 24 variable but weak sources are not shown.

## 2.3. X-ray Fluxes and Luminosities

Characterization of the spectral properties and luminosities of the sources in this data set is a challenging endeavor because the quantity of data available for most sources is so low: 95% of sources have fewer than 100 net counts. Such data sets poorly constrain spectral model parameters, and “best fit” models are often nonphysical.

Investigators have adopted various approaches to analyze weak ACIS source spectra. Some use an assumed intrinsic source spectrum and absorbing column to derive a scaling factor between intrinsic luminosity and observed flux that is applied to all weak sources (Hong et al. 2005; Munro et al. 2006a). Some

---

<sup>2</sup>CIAO calibrations include the effects of contamination on the ACIS-I optical blocking filter.

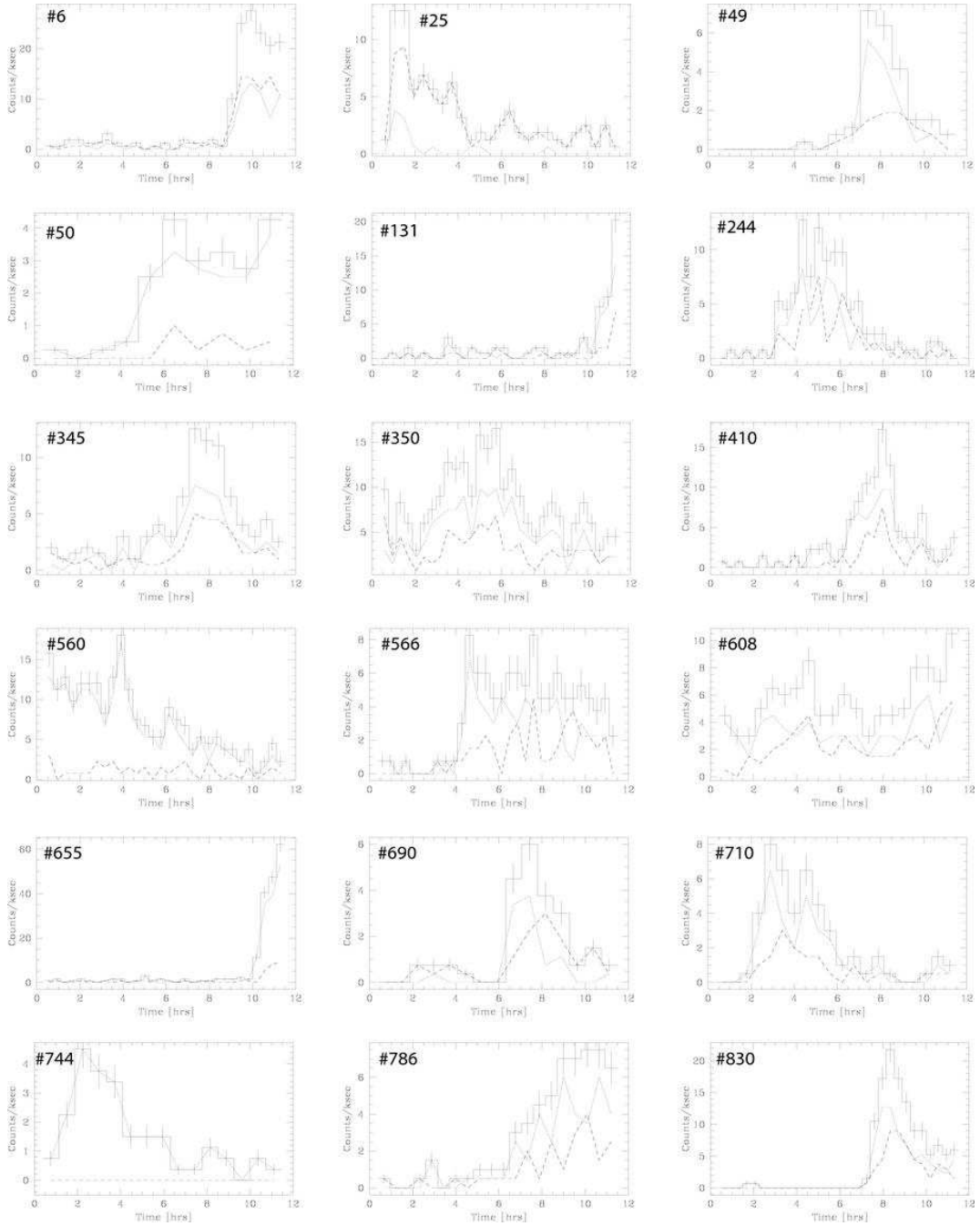


Fig. 3.— Light curves for some sources exhibiting strong variability during the *Chandra* observation, labeled by sequence number. Histograms show the full (0.5 – 8.0 keV) energy band with  $\sqrt{N}$  error bars; dashed lines show the soft (0.5 – 2.0 keV) band; dotted lines show the hard (2.0 – 8.0 keV) band. Note that the ordinates vary between panels.

investigators apply prior knowledge about individual sources, such as  $A_V$  estimates from optical or NIR photometry, to constrain spectral models (Getman et al. 2006a; Flaccomio et al. 2006). Others limit their goals to obtaining non-unique spline-like fits to the event energy distribution, allowing nonphysical models, and emphasize caution when interpreting the spectral parameters (Feigelson et al. 2002). All of these approaches are reasonable.

Another issue concerns the mathematical method of seeking the best-fit spectral model, and then estimating confidence intervals on the spectral parameters. A least-squares approach based on the  $\chi^2$  statistic applied to binned data is traditional, although maximum likelihood estimation of unbinned data is becoming more common. With the nonlinear dependence between spectral parameters, it is often difficult to establish their confidence intervals for weak sources in an authoritative manner. Bayesian analysis provides a likelihood-based approach that incorporates prior knowledge expressed through prior distributions (van Dyk et al. 2001). The uncertainties of the derived parameters (such as absorption-corrected luminosities) are uncovered through posterior distributions, and one can marginalize over uninteresting parameters if one chooses. However, standard tools for a full Bayesian spectral analysis for X-ray data are not yet available.

In this study, we adopt a strategy most similar to that of Feigelson et al. (2002). Our primary goal is to obtain wide-band fluxes using regression models as spline functions. Fluxes are then converted to luminosities, both observed and intrinsic (corrected for estimated absorption), using a distance of 1.6 kpc. Calculations are performed using the XSPEC package (version 12.2.10, Arnaud 1996)<sup>3</sup> to fit one- and two-temperature *apec* thermal plasma models (Smith et al. 2001) and power law models seen through an absorbing column ( $N_H$ ) of interstellar material with cosmic elemental abundances (Morrison & McCammon 1983). The one-temperature thermal plasma model is preferentially used and abundances of  $Z = 0.3Z_\odot$  are assumed, as found for pre-main sequence stars in other, more nearby, star-forming regions (Imanishi et al. 2001; Feigelson et al. 2002). A power law model is adopted if the thermal model poorly described the data or required nonphysical parameters, and if the source is not identified with a known stellar counterpart. When neither best-fit model is acceptable, we freeze the parameter  $kT = 2$  keV in the thermal model, which is typical for young stars (Getman et al. 2005b; Preibisch et al. 2005a), and then fit for the  $N_H$  and normalization parameters. Analysis was not attempted on the 288 weakest sources whose photometric significance (column 12 in Tables 1 and 2) is below 2.0.

The best-fit model was found by the maximum likelihood method (XSPEC minimizes the C statistic, Cash 1979; Wachter et al. 1979). Although the accuracy of the parameter error estimation algorithm in XSPEC is not well understood for weak sources, we report 90% confidence intervals when they were flagged<sup>4</sup> acceptable by XSPEC. One should regard the reported parameter errors with suitable caution. A simulation of parameter uncertainties for weak sources was reported by Feigelson et al. (2002).

Spectral analysis results for the brighter 598 sources are presented in Tables 3 and 4. See the table notes for descriptions of the columns. Best-fit absorbing column densities range from negligible to  $\log N_H \sim 23.7$  cm<sup>-2</sup>, equivalent to a visual absorption of  $A_V \sim 250$ –300 mag. Temperatures range from the softest ( $kT \sim 0.4$  keV) to the hardest (truncated at  $kT = 15$  keV) accessible to the *Chandra* ACIS-I detectors. The range of observed total band (0.5 – 8 keV) luminosities, corrected for absorption, able to be derived from spectral modeling is  $29.8 \lesssim \log L_{t,c} \lesssim 33.3$  ergs s<sup>-1</sup>. Apparent luminosities range from  $\log L_t \sim 29.3$  ergs s<sup>-1</sup>

---

<sup>3</sup> <http://heasarc.gsfc.nasa.gov/docs/software/lheasoft/xanadu/xspec>

<sup>4</sup>See the *tblout error* command in the XSPEC manual.

(estimated for the faintest “tentative” sources in Table 2) to  $\log L_t = 32.8 \text{ ergs s}^{-1}$ . Completeness limits are discussed in §3.2.

These tables report a variety of band-limited luminosities, both apparent and corrected for absorption (see Getman et al. 2005b, for details). Absorption-corrected soft-band luminosities ( $L_{s,c}$  in our nomenclature) are highly uncertain and are not reported. For highly obscured sources ( $\log N_H > 22.5 \text{ cm}^{-2}$ ), soft-band luminosities are not reported because they may be misleading; the spectral fits are based solely on hard counts for these sources, so the model parameters may significantly underestimate or even miss entirely contributions from soft spectral components. Thus, although we could report  $L_s$  and  $L_{s,c}$  derived from the model fit, we choose to omit these quantities because they are not representative of the true soft-band luminosities of these obscured sources. The reader is cautioned that total-band luminosities may underestimate the true source luminosities due to such missing soft spectral components in our models.

While a power law fit may suggest that the source could be a background AGN, this result is not definitive. Of the 52 sources in Table 4, all but 12 have IR counterparts (see §2.4); brighter IR sources are less likely to be AGN. Conversely, some sources fit with very hard thermal plasmas may be equally well fit with power laws; we preferentially chose the thermal fit in such cases.

## 2.4. Stellar Counterparts

Due to the combination of high obscuration and confusion by bright nebular emission, there are no adequate visual band catalogs of stars in the M17 region. The best stellar survey of the region is in the NIR bands, using the SIRIUS instrument on the InfraRed Survey Facility (IRSF) 1.4 m telescope at the South African Astronomical Observatory. SIRIUS detected over 29,000 stars with sensitivity limits around  $J < 20 \text{ mag}$  and  $K < 19 \text{ mag}$  and sub-arcsecond resolution over a  $14' \times 14'$  region (Jiang et al. 2002). For outer portions of the ACIS field outside the SIRIUS coverage, we use the 2MASS All-Sky Survey which reaches  $K \sim 15.5 \text{ mag}$ . A survey of the region with the IRAC detector on board the *Spitzer Space Telescope* in four IR ( $3.6 - 8 \mu\text{m}$ ) bands has recently been released by the Galactic Legacy Infrared Mid-Plane Survey Extraordinaire (GLIMPSE) Legacy Team (e.g. Churchwell et al. 2004). Here we considered the on-line  $\sim 30$  million source Highly Reliable Catalog from the GLIMPSE Enhanced Data Products<sup>5</sup>.

We associate ACIS X-ray sources with IR sources using positional coincidence criteria<sup>6</sup>. We first removed reference frame offsets between the ACIS field (aligned to 2MASS) and the SIRIUS and GLIMPSE catalogs using high-quality ACIS sources (brighter than 10 counts and within  $2'$  of the aim point). The estimated offsets were  $0.6''$  to SIRIUS and  $0.3''$  to GLIMPSE. Then, for every pair of catalog entries (e.g. an ACIS and a SIRIUS source), we test the hypothesis that the two physical sources are spatially coincident, i.e. that the two observed positions are random samples drawn from Gaussian distributions with identical means and with the reported standard deviations in position. If the hypothesis is true then the offsets between the two observed positions (in X and Y) will be drawn from a 2-D Gaussian distribution with zero mean and with X and Y variances equal to the sums of the reported variances. We reject this hypothesis if the observed positional offsets fall outside a 99% confidence region of this two-dimensional Gaussian. IR positional errors are obtained from the catalogs. ACIS positional errors consist of a random component (computed by AE),

---

<sup>5</sup> <http://www.astro.wisc.edu/sirtf/glimpsedata.html>

<sup>6</sup>Software implementing the matching algorithm described here is available in the TARA package at <http://www.astro.psu.edu/xray/docs/TARA/>.

corresponding to the uncertainty inherent in averaging a finite number of event positions, added in quadrature with an arbitrary  $0.2''$  systematic component that avoids unreasonably small error estimates for very bright sources.

The pairs of catalog entries for which the match hypothesis is satisfied are accepted as matches in order of their likelihood. When a match is accepted, the participating IR source is removed from all pending pairs not yet accepted, thus ensuring that no duplicates appear among the associations. In crowded locations, multiple IR sources satisfy the match hypothesis for a specific ACIS source. In such situations, if the most likely IR match of the group is still available, then it is accepted. Otherwise the ACIS source remains unmatched.

Likely associations between ACIS sources and IR sources are reported in Table 5. Listed there are 727 SIRIUS, 476 2MASS, and 224 GLIMPSE counterparts; 771 of the 886 ACIS sources (87%) have a counterpart identified. GLIMPSE counterparts were notably absent from the North Bar and South Bar which suffer from bright nebular emission. IR photometry is reproduced from the catalogs; *JHK* magnitudes are from SIRIUS photometry when available, except for four sources (ACIS #366, 701, 720, and 854) where 2MASS values are more reliable due to saturation effects in the SIRIUS images. Table 5 also gives likely associations to optical stars reported by Chini, Elsaesser, & Neckel (1980) (designated CEN xxx) and to NIR stars from Hanson, Howarth, & Conti (1997) derived from Bumgardner (1992) (designated B xxx)<sup>7</sup>. Association ambiguity flags and notes to other published characteristics of selected sources can be found in the table.

The list of matches in Table 5 is not perfect, as both false negatives (true physical associations that are missed) and false positives (unphysical associations that are listed) are likely present. To the extent that the actual distributions of position errors follow the stated Gaussian distributions, we expect to miss 1% of true associations (false-negatives) as specified by the 99% confidence interval adopted. In Appendix A we estimate that 2.5% of the 2MASS associations, 7% of the SIRIUS associations, and 9% of the GLIMPSE associations are expected to be incorrect due to uncertainty in positions. A non-statistical problem in identifying stellar counterparts is that some cataloged IR sources may be condensations in the nebular emission (from atomic lines, PAH bands, or heated dust continuum) rather than stars. Some NIR sources may be unresolved multiple systems, and (particularly when the primary has spectral type A or B, Stelzer et al. 2005) the brightest component may not be the principal X-ray emitter. In short, our associations should be considered only “likely” rather than confirmed stellar counterparts to the ACIS sources.

Figure 4*a* shows the distributions of offsets between the ACIS and IR associations. Figure 4*b* shows the expected deterioration in positional offsets as the *Chandra* PSF broadens off-axis. This can be compared to a similar plot from the *Chandra* Orion Ultradeep Project (COUP) survey of the Orion Nebula which shows median offsets increasing from  $0.12''$  on-axis to  $0.4''$  off-axis (Getman et al. 2005b, Figure 9). The M17 median offsets are poorer, ranging from  $0.2''$  to  $1''$ , due mainly to the much weaker ACIS sources in the short M17 observation compared to the long COUP observation.

---

<sup>7</sup> A reference frame offset of  $1.9''$  between ACIS and Hanson, Howarth, & Conti (1997) positions was removed before matching the catalogs.

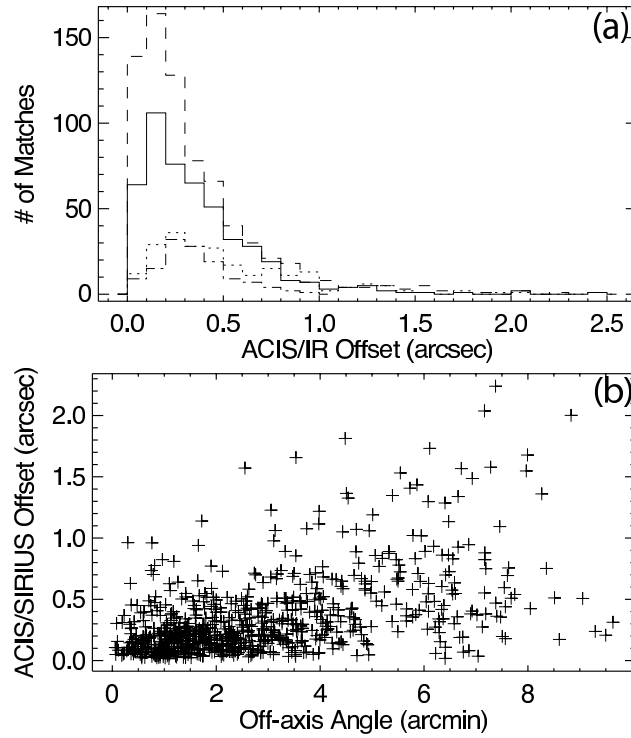


Fig. 4.— Positional offsets between matching ACIS and IR sources, after removal of reference frame offsets. Panel (a) shows offset distributions for SIRIUS (dashed), 2MASS (solid), GLIMPSE (dotted), and Bumgardner (dash-dot) matches. The median ACIS/SIRIUS offset is  $0.24''$ . Panel (b) shows offsets for SIRIUS matches vs. off-axis angle in the ACIS field.

Table 1. Primary *Chandra* Catalog: Basic Source Properties

Source		Position				Extracted Counts					Characteristics					
Seq #	CXOU J	$\alpha_{J2000}$ (deg)	$\delta_{J2000}$ (deg)	Err ( $''$ )	$\theta$ ( $'$ )	Net Full	$\Delta$ Net Full	Bkgd Full	Net Hard	PSF Frac	Signif	$\log P_B$	Anom	Var	EffExp (ks)	$E_{median}$ (keV)
(1)	(2)	(3)	(4)	(5)	(6)	(7)	(8)	(9)	(10)	(11)	(12)	(13)	(14)	(15)	(16)	(17)
37	182009.70-161503.7	275.040439	-16.251041	0.8	6.7	9.7	4.0	2.3	9.4	0.90	2.1	<-5	.	a	32.1	5.3
51	182012.31-160447.7	275.051294	-16.079918	0.8	7.2	16.4	5.0	3.6	11.7	0.90	2.9	<-5	.	a	31.6	2.3
97	182017.84-161117.0	275.074374	-16.188070	0.3	3.1	5.6	3.0	0.4	5.7	0.90	1.6	<-5	.	a	36.7	3.2
123	182019.41-161329.1	275.080890	-16.224756	0.1	4.0	30.8	6.1	0.2	25.9	0.60	4.6	<-5	.	a	36.1	3.3
128	182019.60-161038.8	275.081670	-16.177456	0.3	2.6	8.6	3.5	0.4	8.7	0.89	2.1	<-5	.	a	37.4	4.8
135	182019.88-161052.3	275.082863	-16.181206	0.3	2.5	8.5	3.5	0.5	8.7	0.89	2.1	<-5	.	b	37.4	5.7
163	182020.73-160717.9	275.086416	-16.121661	0.3	3.9	8.2	3.5	0.8	7.5	0.89	2.0	<-5	.	a	36.4	3.5
177	182021.21-161222.9	275.088397	-16.206382	0.2	2.9	16.4	4.6	0.6	12.6	0.90	3.1	<-5	.	a	37.2	2.8
182	182021.32-161140.2	275.088858	-16.194518	0.2	2.5	11.5	4.0	0.5	1.6	0.89	2.5	<-5	.	b	37.4	1.2
186	182021.43-160939.1	275.089300	-16.160865	0.1	2.3	30.3	6.1	0.7	16.6	0.89	4.6	<-5	.	a	38.0	2.1
187	182021.43-161206.8	275.089325	-16.201912	0.0	2.7	363.4	19.6	0.6	288.6	0.89	18.1	<-5	.	a	37.3	3.1
230	182022.58-160251.3	275.094121	-16.047608	0.2	7.9	365.4	19.8	5.6	257.7	0.90	18.0	<-5	.	a	31.2	2.6
233	182022.69-160833.9	275.094578	-16.142761	0.1	2.7	73.1	9.1	0.9	24.6	0.89	7.6	<-5	.	a	38.0	1.7
236	182022.74-161123.5	275.094775	-16.189866	0.1	2.0	60.3	8.3	0.7	45.5	0.89	6.8	<-5	.	a	37.9	2.6
239	182022.87-161148.5	275.095298	-16.196825	0.1	2.2	19.3	5.0	0.7	19.5	0.89	3.5	<-5	.	a	37.1	4.9
244	182022.93-161152.7	275.095573	-16.197986	0.1	2.3	134.4	12.1	0.6	77.6	0.89	10.6	<-5	g	...	35.1	2.4
246	182022.97-161131.8	275.095712	-16.192185	0.2	2.1	12.4	4.1	0.6	12.6	0.85	2.6	<-5	g	...	34.1	4.8
255	182023.16-161305.7	275.096504	-16.218256	0.1	3.1	54.4	7.9	0.6	54.5	0.90	6.4	<-5	.	a	35.5	4.6
275	182023.80-161325.7	275.099198	-16.223807	0.4	3.3	8.5	3.5	0.5	8.6	0.90	2.1	<-5	.	a	34.8	4.9
281	182024.00-160818.8	275.100040	-16.138573	0.1	2.7	29.2	6.0	0.8	1.7	0.89	4.5	<-5	.	a	36.2	0.9
296	182024.39-160843.3	275.101640	-16.145367	0.2	2.3	10.2	3.8	0.8	1.7	0.90	2.3	<-5	.	a	38.4	1.3
309	182024.60-161139.2	275.102519	-16.194249	0.1	1.8	19.0	5.0	1.0	18.3	0.90	3.4	<-5	.	a	38.2	3.3
324	182024.87-161127.5	275.103634	-16.190973	0.1	1.6	49.8	7.7	1.2	31.2	0.90	6.1	<-5	.	a	38.2	2.7
329	182024.94-161131.1	275.103949	-16.191974	0.2	1.7	15.7	4.6	1.3	16.2	0.90	3.0	<-5	.	c	38.2	4.4
334	182025.07-161133.9	275.104499	-16.192767	0.1	1.7	21.8	5.3	1.2	12.2	0.90	3.7	<-5	.	a	38.2	2.5
350	182025.50-161053.8	275.106253	-16.181624	0.0	1.2	308.6	18.1	1.4	188.5	0.90	16.6	<-5	.	c	38.6	2.5
370	182025.93-161114.3	275.108062	-16.187315	0.2	1.3	8.8	3.7	1.2	1.6	0.90	2.1	<-5	.	a	38.6	1.5
371	182025.93-160949.4	275.108070	-16.163734	0.2	1.3	8.1	3.5	0.9	3.6	0.90	2.0	<-5	.	a	38.9	1.8
372	182025.95-160938.2	275.108153	-16.160626	0.3	1.4	5.1	3.0	0.9	3.6	0.90	1.4	-3.6	.	b	38.8	2.5
373	182026.00-161253.0	275.108352	-16.214727	0.3	2.6	5.6	3.0	0.4	5.8	0.85	1.6	<-5	.	a	37.8	4.0
374	182026.01-161022.4	275.108377	-16.172897	0.0	1.1	102.3	10.7	0.7	46.7	0.90	9.1	<-5	g	...	27.4	1.8
375	182026.02-161240.0	275.108417	-16.211132	0.2	2.4	8.4	3.5	0.6	4.6	0.89	2.0	<-5	.	a	38.0	2.3
376	182026.04-161104.6	275.108512	-16.184620	0.1	1.2	78.3	9.5	1.7	45.3	0.90	7.8	<-5	.	a	38.6	2.3
377	182026.09-161039.9	275.108747	-16.177772	0.2	1.0	13.9	4.4	1.1	5.5	0.90	2.8	<-5	.	a	38.7	1.8
378	182026.09-160301.3	275.108749	-16.050381	0.7	7.5	11.5	4.5	4.5	0.1	0.90	2.3	-4.7	.	a	31.8	1.1
379	182026.11-161053.5	275.108806	-16.181547	0.1	1.1	21.0	5.3	2.0	10.1	0.90	3.6	<-5	.	a	38.7	1.9
396	182026.60-161055.7	275.110852	-16.182141	0.0	1.0	2473.5	50.3	2.5	1622.0	0.90	48.7	<-5	.	c	38.7	2.7
398	182026.62-161136.5	275.110920	-16.193480	0.1	1.4	18.2	4.9	0.8	7.5	0.90	3.3	<-5	.	a	38.4	1.9
399	182026.62-160822.9	275.110937	-16.139700	0.3	2.3	6.2	3.2	0.8	1.7	0.90	1.6	-4.8	.	a	36.0	1.7
433	182027.41-161331.0	275.114226	-16.225280	0.0	3.1	263.3	16.8	0.7	18.6	0.90	15.2	<-5	.	a	37.5	1.3
466	182028.15-161049.3	275.117308	-16.180378	0.0	0.6	538.1	23.7	1.9	386.2	0.90	22.2	<-5	.	a	38.9	2.7
488	182028.65-161211.6	275.119414	-16.203233	0.1	1.7	70.6	8.9	0.4	35.8	0.89	7.5	<-5	.	a	38.5	2.0
495	182028.86-161042.0	275.120280	-16.178337	0.2	0.4	8.3	3.9	2.7	0.0	0.90	1.9	-4.0	.	a	39.0	1.6
510	182029.21-161425.6	275.121709	-16.240461	0.4	3.9	5.2	3.0	0.8	0.5	0.90	1.4	-3.8	.	a	36.7	1.2
511	182029.28-161041.4	275.122029	-16.178180	0.1	0.3	53.0	8.2	6.0	29.7	0.90	6.1	<-5	.	a	39.1	2.2
512	182029.31-161047.9	275.122151	-16.179989	0.1	0.4	77.4	9.5	3.6	50.4	0.83	7.7	<-5	.	a	39.1	2.5
513	182029.32-161045.2	275.122167	-16.179236	0.1	0.4	16.8	5.0	3.2	11.5	0.79	3.0	<-5	.	a	39.1	2.4
514	182029.36-160919.2	275.122353	-16.155335	0.2	1.2	6.1	3.2	0.9	2.6	0.91	1.6	-4.4	.	a	39.1	1.8
515	182029.39-160943.0	275.122474	-16.161946	0.0	0.8	155.2	13.0	0.8	102.6	0.90	11.5	<-5	.	a	39.3	2.5
516	182029.39-161046.5	275.122489	-16.179593	0.0	0.4	69.5	9.1	3.5	53.4	0.79	7.2	<-5	.	a	39.1	3.0
517	182029.39-161212.9	275.122489	-16.203593	0.2	1.7	8.5	3.5	0.5	1.8	0.89	2.1	<-5	.	a	38.5	1.4
518	182029.43-161050.2	275.122661	-16.180616	0.1	0.4	47.0	7.8	6.0	29.9	0.90	5.6	<-5	.	a	39.1	2.7
536	182029.81-161045.6	275.124213	-16.179352	0.0	0.3	1912.2	44.3	6.8	1052.5	0.80	42.7	<-5	.	a	39.1	2.2
543	182029.89-161044.5	275.124574	-16.179031	0.0	0.3	3865.9	62.7	8.1	2447.0	0.80	61.1	<-5	.	a	39.1	2.6
567	182030.23-161034.9	275.125982	-16.176382	0.1	0.1	43.6	7.5	4.4	9.4	0.90	5.5	<-5	.	a	39.2	1.7
574	182030.44-161053.1	275.126836	-16.181427	0.1	0.4	89.5	10.3	5.5	22.3	0.90	8.3	<-5	.	a	39.2	1.7
600	182030.95-161039.4	275.128970	-16.177620	0.2	0.2	8.0	3.7	2.0	5.0	0.90	1.9	-4.3	.	a	39.2	2.3
618	182031.35-160228.4	275.130660	-16.041249	0.4	8.0	64.4	9.3	11.6	38.7	0.75	6.5	<-5	.	a	29.3	2.3

Table 1—Continued

Source		Position				Extracted Counts					Characteristics					
Seq #	CXOU J	$\alpha_{J2000}$ (deg)	$\delta_{J2000}$ (deg)	Err ( $''$ )	$\theta$ ( $'$ )	Net Full	$\Delta$ Net Full	Bkgd Full	Net Hard	PSF Frac	Signif	$\log P_B$	Anom	Var	EffExp (ks)	$E_{median}$ (keV)
(1)	(2)	(3)	(4)	(5)	(6)	(7)	(8)	(9)	(10)	(11)	(12)	(13)	(14)	(15)	(16)	(17)
647	182031.84–161138.1	275.132701	-16.193943	0.3	1.2	3.5	2.5	0.5	0.8	0.90	1.1	-2.9	g	...	27.5	1.6
650	182031.89–161616.5	275.132883	-16.271262	0.6	5.8	10.0	3.8	1.0	3.5	0.91	2.3	<-5	g	...	18.0	1.7
655	182031.97–161030.5	275.133240	-16.175147	0.0	0.4	249.3	16.3	0.7	208.6	0.90	14.8	<-5	g	...	25.8	3.4
706	182034.56–161523.6	275.144010	-16.256565	0.5	5.0	9.0	3.7	1.0	9.4	0.89	2.1	<-5	.	a	33.6	5.0
726	182035.63–161055.5	275.148459	-16.182086	0.2	1.3	11.2	4.0	0.8	1.8	0.90	2.5	<-5	.	a	39.0	1.4
854	182053.86–160306.5	275.224439	-16.051830	0.4	9.3	105.5	11.3	9.5	6.0	0.91	8.9	<-5	.	a	29.3	1.0

Note. — Table 1 is published in its entirety in the electronic edition of the *Astrophysical Journal*. Interesting sources mentioned in the text are shown here for guidance regarding its form and content.

Note. — **Column 1:** X-ray catalog sequence number, sorted by RA. **Column 2:** IAU designation. **Columns 3,4:** Right ascension and declination for epoch J2000.0. **Column 5:** Estimated standard deviation of the random component of the position error,  $\sqrt{\sigma_x^2 + \sigma_y^2}$ . The single-axis position errors,  $\sigma_x$  and  $\sigma_y$ , are estimated from the single-axis standard deviations of the PSF inside the extraction region and the number of counts extracted. **Column 6:** Off-axis angle. **Columns 7,8:** Net counts extracted in the total energy band (0.5–8 keV); average of the upper and lower  $1\sigma$  errors on column 7. **Column 9:** Background counts extracted (total band). **Column 10:** Net counts extracted in the hard energy band (2–8 keV). **Column 11:** Fraction of the PSF (at 1.497 keV) enclosed within the extraction region. Note that a reduced PSF fraction (significantly below 90%) may indicate that the source is in a crowded region. **Column 12:** Photometric significance computed as  $\frac{\text{net counts}}{\text{upper error on net counts}}$ . **Column 13:** Log probability that extracted counts (total band) are solely from background. Some sources have  $P_B$  values above the 1% threshold that defines the catalog because local background estimates can rise during the final extraction iteration after sources are removed from the catalog. **Column 14:** Source anomalies: g = fractional time that source was on a detector (FRACEXPO from *mkarf*) is  $< 0.9$ ; e = source on field edge; p = source piled up; s = source on readout streak. **Column 15:** Variability characterization based on K-S statistic (total band): a = no evidence for variability ( $0.05 < P_{KS}$ ); b = possibly variable ( $0.005 < P_{KS} < 0.05$ ); c = definitely variable ( $P_{KS} < 0.005$ ). No value is reported for sources with fewer than 4 counts or for sources in chip gaps or on field edges. **Column 16:** Effective exposure time: approximate time the source would have to be observed on-axis (no telescope vignetting) on a nominal region of the detector (no dithering over insensitive regions of the detector) to obtain the reported number of counts. **Column 17:** Background-corrected median photon energy (total band).

Table 2. Tentative *Chandra* Catalog: Basic Source Properties

Source		Position				Extracted Counts					Characteristics					
Seq #	CXOU J	$\alpha_{J2000}$ (deg)	$\delta_{J2000}$ (deg)	Err ( $''$ )	$\theta$ ( $'$ )	Net Full	$\Delta$ Net Full	Bkgd Full	Net Hard	PSF Frac	Signif	$\log P_B$	Anom	Var	EffExp (ks)	$E_{median}$ (keV)
(1)	(2)	(3)	(4)	(5)	(6)	(7)	(8)	(9)	(10)	(11)	(12)	(13)	(14)	(15)	(16)	(17)
322	182024.83-161135.3	275.103482	-16.193161	0.5	1.7	2.9	2.5	1.1	3.3	0.90	0.9	-1.6	.	a	38.2	4.7
519	182029.48-161644.0	275.122866	-16.278895	0.7	6.2	5.6	3.4	2.4	0.6	0.90	1.4	-2.5	.	a	33.7	1.5

Note. — Table 2 has the same columns as 1 and is published in its entirety in the electronic edition of the *Astrophysical Journal*. Interesting sources mentioned in the text are shown here for guidance regarding its form and content.

Note. — See notes for Table 1

Table 3. X-ray Spectroscopy for Photometrically Selected Sources: Thermal Plasma Fits

Seq # (1)	Source <sup>a</sup>			Spectral Fit <sup>b</sup>			X-ray Luminosities <sup>c</sup>					Notes <sup>d</sup> (13)
	CXOU J (2)	Net Counts (3)	Signif (4)	$\log N_H$ ( $\text{cm}^{-2}$ ) (5)	$kT$ (keV) (6)	$\log EM$ ( $\text{cm}^{-3}$ ) (7)	$\log L_s$ (8)	$\log L_h$ (9)	$\log L_{h,c}$ ( $\text{ergs s}^{-1}$ ) (10)	$\log L_t$ (11)	$\log L_{t,c}$ (12)	
37	182009.70–161503.7	9.7	2.1	23.7	1.4	55.7	...	30.55	31.99	30.55	...	...
51	182012.31–160447.7	16.4	2.9	-0.3 22.3 +0.2	2.0	53.9 +0.2	29.54	30.27	30.41	30.35	30.85	...
123	182019.41–161329.1	30.8	4.6	-0.3 22.5 +0.2	-1.7 3.4	-0.4 54.2 +0.5	29.68	30.86	31.01	30.89	31.30	...
128	182019.60–161038.8	8.6	2.1	-0.5 23.2 +0.3	13.6	53.8	...	30.45	30.82	30.45	...	...
135	182019.88–161052.3	8.5	2.1	23.8	2.0	55.3	...	30.54	31.85	30.54	...	...
177	182021.21–161222.9	16.4	3.1	-0.6 22.3 +0.4	-2.3 3.6	53.6 +0.7	29.40	30.32	30.42	30.37	30.71	...
182	182021.32–161140.2	11.5	2.5	-1.1 21.9 +0.3	-0.4 0.7 +0.9	53.5 +0.9	29.66	29.06	29.14	29.76	30.47	...
186	182021.43–160939.1	30.3	4.6	-0.6 22.1 +0.4	-1.7 3.0	-0.4 53.8 +0.6	29.81	30.42	30.48	30.52	30.81	...
187	182021.43–161206.8	363.4	18.1	-0.08 22.4 +0.07	-1.2 4.4 +2.6	-0.1 55.0 +0.1	30.56	31.76	31.89	31.79	32.14	...
230	182022.58–160251.3	365.4	18.0	-0.10 22.3 +0.09	-1.5 4.6 +3.3	-0.1 55.0 +0.1	30.77	31.74	31.83	31.79	32.08	...
233	182022.69–160833.9	73.1	7.6	-0.4 21.7 +0.2	-1.5 3.5 +10.7	-0.2 53.9 +0.2	30.29	30.69	30.72	30.84	31.01	...
236	182022.74–161123.5	60.3	6.8	-0.2 22.6 +0.2	-0.5 1.6 +1.8	-0.5 54.7 +0.4	...	30.86	31.12	30.90	...	...
239	182022.87–161148.5	19.3	3.5	-0.2 23.5 +0.2	2.0	-0.3 55.2 +0.4	...	30.78	31.69	30.78	...	...
244	182022.93–161152.7	134.4	10.6	-0.2 22.2 +0.1	-1.1 3.3 +7.5	-0.3 54.6 +0.2	30.42	31.24	31.33	31.30	31.63	...
246	182022.97–161131.8	12.4	2.6	-0.3 23.5 +0.3	2.6	54.9 +1.6	...	30.72	31.56	30.72	...	...
255	182023.16–161305.7	54.4	6.4	-0.3 23.5 +0.2	-0.7 1.6 +8.5	55.8	...	31.20	32.18	31.20	...	...
275	182023.80–161325.7	8.5	2.1	-0.4 23.1 +0.3	13.7	53.8	...	30.44	30.79	30.44	...	...
281	182024.00–160818.8	29.2	4.5	20.0	-0.3 0.6 +0.1	-0.2 53.3 +0.2	30.21	28.80	28.80	30.22	30.24	...
296	182024.39–160843.3	10.2	2.3	21.6 +0.4	2.0	-0.4 53.1 +0.3	29.52	29.58	29.60	29.85	30.04	...
309	182024.60–161139.2	19.0	3.4	-0.3 22.8 +0.4	-1.1 1.7 +3.4	54.5 +1.7	...	30.50	30.88	30.51	...	...
324	182024.87–161127.5	49.8	6.1	-0.2 22.4 +0.2	-1.0 2.5 +4.0	-0.3 54.2 +0.4	29.88	30.74	30.87	30.80	31.24	...
329	182024.94–161131.1	15.7	3.0	23.1	15.0	54.0	...	30.66	31.00	30.66	...	...
334	182025.07–161133.9	21.8	3.7	-0.3 22.4 +0.3	-0.8 1.7 +2.9	54.1	29.61	30.30	30.47	30.38	30.99	...
350	182025.50–161053.8	308.6	16.6	-0.12 22.1 +0.10	-1.6 5.0 +5.6	-0.1 54.7 +0.1	30.72	31.55	31.62	31.61	31.85	...
370	182025.93–161114.3	8.8	2.1	21.8	2.4	53.0	29.28	29.60	29.64	29.77	30.03	...
374	182026.01–161022.4	102.3	9.1	-0.3 22.0 +0.2	-1.3 3.3 +7.3	-0.2 54.4 +0.2	30.49	31.09	31.14	31.19	31.45	...
375	182026.02–161240.0	8.4	2.0	-0.6 22.6 +0.3	-0.7 1.3	54.1 +1.4	...	29.98	30.29	30.03	...	...
376	182026.04–161104.6	78.3	7.8	-0.2 22.3 +0.3	-1.1 1.9 +1.6	-0.3 54.4 +0.7	30.20	30.81	30.93	30.91	31.38	...
377	182026.09–161039.9	13.9	2.8	-0.6 22.0 +0.5	-1.6 2.2	53.4 +1.2	29.51	29.91	29.97	30.06	30.39	...
378	182026.09–160301.3	11.5	2.3	20.4 +1.6	1.4	-0.3 53.1 +0.5	29.84	29.36	29.36	29.96	29.98	...
379	182026.11–161053.5	21.0	3.6	-0.4 22.0 +0.3	-0.7 1.8 +3.1	-0.4 53.7 +0.4	29.73	30.07	30.14	30.23	30.62	...
396	182026.60–161055.7	2473.5	48.7	-0.04 22.1 +0.03	-4.1 14.5	-0.02 55.6 +0.02	31.56	32.54	32.59	32.58	32.75	...
398	182026.62–161136.5	18.2	3.3	-0.2 22.5 +0.2	-0.3 0.7 +0.5	54.6 +1.0	...	29.99	30.30	30.17	...	...
433	182027.41–161331.0	263.3	15.2	-0.07 22.0 +0.08	-0.11 0.6 +0.08	-0.2 55.1 +0.3	31.02	30.32	30.43	31.10	32.06	...
466	182028.15–161049.3	538.1	22.2	-0.10 22.3 +0.07	-1.4 4.8 +5.2	-0.1 55.1 +0.1	30.85	31.86	31.95	31.91	32.19	...
488	182028.65–161211.6	70.6	7.5	-0.3 22.2 +0.2	-0.8 2.2 +2.7	-0.3 54.3 +0.3	30.15	30.78	30.89	30.87	31.30	...
511	182029.28–161041.4	53.0	6.1	22.6	0.9 +0.5	-0.6 55.0	...	30.55	30.89	30.65	...	...
512	182029.31–161047.9	77.4	7.7	-0.2 22.5 +0.2	-0.5 1.5 +1.0	-0.4 54.8 +0.5	...	30.95	31.19	31.00	...	...
513	182029.32–161045.2	16.8	3.0	-0.2 22.5 +0.2	2.0	-0.3 54.0 +0.2	29.43	30.34	30.52	30.39	30.96	...

Table 3—Continued

Source <sup>a</sup>				Spectral Fit <sup>b</sup>			X-ray Luminosities <sup>c</sup>					Notes <sup>d</sup>
Seq #	CXOU J	Net Counts	Signif	$\log N_H$ ( $\text{cm}^{-2}$ )	$kT$ (keV)	$\log EM$ ( $\text{cm}^{-3}$ )	$\log L_s$	$\log L_h$	$\log L_{h,c}$ ( $\text{ergs s}^{-1}$ )	$\log L_t$	$\log L_{t,c}$	
(1)	(2)	(3)	(4)	(5)	(6)	(7)	(8)	(9)	(10)	(11)	(12)	(13)
515	182029.39–160943.0	155.2	11.5	−0.2 22.3 +0.1	−0.8 2.5 +2.9	−0.3 54.7	30.39	31.23	31.36	31.29	31.72	...
516	182029.39–161046.5	69.5	7.2	−0.2 22.5 +0.2	−1.5 3.0 +7.7	−0.3 54.5 +0.5	29.95	31.04	31.18	31.07	31.51	...
517	182029.39–161212.9	8.5	2.1	−0.7 22.2 +0.3	0.4	54.3	29.48	28.94	29.14	29.59	31.13	...
518	182029.43–161050.2	47.0	5.6	22.5	1.5	54.5 +0.1	...	30.66	30.90	30.72	...	...
536	182029.81–161045.6	1912.2	42.7	−0.03 22.4 +0.03	<i>15.0</i>	−0.04 55.3 +0.04	31.63	32.37	32.48	32.44	33.16	2T (0.9 keV)
543	182029.89–161044.5	3865.9	61.1	−0.05 22.3 +0.04	−1.9 10.4 +3.1	−0.02 55.7 +0.02	31.85	32.78	32.85	32.83	33.28	2T (0.7 keV)
567	182030.23–161034.9	43.6	5.5	−0.1 22.3 +0.2	−0.3 0.6 +0.3	−0.4 54.8 +1.2	30.18	30.05	30.26	30.42	31.72	...
574	182030.44–161053.1	89.5	8.3	22.4	0.6 +0.2	−0.4 55.3	30.47	30.42	30.69	30.75	32.25	...
618	182031.35–160228.4	64.4	6.5	22.5	1.3	−0.59 54.9 +0.08	30.25	30.86	31.09	30.96	31.81	...
650	182031.89–161616.5	10.0	2.3	20.6	14.9	53.0	29.69	30.07	30.08	30.23	30.24	...
655	182031.97–161030.5	249.3	14.8	−0.14 22.5 +0.09	−4.0 8.9	−0.08 54.9 +0.13	30.46	31.83	31.95	31.85	32.13	...
706	182034.56–161523.6	9.0	2.1	−0.6 23.3 +0.3	<i>15.0</i>	−0.6 54.0 +0.4	...	30.56	31.02	30.56	...	...
726	182035.63–161055.5	11.2	2.5	−0.8 21.8 +0.3	<i>2.0</i>	−0.3 53.2 +0.3	29.51	29.71	29.75	29.92	30.19	...
854	182053.86–160306.5	105.5	8.9	21.0 +0.2	0.6 +0.1	54.0	30.83	29.45	29.47	30.85	30.99	...

Note. — Table 3 is published in its entirety in the electronic edition of the *Astrophysical Journal*. Interesting sources mentioned in the text are shown here for guidance regarding its form and content.

<sup>a</sup>For convenience, **columns 1–4** reproduce the source identification, net counts, and photometric significance data from Table 1.

<sup>b</sup>All fits used the “wabs(apec)” model in *XSPEC* and assumed  $0.3Z_{\odot}$  abundances (Imanishi et al. 2001; Feigelson et al. 2002). **Columns 5 and 6** present the best-fit values for the column density and plasma temperature parameters. **Column 7** presents the emission measure for the model spectrum, assuming a distance of 1.6 kpc. *Quantities in italics* were frozen in the fit. Uncertainties represent 90% confidence intervals. More significant digits are used for uncertainties  $< 0.1$  in order to avoid large rounding errors; for consistency, the same number of significant digits is used for both lower and upper uncertainties. Uncertainties are missing when *XSPEC* was unable to compute them or when their values were so large that the parameter is effectively unconstrained. Fits lacking uncertainties, fits with large uncertainties, and fits with frozen parameters should be viewed merely as splines to the data to obtain rough estimates of luminosities; the listed parameter values are unreliable.

<sup>c</sup>X-ray luminosities are presented in **columns 8–12**: s = soft band (0.5–2 keV); h = hard band (2–8 keV); t = total band (0.5–8 keV). Absorption-corrected luminosities are subscripted with a c; they are omitted when  $\log N_H > 22.5 \text{ cm}^{-2}$  since the soft band emission is essentially unmeasurable.

<sup>d</sup>**2T** means a two-temperature model was used; the second temperature is shown in parentheses. See spectra in Figure 12.

Table 4. X-ray Spectroscopy for Photometrically Selected Sources: Power Law Fits

Source <sup>a</sup>				Spectral Fit <sup>b</sup>			X-ray Fluxes <sup>c</sup>				
Seq #	CXOU J	Net Counts	Signif	$\log N_H$ ( $\text{cm}^{-2}$ )	$\Gamma$	$\log N_\Gamma$	$\log L_s$	$\log L_h$	$\log L_{h,c}$ (photons $\text{cm}^{-2} \text{s}^{-1}$ )	$\log L_t$	$\log L_{t,c}$
(1)	(2)	(3)	(4)	(5)	(6)	(7)	(8)	(9)	(10)	(11)	(12)
2	181957.67–161328.8	12.5	2.3	23.1	1.1	-6.3	...	29.82	30.10	29.82	...
5	181959.04–160350.2	55.4	5.7	21.9	1.6	-5.2	30.10	30.88	30.91	30.95	31.10
13	182004.28–161128.9	19.8	3.4	21.6	-1.3 2.1	-5.6	29.78	30.12	30.14	30.28	30.46
40	182010.53–161401.5	24.1	3.9	-1.0 21.9 +0.4	-1.0 1.5	-5.6	29.70	30.49	30.52	30.56	30.71
59	182013.22–160856.5	10.3	2.3	22.2	0.1	-6.4	28.95	30.64	30.67	30.65	30.70
69	182015.48–160706.0	10.1	2.3	22.8	5.4	-3.6	...	29.97	30.54	30.02	...
96	182017.83–161014.5	12.8	2.7	-1.4 22.8 +0.5	1.2	-5.3	...	30.90	31.08	30.90	...
102	182018.19–160937.0	56.5	6.6	-0.3 22.5 +0.2	-1.0 1.5	-4.9	...	31.07	31.18	31.08	...
112	182018.95–160736.9	17.3	3.2	-0.7 22.3 +0.4	1.9	-5.4	29.33	30.41	30.50	30.45	30.76
121	182019.33–161051.9	9.5	2.2	23.0	3.1	-4.4	...	30.32	30.78	30.33	...
153	182020.49–160806.4	15.0	2.9	22.0 +0.5	1.6	-5.7	29.45	30.30	30.34	30.35	30.54
175	182021.08–160738.2	20.2	3.6	22.0 +0.5	1.3	-5.8	29.47	30.50	30.54	30.54	30.67
179	182021.25–160944.3	8.4	2.0	21.5 +0.8	0.6	-6.6	29.11	30.18	30.19	30.21	30.24
189	182021.59–160703.3	11.3	2.5	22.5	1.6	-5.6	...	30.30	30.43	30.32	...
196	182021.74–161317.4	10.4	2.3	22.0 +0.5	1.5	-6.0	29.24	30.16	30.20	30.21	30.37

Note. — Table 4 is published in its entirety in the electronic edition of the *Astrophysical Journal*. A portion is shown here for guidance regarding its form and content.

<sup>a</sup>For convenience, **columns 1–4** reproduce the source identification, net counts, and photometric significance data from Table 1.

<sup>b</sup>All fits used the “wabs(powerlaw)” model in *XSPEC*. **Columns 5 and 6** present the best-fit values for the column density and power law photon index parameters. **Column 7** presents the power law normalization for the model spectrum. *Quantities in italics* were frozen in the fit. Uncertainties represent 90% confidence intervals. Uncertainties are missing when *XSPEC* was unable to compute them or when their values were so large that the parameter is effectively unconstrained. Fits lacking uncertainties, fits with large uncertainties, and fits with frozen parameters should be viewed merely as splines to the data to obtain rough estimates of luminosities; the listed parameter values are unreliable.

<sup>c</sup>X-ray luminosities are presented in **columns 8–12**: s = soft band (0.5–2 keV); h = hard band (2–8 keV); t = total band (0.5–8 keV). Absorption-corrected luminosities are subscripted with a c; they are omitted when  $\log N_H > 22.5 \text{ cm}^{-2}$  since the soft band emission is essentially unmeasurable.

Table 5. Stellar counterparts

Seq	X-ray	Optical/Infrared star						Infrared photometry							
	CXOU	CEN	B	2MASS	SIRIUS	GLIMPSE	Notes	J (mag)	H (mag)	K (mag)	[3.6] (mag)	[4.5] (mag)	[5.8] (mag)	[8.0] (mag)	
(1)	(2)	(3)	(4)	(5)	(6)	(7)	(8)	(9)	(10)	(11)	(12)	(13)	(14)	(15)	
37	182009.70–161503.7	...	...	...	...	...	...	...	...	...	...	...	...	...	
51	182012.31–160447.7	...	...	18201227–1604466	0bc	25643	G015.1109–00.5795	— <sub>051</sub>	15.89	12.27	10.35	8.70	8.39	8.31	8.36
97	182017.84–161117.0	...	...	...	...	13045	...	— <sub>097</sub>	...	17.81:	16.47:	...	...	...	...
123	182019.41–161329.1	...	...	...	...	15128	...	— <sub>123</sub>	12.75	9.68	7.45	...	...	...	...
128	182019.60–161038.8	...	353	18201960–1610382	000	12415	...	— <sub>128</sub>	16.57	14.92	11.92	...	...	...	...
135	182019.88–161052.3	...	...	...	...	...	...	...	...	...	...	...	...	...	...
163	182020.73–160717.9	...	...	18202075–1607176	000	28479	...	...	17.81	13.53	11.30	...	...	...	...
177	182021.21–161222.9	...	...	18202121–1612231	000	12302	...	— <sub>177</sub>	16.88	14.62	13.42	...	...	...	...
182	182021.32–161140.2	17 (B3)	336	18202133–1611403	000	12345	...	...	12.96	12.51	12.33	...	...	...	...
186	182021.43–160939.1	35 (B3)	333	18202142–1609392	00c	14179	G015.0565–00.6501	—	11.79	10.90	10.42	9.77	9.79	...	...
187	182021.43–161206.8	...	335	18202143–1612068	000	13003	G015.0203–00.6694	—	14.14	12.17	11.27	10.24	10.16	...	...
230	182022.58–160251.3	...	...	18202258–1602510	000	28651	<sup>a</sup> G015.1587–00.6007	—	15.57	13.72	...	11.39	10.94	10.29	...
233	182022.69–160833.9	16 (H:O9-B2)	311	18202270–1608342	000	11686	G015.0335–00.6683	— <sub>236</sub>	9.99	9.44	9.10	...	...	...	...
236	182022.74–161123.5	...	310	18202274–1611234	00c	11686	...	— <sub>236</sub>	14.29	12.73	11.97	10.56	10.42	...	...
239	182022.87–161148.5	...	...	...	...	...	...	— <sub>239</sub>	...	...	...	...	...	...	...
244	182022.93–161152.7	...	...	18202294–1611528	000	12326	...	— <sub>244</sub>	14.11	12.95	12.34	...	...	...	...
246	182022.97–161131.8	...	...	...	...	...	...	— <sub>246</sub>	...	...	...	...	...	...	...
255	182023.16–161305.7	...	...	...	...	...	...	— <sub>255</sub>	...	...	...	...	...	...	...
275	182023.80–161325.7	...	...	...	...	12260	...	— <sub>275</sub>	15.99	15.40	15.15	...	...	...	...
281	182024.00–160818.8	7 (F8)	293	18202401–1608187	000	27470	...	— <sub>281</sub>	10.00	9.70	9.58	...	...	...	...
296	182024.39–160843.3	31 (H:O9.5)	289	18202439–1608434	000	27457	...	—	10.56	9.84	9.40	...	...	...	...
309	182024.60–161139.2	...	284	18202460–1611394	000	14322	...	— <sub>309</sub>	13.14	10.62	9.34	...	...	...	...
322	182024.83–161135.3	...	...	...	...	14776	...	— <sub>322</sub>	...	...	...	...	...	...	...
324	182024.87–161127.5	...	279	18202488–1611276	000	14553	...	— <sub>324</sub>	13.02	11.85	10.75	...	...	...	...
329	182024.94–161131.1	...	...	...	...	14878	...	— <sub>329</sub>	15.88:	14.46:	12.46:	...	...	...	...
334	182025.07–161133.9	...	273	18202508–1611339	000	14856	...	— <sub>334</sub>	13.40	11.58	10.29	...	...	...	...
350	182025.50–161053.8	83 (B3)	267	18202550–1610537	000	12337	...	—	13.45	12.08	11.28	...	...	...	...
370	182025.93–161114.3	...	...	18202589–1611142	cpc	14914	...	—	14.64:	14.12	13.41	...	...	...	...
371	182025.93–160949.4	...	...	...	...	13929	...	—	15.57	14.06	13.44	...	...	...	...
372	182025.95–160938.2	...	...	...	...	13173	G015.0653–00.6659	—	16.33	14.49	13.63	11.80	11.30	...	...
373	182026.00–161253.0	...	...	...	...	...	...	—	...	...	...	...	...	...	...
374	182026.01–161022.4	...	252	18202602–1610225	c00	11830	...	—	14.14	12.66	11.97	...	...	...	...
375	182026.02–161240.0	...	256	18202603–1612398	000	11404	...	—	14.92	12.87	11.66	...	...	...	...
376	182026.04–161104.6	26 (B3)	253	18202603–1611045	000	13500	G015.0443–00.6776	—	11.53	10.87	10.53	9.85	9.90	...	...
377	182026.09–161039.9	...	...	18202609–1610404	00c	13925	...	—	15.00	13.65	13.05	...	...	...	...
378	182026.09–160301.3	...	...	18202614–1603007	00c	...	<sup>a</sup> G015.1630–00.6145	—	13.92	13.58	13.63	13.49	13.45	...	...
379	182026.11–161053.5	...	...	...	...	14870	...	—	14.66	13.53	12.80	...	...	...	...
396	182026.60–161055.7	...	...	...	...	14346	...	—	15.02	13.79	13.16	...	...	...	...
398	182026.62–161136.5	...	246	18202661–1611369	c00	...	...	— <sub>398</sub>	...	12.01	10.56	...	...	...	...
399	182026.62–160822.9	74 (B3)	245	18202662–1608229	c00	27036	...	—	13.37	12.34	11.77	...	...	...	...
433	182027.41–161331.0	(H: O6)	0	18202742–1613309	000	14703	...	— <sub>s-433</sub>	8.30	7.89	9.18:	...	...	...	...
466	182028.15–161049.3	85 (B2)	223	18202815–1610493	000	6104	...	— <sub>466</sub>	12.67	11.33	10.62	...	...	...	...
488	182028.65–161211.6	...	215	18202866–1612115	000	5988	...	— <sub>488</sub>	11.35	10.55	10.08	...	...	...	...
495	182028.86–161042.0	84 (B2)	207	18202887–1610421	0cc	6109	...	— <sub>495</sub>	12.69	11.58	11.11	...	...	...	...
510	182029.21–161425.6	...	...	18202924–1614254	000	1967	...	—	14.74	14.21	13.88	...	...	...	...
511	182029.28–161041.4	...	202	18202930–1610411	ccc	3559	...	—	14.46	12.86	12.08	...	...	...	...
512	182029.31–161047.9	...	...	...	...	6070	...	—	14.77	12.93	12.11	...	...	...	...
513	182029.32–161045.2	...	...	...	...	6071	...	—	...	14.29	13.15	...	...	...	...
514	182029.36–160919.2	...	...	18202937–1609192	0cc	21537	...	—	...	14.99	14.27	...	...	...	...
515	182029.39–160943.0	98 (B4)	200	...	...	13962	G015.0707–00.6786	—	13.43	12.20	11.63	10.97	10.89	...	...
516	182029.39–161046.5	...	...	...	...	9296	...	—	14.79:	13.26	12.35	...	...	...	...
517	182029.39–161212.9	...	201	18202940–1612127	000	6619	...	—	13.04	12.10	11.72	...	...	...	...
518	182029.43–161050.2	...	...	...	...	6069	...	—	13.58	12.26	11.61	...	...	...	...
519	182029.48–161644.0	...	...	...	...	...	...	—	...	...	...	...	...	...	...
536	182029.81–161045.6	1 (O4+O4)	189	...	...	...	...	— <sub>536</sub>	...	...	...	...	...	...	...
543	182029.89–161044.5	1 (O4+O4)	189	18202986–1610449	00d	...	...	— <sub>536</sub>	7.24	6.29	5.75	...	...	...	...
567	182030.23–161034.9	61 (H:O9-B2)	181	18203022–1610349	000	7833	...	—	10.72	9.70	9.23	...	...	...	...
574	182030.44–161053.1	37 (H:O3-O6)	174	18203044–1610530	000	10398	...	— <sub>s-574</sub>	10.11	8.56	7.88	...	...	...	...

#### 2.4.1. Sources Without Stellar Counterparts

IR associations could not be found for 115 of the 886 X-ray sources. Their spatial locations are plotted as small diamonds in Figure 1a.

Visual examination of the SIRIUS and 2MASS images suggests that at least 14 of these probably have NIR associations that are not cataloged, either because the counterpart is only marginally resolved from a brighter star or because it lies near the limit of the NIR survey. Visual examination of the GLIMPSE image shows many point-like objects that are not listed in the Highly Reliable Catalog; thus some ACIS sources unidentified in Table 5 may have 3.6 – 8  $\mu\text{m}$  counterparts.

Extragalactic sources, mostly AGN at moderate redshifts, dominate X-ray source counts at high Galactic latitudes and some should be detected in Galactic plane fields despite the heavy obscuration. Getman et al. (2006a) and Wang et al. (2006) have quantitatively calculated the expected background contamination in ACIS observations of the Cepheus B and NGC 6357 star formation regions. In both cases, they predict that  $20 \pm 10$  sources should appear in a  $\sim 40$  ks ACIS exposure with dense Galactic cloud material, and only a few of those should be detectable in the IR. Some of these extragalactic sources are probably among the sources with spectra best fit by power law rather than thermal models (Table 4); as noted above, twelve of those sources lack IR counterparts. The spatial distribution of unassociated sources in Figure 1a is consistent with a random sprinkling of  $\sim 20$  extragalactic sources.

The remaining  $\sim 80$  ACIS sources without counterparts are likely to be new members of the M17 cloud complex. The high median energy of this unassociated population ( $E_{median} = 3.0$  keV) indicates that these sources are deeply embedded ( $A_V \gtrsim 15$  mag). Some are probably low mass stars with strong magnetic activity; several dozen such X-ray discovered stars were found in the cloud behind the Orion Nebula in the COUP study (Getman et al. 2005a). This interpretation is supported by their spatial distribution: Figure 1a shows that they are concentrated in the IR-bright North Bar and South Bar where IR surveys are most confused by nebular emission. Some of these may be very young with the local absorption in an envelope or disk, as suggested by Getman et al. for the COUP sources.

#### 2.4.2. NIR Properties of ACIS Sources

Following Hanson, Howarth, & Conti (1997, Figure 2), Figure 5 shows the NIR  $J - H$  vs.  $H - K$  color-color diagram for 609 out of 886 *Chandra* stars with high-quality (errors  $< 0.1$  mag)  $JHK$  photometry listed in Table 5. This plot is valuable for estimating the disk/envelope evolutionary class (I, II, or III, from Lada 1987) of protostars and young stellar objects. Most *Chandra* sources occupy the color space defined by the two leftmost dashed lines (rightward of the locus of main sequence stars, between these two reddening lines and including the extension of those lines to the upper right); this region of color space is associated with young stars lacking inner disks, referred to as Class III objects, which are reddened by interstellar extinction.

The  $\sim 100$  stars to the right of this reddened band are NIR excess sources; most occupy the color space between the middle and right-most dashed lines (including sources below the classical T Tauri star locus that would fall to the left of the rightmost reddening line if it was extended downward); this space is associated with pre-main sequence stars with circumstellar accretion disks, referred to as Class II objects. A handful of stars occupy the color space (rightward of the right-most dashed line and its downward extension) associated with protostars, referred to as Class I objects. The Herbig AeBe locus shows where these intermediate-mass pre-main sequence stars lie in color space; some IR excess sources could be HAeBe stars. The outlier #128

Table 5—Continued

Seq	X-ray	Optical/Infrared star						Infrared photometry							
	CXOU	CEN	B	2MASS	SIRIUS	GLIMPSE	Notes	J	H	K	[3.6]	[4.5]	[5.8]	[8.0]	
(1)	(2)	(3)	(4)	(5)	(6)	(7)	(8)	(mag)	(mag)	(mag)	(mag)	(mag)	(mag)	(mag)	
600	182030.95–161039.4	...	163	18203095–1610393 c00	6139	...	—600	12.86	10.99	9.76	...	...	...	...	
618	182031.35–160228.4	...	...	...	...	...	—618	...	...	...	...	...	...	...	
647	182031.84–161138.1	28 (B0)	150	18203184–1611383 000	8849	G015.0470–00.7023	—	12.24	11.71	11.40	10.40	9.94	9.36	7.68	
650	182031.89–161616.5	...	...	18203183–1616170 ss0	6300	G014.9787–00.7389	—650	12.61	10.95	9.57	7.75	...	6.84	6.38	
655	182031.97–161030.5	...	148	18203198–1610305 c00	6784	G015.0639–00.6940	—	15.63	13.58	12.63	11.55	11.61	...	...	
660	182032.06–160200.0	...	...	...	...	...	—660	...	...	...	...	...	...	...	
665	182032.34–160154.1	...	...	...	...	...	—665	...	...	...	...	...	...	...	
706	182034.56–161523.6	...	...	...	...	...	—	...	...	...	...	...	...	...	
726	182035.63–161055.5	45 (B1)	93	18203561–1610555 ccc	4442	G015.0646–00.7101	—	11.32	10.97	10.81	10.43	10.45	...	...	
854	182053.86–160306.5	...	...	18205385–1603063 000	20977	G015.2139–00.7131	—854	8.69	8.40	8.30	8.15	8.25	8.20	8.07	

Note. — Table 5 is published in its entirety in the electronic edition of the *Astrophysical Journal*. Interesting sources mentioned in the text are shown here for guidance regarding its form and content.

Note. — **Columns 1–2:** Source identification from Table 1. **Column 3:** Source number from Chini, Elsaesser, & Neckel (1980) and spectral type. Spectral types preceded by “H:” come from Hanson, Howarth, & Conti (1997); others come from SIMBAD, then Chini, Elsaesser, & Neckel (1980). **Column 4:** Source number from Hanson, Howarth, & Conti (1997) derived from Bumgardner (1992). A reference frame offset of  $1.9''$  between ACIS and Hanson, Howarth, & Conti (1997) positions was removed before matching the catalogs. **Column 5:** 2MASS designation. Three characters following the designation report the 2MASS Contamination and Confusion Flag defined in the Explanatory Supplement to the 2MASS All Sky Data Release at [http://www.ipac.caltech.edu/2mass/releases/allsky/doc/sec2\\_2a.html](http://www.ipac.caltech.edu/2mass/releases/allsky/doc/sec2_2a.html). **Column 6:** SIRIUS catalog running sequence number from Jiang et al. (2002). Sources outside the SIRIUS field of view are indicated by table note <sup>a</sup>. **Column 7:** GLIMPSE (a *Spitzer* legacy science program) designation. Sources are taken from the Highly Reliable Catalog, Version 1 at <http://www.astro.wisc.edu/sirtf/glimagesdata.html>. **Column 8:** Match ambiguity flags and notes on matches to other catalogs. An “s” in the first/second/third position indicates there are “secondary” (i.e. multiple) matches with the 2MASS/SIRIUS/GLIMPSE catalog respectively. **Columns 9–11:** JHK photometry. Values are generally taken from SIRIUS when a match is identified, or from 2MASS otherwise. However the bright sources #366, 701, 720, and 854 suffer saturation in the SIRIUS photometry so the 2MASS values are reported instead. Magnitudes have been corrected to the CIT photometry system (Elias et al. 1982). Annotation with : indicates reported photometry errors exceed 0.1 mag, 2MASS values are annotated by > when the 2MASS Photometric Quality Flag indicates a flux upper limit (flag=U), and are omitted when the flag indicates poor photometry (flag=E). **Columns 12–15:** Far infrared photometry taken from GLIMPSE. Median photometric errors for the reported counterparts are 0.13, 0.12, 0.16, 0.16 mag in the four bands. Maximum errors are 0.34, 0.32, 0.34, 0.35 mag.

is probably an interesting Class I protostar; it is a faint but very hard X-ray source.

Above the leftmost reddening line is the region of color space occupied by background giant stars (Hanson, Howarth, & Conti 1997). Simulations of X-ray detected background giants from the Cepheus B study (Getman et al. 2006a) showed that typically only  $\sim 3$  such objects should be detected in our M17 *Chandra* observation; the fact that more than 30 points occupy this region of color space in Figure 5 shows that such color-color diagrams are not definitive for classifying sources. NIR photometry can be contaminated by diffuse emission or crowding, causing pre-main sequence members of M17 to scatter into this region of color space.

As these classes are based solely on the NIR (*JHK*) spectral energy distributions (SEDs) of the sources, they reflect the evolutionary stage of inner disks. Our analysis is insensitive to the evolutionary status of centrally-cleared, outer disks. Thus our Class III status based on *JHK* colors for the known O9–B3 stars #186, 233, 296, and 488 is not in conflict with the Class I status given to these sources by Nielbock et al. (2001), whose classification is based on IR SEDs that extend out to 20  $\mu\text{m}$ , where outer disks can be detected.

Figure 6 shows the NIR *J* vs. *J – H* color-magnitude diagram for the same stars shown in Figure 5. This plot is valuable for estimating individual masses and reddening. Assuming that they lie on the 1 Myr isochrone, the majority of ACIS stars appear to be G and F stars ( $0.5 \lesssim M \lesssim 2 M_{\odot}$ ) reddened by  $3 \lesssim A_V \lesssim 15$  mag. Sources to the left of the 1 Myr isochrone may be older than the NGC 6618 population (§2.5) or may have contaminated photometry.

The drop off of stars towards higher masses is due to the stellar Initial Mass Function (IMF). The peak of the mass distribution in the figure is reasonably consistent with the mass completeness limit of  $1.7 M_{\odot}$  estimated in §3.2 for the lightly obscured population. Since the stellar IMF rises steeply towards a peak around  $M \sim 0.3\text{--}0.5 M_{\odot}$ , most of our X-ray sources are associated with stars having masses below our completeness limit. The minimum absorption of  $A_V \sim 3$  mag is consistent with the absorption reported in the M17 cluster (Chini, Elsaesser, & Neckel 1980). Approximately 40 stars are highly obscured with  $A_V \geq 20$  mag; other X-ray discovered members without NIR associations undoubtedly are even more obscured.

Table 6 lists 138 X-ray stars (from the sample of 609 high-quality counterparts) with dereddened mass estimates  $M \geq 2.0 M_{\odot}$ , ordered by mass. Appended to the table are five sources whose photometry has large errors but nevertheless strongly suggests that the stars are massive. Some massive stars cataloged in the literature are included in this table; they are marked with table notes. Some cataloged massive stars (from Tables 8 and 9) detected by *Chandra* are missing: ACIS #239, #322, #536, and #543 have no photometry available; ACIS #128, #182, #399, #647, and #726 have dereddened mass estimates less than  $2.0 M_{\odot}$ . We adopt the reddening law of Rieke & Lebofsky (1985)<sup>8</sup>. Note that inference of stellar masses and visual extinction from dereddening involves an ambiguity for stars within the mass range 2–4  $M_{\odot}$  (Figure 6) because the reddening vector intercepts the 1 Myr isochrone twice. Table 6 reports the lower of the two mass estimates. As a result there is an apparent gap between 4–10  $M_{\odot}$  in the reported mass distribution, and some reported masses in the range of 2–4  $M_{\odot}$  may be approximately one half their true values. The table also reports a NIR (*JHK*) SED classification for each object (Class I, II, or III described above) obtained from the color-color diagram. Of course, these class estimates refer only to hot inner disks and are subject to photometric uncertainties, so misclassifications are present. These approximate masses and classifications

---

<sup>8</sup> The abnormal reddening law of  $R_V = 4.8$  derived for M17 cloud material by Chini & Wargau (1998) should have little or no impact on the NIR extinction (Cardelli et al. 1989); thus we use the standard reddening law from Rieke & Lebofsky (1985).

are used in §3.1, §5.3, and §5.4.

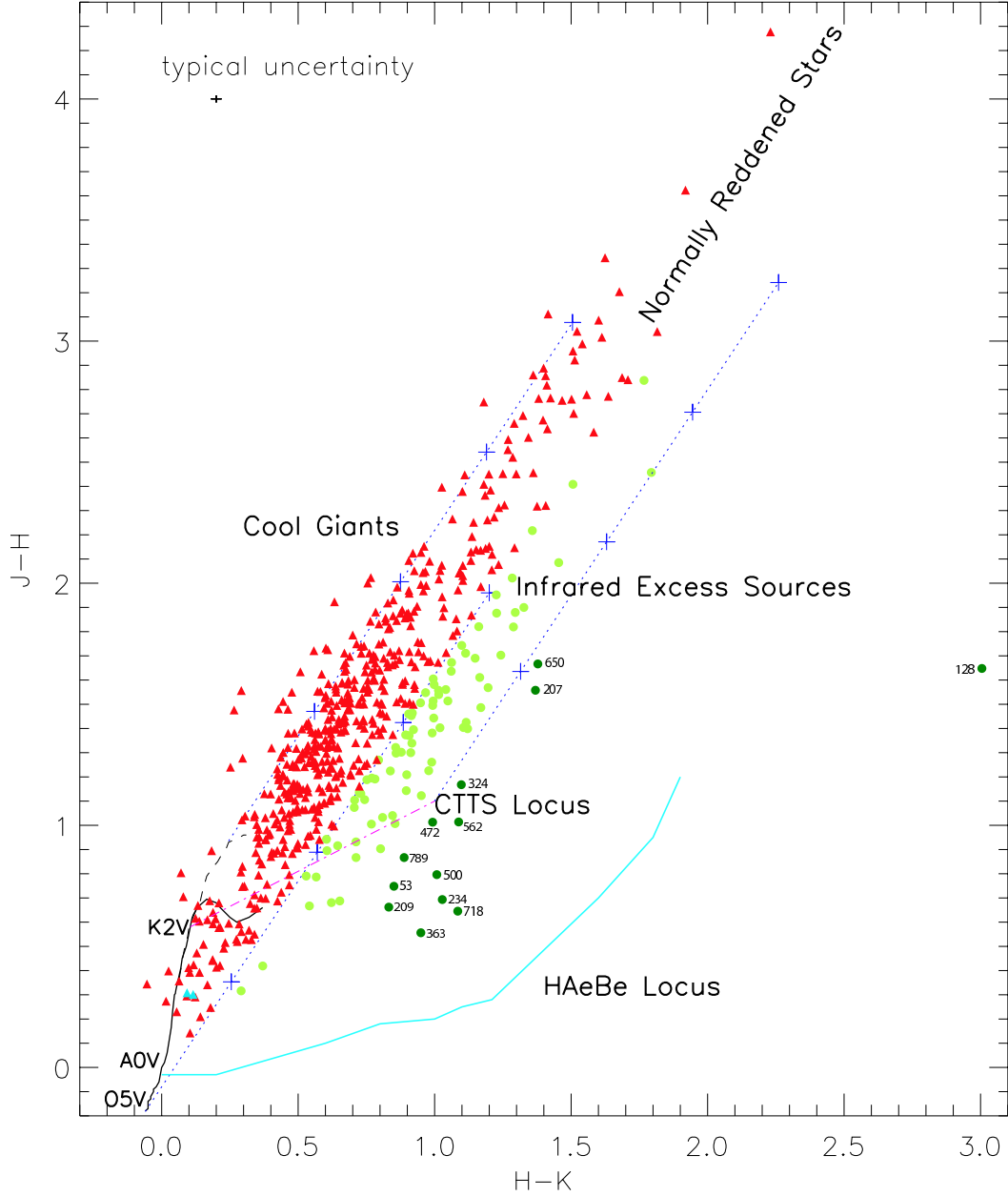


Fig. 5.— NIR color-color diagram. The (light and dark) green circles and red triangles represent sources with and without  $K$ -band excess, respectively. The dark green circles represent Class I objects, labeled by their ACIS sequence numbers. The two blue triangles are foreground stars (#281, #854, §5.3). The black solid and gray long-dash lines denote the loci of main sequence stars and giants, respectively, from Bessell & Brett (1988). The purple dash dotted line is the locus for classical T Tauri stars (CTTS; Class II pre-main sequence stars) from Meyer et al. (1997). The cyan solid line is the locus for HAeBe stars from Lada & Adams (1992). Three blue dashed lines (marked every 5 mag) are drawn parallel to a reddening vector with length  $A_V = 20$  mag, originating from the O5 dwarf, the M4 giant, and the end of the pre-main sequence locus.

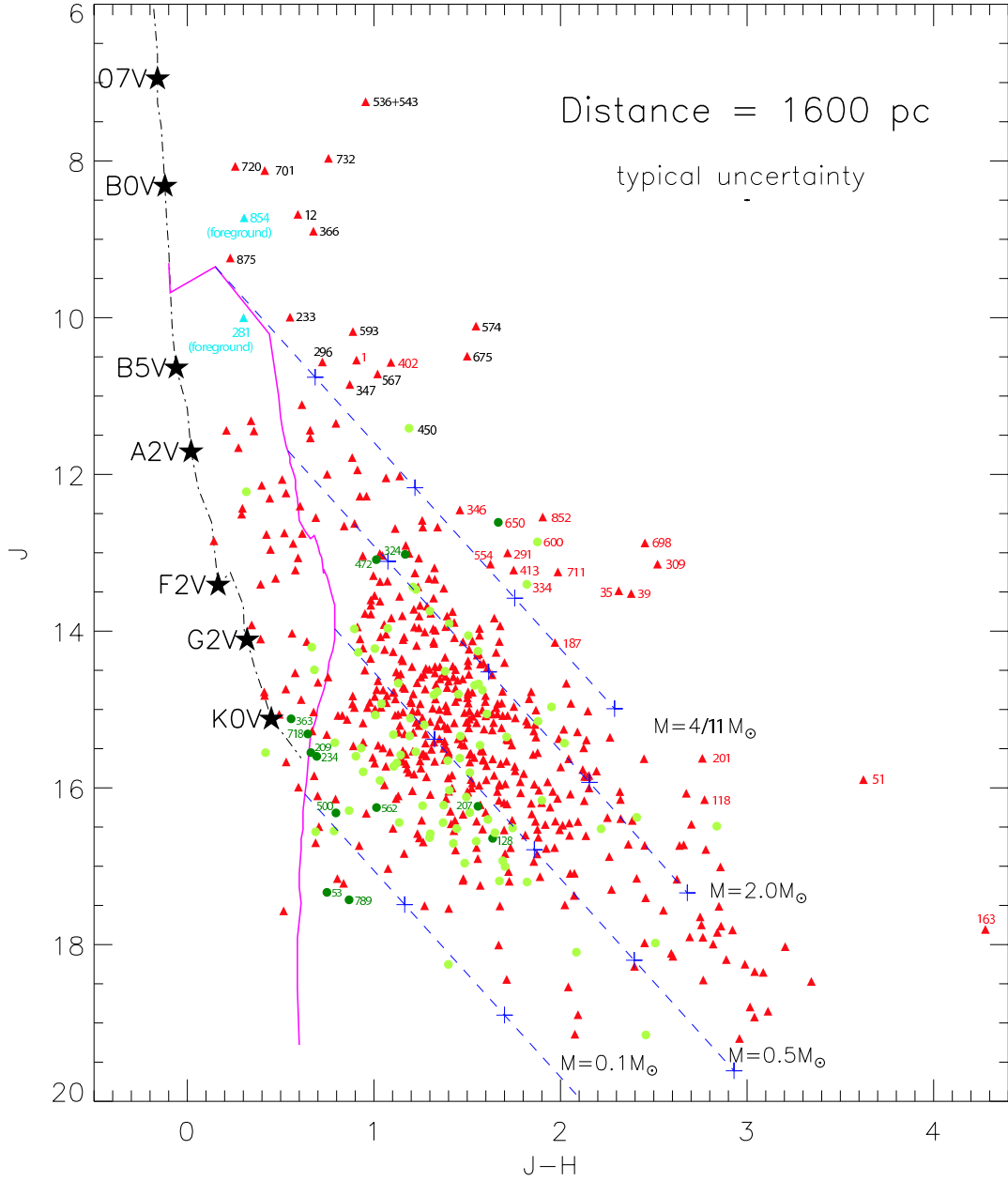


Fig. 6.— NIR  $J$  vs.  $J - H$  color-magnitude diagram. The (light and dark) green circles and red triangles represent sources with and without  $K$ -band excess, respectively. The dark green circles represent Class I objects, labeled by their ACIS sequence numbers. The two blue triangles are foreground stars (§5.3). The purple solid line is the 1 Myr isochrone from Siess et al. (2000) and Baraffe et al. (1998). The gray dash dotted line marks the location of Zero Age Main Sequence (ZAMS) stars; various spectral types are marked by black stars. The blue dashed lines represent the standard reddening vectors for various stellar masses, marked for every  $A_V = 5$  mag by the blue crosses. Sequence numbers for ACIS sources down to  $4 M_{\odot}$  are shown in black for cataloged OB stars (from Table 9) and in red otherwise. The O star #433 is among those omitted due to poor photometry. Sources #51 and #163 are discussed in §5.3. Typical uncertainties are shown graphically; the small median  $J$ -band uncertainty (0.02 mag) may be difficult to see.

Table 6. Photometrically Selected Intermediate- and High-Mass Stars

ACIS #	CXOU	$A_V$	Mass	Class
(1)	(2)	(mag)	( $M_\odot$ )	(est.)
		(3)	(4)	(5)
732 <sup>a</sup>	182035.87–161542.5	8.2	34.8	III
574 <sup>a</sup>	182030.44–161052.8	15.6	34.2	III
51	182012.31–160447.4	35.0	31.0	III
698	182034.40–160938.8	24.1	30.4	III
309 <sup>b</sup>	182024.60–161139.0	24.7	29.4	III
675 <sup>a</sup>	182033.06–161121.3	15.2	29.0	III
163	182020.74–160717.7	41.1	29.0	III
12 <sup>a</sup>	182003.04–160206.5	6.7	23.0	III
39	182010.50–160528.6	23.4	21.8	III
35	182009.19–161430.9	22.7	20.5	III
701 <sup>a</sup>	182034.49–161011.6	4.2	20.5	III
852	182053.43–161210.1	18.9	19.5	III
366 <sup>a</sup>	182025.86–160832.1	6.4	18.8	III
720 <sup>a</sup>	182035.39–161048.2	6.4	18.6	III
402	182026.66–160708.6	11.3	18.3	III
593 <sup>a</sup>	182030.84–161007.2	9.4	17.3	III
600 <sup>c</sup>	182030.95–161039.1	18.6	16.8	II
711	182034.85–160626.2	19.6	16.2	III
567 <sup>a</sup>	182030.23–161034.7	10.6	16.1	III
1	181957.56–161204.3	9.5	15.3	III
650	182031.89–161616.2	16.6	14.9	I
450 <sup>a</sup>	182027.80–161101.4	12.2	14.6	II
201	182021.82–161123.4	26.9	14.2	III
291	182024.33–161352.8	17.1	13.6	III
347 <sup>a</sup>	182025.44–161115.5	9.2	13.2	III
233 <sup>a</sup>	182022.70–160833.6	6.2	13.2	III
413	182026.96–160347.3	17.4	12.9	III
346	182025.42–161118.6	14.7	12.9	III
334	182025.08–161133.7	18.0	12.9	II
875 <sup>a</sup>	182101.07–160546.7	3.2	12.8	III
296 <sup>a</sup>	182024.39–160843.0	7.8	12.7	III
118	182019.25–161326.4	26.9	11.8	III
554	182030.03–161034.5	16.2	11.7	III
187	182021.44–161206.6	19.4	11.3	III
757	182037.62–160332.3	21.7	3.7	III
27	182008.25–160552.5	7.4	3.7	III
691	182034.02–160800.6	23.5	3.7	II
817	182043.77–161330.1	18.7	3.4	III
813	182043.42–161245.9	5.7	3.4	III
488 <sup>a</sup>	182028.66–161211.3	3.2	3.4	III
466 <sup>a</sup>	182028.15–161049.1	8.4	3.4	III
608 <sup>a</sup>	182031.12–160929.6	7.5	3.3	III
582	182030.64–161028.3	16.8	3.3	III
560	182030.15–161055.6	15.7	3.3	III
507 <sup>a</sup>	182029.17–160942.8	7.5	3.3	III
438	182027.62–161043.0	20.9	3.3	III
307	182024.56–161127.5	14.7	3.3	III
588	182030.73–161101.4	22.3	3.2	III
456	182027.86–160955.3	1.3	3.2	III
375	182026.02–161239.8	14.8	3.2	III
288	182024.23–161109.3	11.2	3.2	III
229	182022.58–161024.5	10.9	3.2	III
186 <sup>a</sup>	182021.43–160938.8	3.9	3.2	III
83	182016.84–160729.0	21.6	3.2	III
506	182029.14–161054.0	4.1	3.1	III
206	182021.92–161412.3	25.5	3.1	III
763	182038.02–160310.5	26.7	3.0	III
687	182033.76–161304.6	7.8	3.0	III
678	182033.21–161058.1	11.0	3.0	III
677	182033.17–160746.3	15.4	3.0	III
526	182029.61–160603.5	20.3	3.0	III
508	182029.20–161110.7	1.6	3.0	III
495 <sup>a</sup>	182028.87–161041.7	5.8	3.0	III
343	182025.32–160939.4	4.4	3.0	III
649	182031.86–161047.1	20.0	2.9	III
638 <sup>a</sup>	182031.70–160945.6	7.0	2.9	III
376 <sup>a</sup>	182026.04–161104.3	1.5	2.9	III
350 <sup>a</sup>	182025.50–161053.6	8.2	2.9	III
312 <sup>a</sup>	182024.62–161108.4	6.3	2.9	III
253	182023.13–161131.8	14.9	2.9	III
682	182033.43–161042.5	13.6	2.9	II
783	182039.71–161312.5	7.8	2.8	III
595	182030.89–160904.9	10.0	2.8	III
505	182029.12–161247.2	15.2	2.8	III
496 <sup>a</sup>	182028.87–161109.8	6.5	2.8	III
423	182027.20–160420.6	10.8	2.8	III
408	182026.82–160749.3	4.0	2.8	III

Table 6—Continued

ACIS #	CXOU	$A_V$ (mag)	Mass ( $M_\odot$ )	Class (est.)
(1)	(2)	(3)	(4)	(5)
645	182031.82–161123.6	11.2	2.7	III
564	182030.19–161213.4	17.0	2.7	III
512	182029.32–161047.7	12.6	2.7	III
406 <sup>a</sup>	182026.79–161057.8	7.4	2.7	III
273	182023.76–161101.2	10.0	2.7	III
105	182018.44–161418.7	14.2	2.7	III
324	182024.87–161127.2	6.2	2.7	I
771	182038.82–160604.6	21.9	2.6	III
727	182035.67–160242.5	8.6	2.6	III
607	182031.09–161125.9	17.0	2.6	III
549	182029.95–160953.5	6.7	2.6	III
489	182028.67–160926.0	2.3	2.6	III
179	182021.25–160944.1	15.8	2.6	III
150	182020.32–160237.1	12.4	2.6	III
57	182012.96–161308.1	17.8	2.6	II
800	182041.79–160241.7	9.5	2.5	III
518	182029.44–161049.9	7.5	2.5	III
305	182024.54–160737.4	12.7	2.5	III
710	182034.83–160750.9	9.3	2.5	II
592	182030.80–161041.8	14.1	2.5	II
758	182037.78–160427.1	22.5	2.4	III
568	182030.28–161131.2	8.6	2.4	III
538	182029.82–160957.0	9.7	2.4	III
401	182026.65–160310.3	17.5	2.4	III
30	182008.44–161409.4	8.2	2.4	III
16	182004.72–160937.1	13.8	2.4	III
285	182024.10–160839.9	9.7	2.4	II
628	182031.52–160910.1	9.6	2.3	III
515	182029.39–160942.7	6.7	2.3	III
368	182025.87–160922.9	15.2	2.3	III
236	182022.75–161123.2	9.7	2.3	III
137	182019.95–160805.0	14.9	2.3	III
21	182006.33–160453.5	15.1	2.3	III
537	182029.82–161057.2	12.7	2.3	II
335	182025.10–161129.4	8.2	2.3	II
668	182032.48–161047.0	21.8	2.2	III
655	182031.98–161030.2	14.1	2.2	III
555	182030.04–161233.9	14.9	2.2	III
511	182029.29–161041.2	10.1	2.2	III
437	182027.59–161133.3	10.3	2.2	III
435	182027.48–161013.2	3.4	2.2	III
374	182026.01–161022.1	8.9	2.2	III
310	182024.60–161046.1	9.1	2.2	III
264	182023.44–160953.1	9.9	2.2	III
113	182019.06–160629.3	19.6	2.2	III
94	182017.82–160453.1	23.9	2.2	III
680	182033.39–160918.6	6.3	2.2	II
654	182031.97–160924.9	6.5	2.2	II
717	182035.29–161118.4	7.9	2.1	III
694	182034.08–161044.3	4.6	2.1	III
681	182033.41–161115.6	9.6	2.1	III
534	182029.76–160936.3	7.0	2.1	III
434	182027.47–161358.4	4.7	2.1	III
200	182021.79–161041.8	16.7	2.1	III
159	182020.55–160738.0	12.4	2.1	III
142	182020.03–161330.8	17.9	2.1	III
804	182042.04–161107.2	15.0	2.0	III
262	182023.34–160512.8	23.3	2.0	III
225	182022.49–160951.5	10.7	2.0	III
192	182021.62–160924.5	8.3	2.0	III
359	182025.73–161045.8	7.0	2.0	II
7 <sup>d</sup>	182000.65–161112.0	...	...	...
9 <sup>e</sup>	182001.73–160529.0	...	...	...
398 <sup>b</sup> f	182026.62–161136.5	...	4:	...
433 <sup>a</sup> f	182027.41–161331.0	...	>4	...
539 <sup>f</sup>	182029.84–161041.3	...	4:	...

Note. — **Columns 1–2:** Source identification from Table 1.  
**Columns 3–4:** Visual absorption and mass, derived from dereddened location in color-magnitude diagram along the standard interstellar reddening vector.  
**Column 5:** Suggested disk/envelope evolutionary class (see text) based on source’s position in NIR color-color diagram (Figure 5). ACIS #281 and #854 are likely foreground stars (§5.3) and are omitted. ACIS #123 and #543 have inaccurate photometry and are omitted.

<sup>a</sup>Historically recognized OB stars from Table 9.

<sup>b</sup>High-mass Class I source from Table 8.

<sup>c</sup>ACIS #600 is B 163 in Hanson, Howarth, & Conti (1997) and is listed in their Table 6 as a candidate young stellar object.

<sup>d</sup>*J*-band photometry is not available, however source is bright in *K*-band (10.9 mag) and is likely massive.

<sup>e</sup>*J*-band photometry is not available, however source is bright in *K*-band (9.9 mag) and is likely massive.

<sup>f</sup>Photometry has large errors.

## 2.5. X-ray sources not associated with M17

Approximately 20 extragalactic sources are expected to appear in our ACIS catalog (§2.4.1). An additional  $\sim 20$  foreground stars are expected to appear in the catalog, based on extrapolation of foreground contamination simulations presented by Getman et al. (2006a) and Wang et al. (2006). This is roughly consistent with the population of sources observed between the 1My isochrone and the zero-age main sequence (ZAMS) track in the color-magnitude diagram discussed in §2.4.2 (Figure 6). Additionally, some of those sources show large proper motions in the UCAC2 catalog (Zacharias et al. 2004) and/or are faint, soft, minimally-absorbed X-ray sources. Thus, in total  $\sim 5\%$  of our catalog of 886 ACIS sources are expected to be unrelated to the M17 star forming region. We postpone a detailed membership study until we have a longer ACIS observation of M17, where the X-ray spectra will be better characterized and more useful for identifying the unrelated populations.

## 3. Global Properties of the Stellar Populations

The COUP study of the Orion Nebula Cluster, whose membership was reliably known in advance from many optical and NIR studies, shows a strong statistical association between X-ray luminosity and stellar mass in lower mass ( $M \leq 3 M_{\odot}$ ) pre-main sequence stars (Preibisch et al. 2005a). This relationship is confirmed in other young stellar clusters such as Cep OB3b and Cep B (Getman et al. 2006a) and NGC 2264 (Flaccomio et al. 2006; Rebull et al. 2006). The astrophysical origin of the relation is uncertain: it may arise from internal dynamo processes (Preibisch et al. 2005a) or constraints on the external magnetic coronae (Jardine et al. 2006).

However, the empirical  $L_x - M$  correlation means that X-ray catalogs should give a surprisingly complete census of lightly obscured cloud members down to a mass limit dependent on the  $L_x$  limit of the observation (Feigelson et al. 2005; Getman et al. 2006a). Our census of the lightly obscured M17 population is complete down to a hard-band X-ray luminosity of  $\log L_{h,c} \sim 30.5 \text{ ergs s}^{-1}$  (§3.2). Assuming that the M17 stars follow the same empirical  $L_{h,c} - M$  relation as the Orion population (Preibisch et al. 2005a; Getman et al. 2006a), that completeness limit roughly corresponds to a mass of  $1.7 M_{\odot}$ . This is achieved with  $< 5\%$  contamination from non-cluster members (§2.5).

A second critical point is that X-ray emission arises primarily from magnetic flaring and thus X-ray selected samples are relatively unbiased with respect to the presence or absence of circumstellar disks (Feigelson et al. 2006). Some systematic effects are present— Class II stars (systems with accretion disks) are systematically  $\sim 2$  times fainter than Class III stars (systems with weak or absent disks) in the same mass stratum, and a soft X-ray component from accretion may be occasionally seen—but these are relatively small (Preibisch et al. 2005a). Thus the X-ray sample complements IR population studies that often rely on the presence of warm dusty disks, although X-ray studies are less complete for the lowest mass objects. From the *JHK* photometric study of the SIRIUS field (somewhat smaller than the ACIS field), Jiang et al. (2002) identified 454 Class I protostars, 2798 Class II/III pre-main sequence stars, and 281 OB candidates. The Class I objects are concentrated along the North Bar and South Bar in the HII region. The Class II/III stars are distributed widely across the field with a deficit in the M17-SW region attributable to heavy absorption.

### 3.1. Spatial Distribution of X-ray Stars in M17

Figure 7 shows the distribution of X-ray stars in the ACIS field, both as individual stars and smoothed with a box kernel of width  $30''$ . The low obscuration and high obscuration sources are discriminated by their spectra as those with median energy below and above 2.5 keV respectively. This criterion corresponds to an absorption of  $\log N_H \sim 22.3 \text{ cm}^{-2}$  or  $A_V \sim 10 \text{ mag}$  (Feigelson et al. 2005).

The lightly obscured population shows a simple, centrally concentrated structure centered at  $(\alpha, \delta) = (18^h 20^m 28^s, -16^\circ 10' 50'')$ . This lies about  $30''$  (0.2 pc projected) west of the O4+O4 binary CEN 1 (ACIS #536 and 543; the field center is shown in §5). The B2 star CEN 85 (ACIS #466) coincides with the center of the cluster distribution. The inner  $2'$  (0.9 pc) radius appears spherical, but the distribution becomes elongated towards the northwest around  $2'-4'$  from the center. The central concentration of the cluster (surface stellar density  $> 1$  per arcmin<sup>2</sup>) traced by the ACIS sources is  $\sim 8' \times 6'$  ( $\sim 4 \times 3$  pc).

Several features are seen in the stellar surface density map for the heavily obscured population (Figure 7*b,d*).

1. The highest concentration of stars ( $\sim 40$ ) coincides with the main centrally concentrated cluster seen in Figure 7*a,c*. This is undoubtedly the same physical structure exhibiting a wide range of obscuration.
2. A secondary stellar concentration ( $\sim 14$  stars) is located northwest of the cluster center at  $(18^h 20^m 22^s, -16^\circ 07' 30'')$  with  $3'$  (1.4 pc) diameter. This may be part of the northwest elongation seen in the lightly obscured population, but there is a distinct dip in stellar density between it and the central cluster. This cannot be attributed to absorption: there is a band of CO-emitting molecular material west and north of the secondary stellar concentration, but none is seen in the dip region, as shown in Figure 1*b*. We label this secondary stellar group M17-X in Figure 7*d*, where “X” indicates X-ray discovered, as it was not previously noted in IR studies. As this concentration is based on only 14 stars, its reliability is uncertain.
3. High-density enhancements ( $\sim 40$  stars) in the X-ray star density extend from the main cluster  $3'$  towards the west and  $4'$  to the southwest. The densest portion of this enhancement coincides with M17-UC1 (§4.1) and it ends around the KWO (§4.2). This arcuate distribution runs along the eastern edge of the M17-SW molecular core, following a very similar distribution of Class I protostellar candidates found by Jiang et al. (2002). This is an independent detection of this elongated stellar structure; only a handful of the ACIS stars are SIRIUS Class I candidates. The ACIS enhancement thus gives a clear view of the spatial distribution of the triggered stellar population along the shock front between the M17 HII region and the M17-SW molecular core.
4. A stellar concentration (10–15 stars) is present at the northern edge of the ACIS field, corresponding to the embedded M17-North group of protostars (§4.3).

The spatial distributions of the intermediate- and high-mass stars detected by *Chandra* are shown in Figure 8 based on mass estimates described in §2.4.2 and Table 6. As expected, the highest concentration of massive stars is located around the known bright O stars in NGC 6618. Other concentrations of interest include: M17-SW centered on  $(18^h 20^m 24^s, -16^\circ 11' 30'')$  around UC1 (§4.1), and a tight grouping of three stars around the KWO (§4.2).

It is also important to note that several dozen intermediate- and high-mass stars are distributed widely throughout the ACIS field. These mostly are lightly obscured and several were identified as possible OB

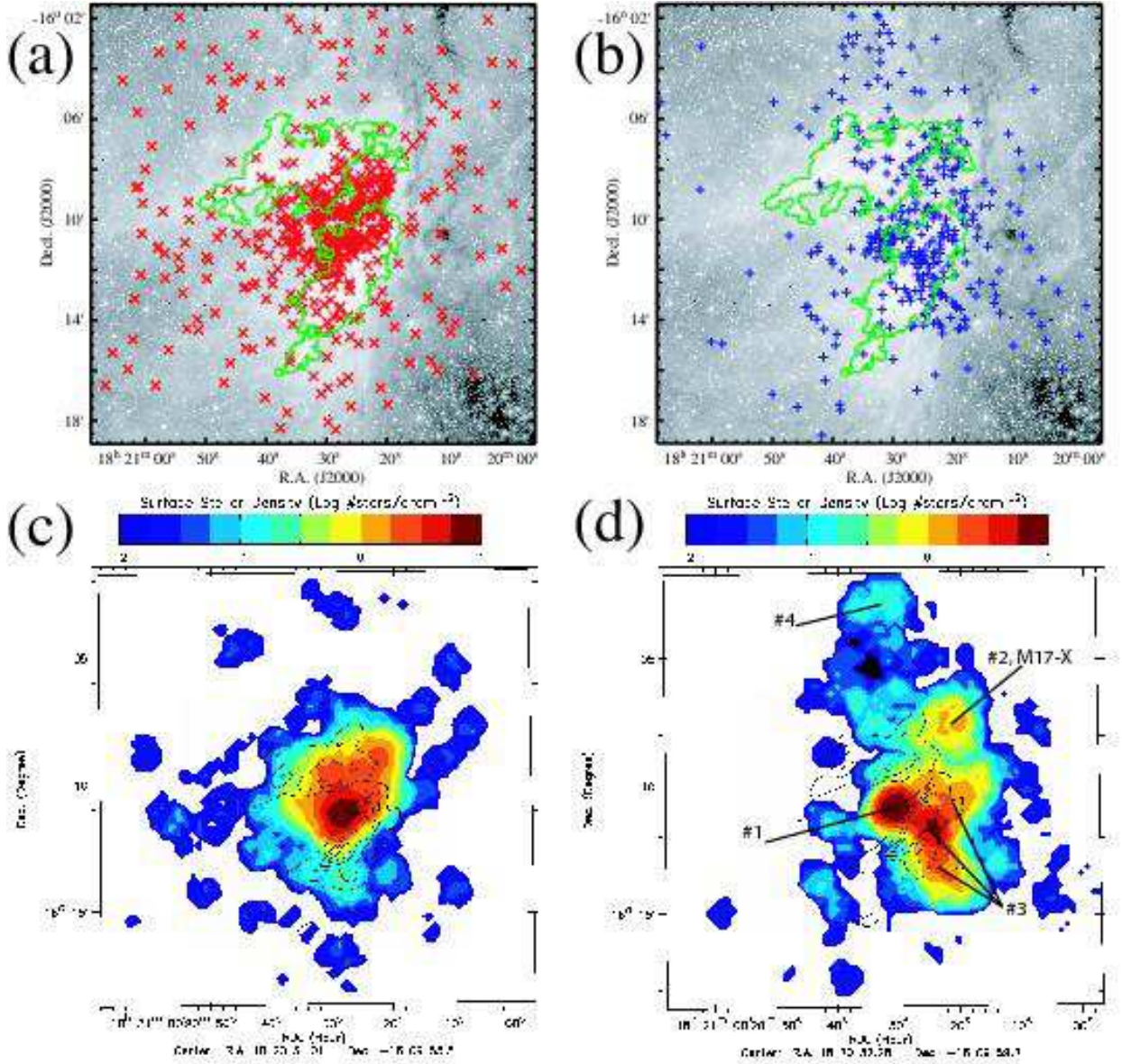


Fig. 7.— Spatial distribution of ACIS X-ray sources. The left-hand panels show the lightly obscured population ( $E_{median} < 2.5$  keV or  $A_V \leq 10$  mag), and the right-hand panels show the heavily obscured population ( $E_{median} > 2.5$  keV or  $A_V \geq 10$  mag). The top panels show the individual star positions superposed on the *Spitzer* GLIMPSE  $3.6 \mu\text{m}$  grayscale image, with green contours outlining the North Bar and South Bar in the HII region. The bottom panels show a map of the stellar surface density after smoothing with a  $30''$  radius kernel; contours from the *MSX*  $8 \mu\text{m}$  map are overlaid to show the North Bar and South Bar. Four structures discussed in §3.1 are labeled in panel (d); structure #2 is the newly identified M17-X embedded cluster.

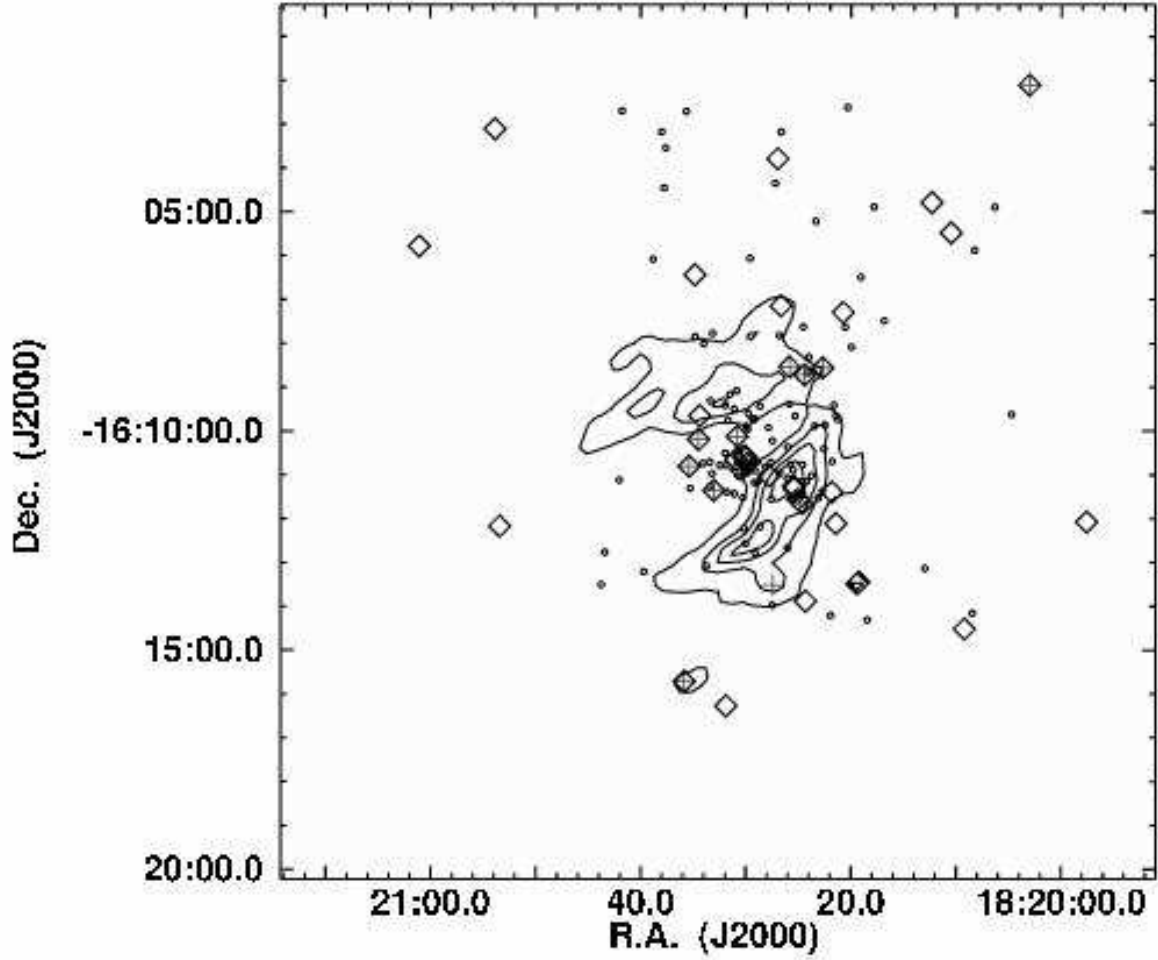


Fig. 8.— Spatial distribution of X-ray selected intermediate-mass stars ( $2 \lesssim M \lesssim 8 M_{\odot}$ , small circles) and high-mass stars ( $M \gtrsim 8 M_{\odot}$ , diamonds). The  $MSX 8\mu m$  contours are overlaid. The pluses mark previously known O stars (§5 and Table 9); the known O star not marked as high-mass (missing its diamond) was detected (ACIS #433  $\leftrightarrow$  OI 345) but no mass estimate is reported in Table 6 due to large photometry errors.

stars from the early *UBV* photometric study of Ogura & Ishida (1976). Most of these stars do not appear to be extremely young. Among the intermediate-mass stars,  $\sim 100$  have NIR colors consistent with reddened Class III objects while about a dozen have *K*-band excesses characteristic of Herbig Ae/Be stars (Figure 5).

### 3.2. Quantifying the Stellar Population with the XLF

Establishing and understanding the Initial Mass Function (IMF) that arises from star formation processes are major goals underlying studies of young stellar clusters (Corbelli et al. 2005). This effort is subject to a variety of difficulties. One of the major problems is the huge level of background and foreground contamination seen in optical and NIR observations of most clusters. Statistical correction for contamination using observations of nearby control fields or using Galactic stellar models can give uncertain results. Jiang et al. (2002) used Galactic models of foreground and (extinguished) background stellar populations to correct the observed *K*-band luminosity function (KLF) in regions of the SIRIUS field. The results were satisfactory in the limited mass range  $0.5 \lesssim M \lesssim 2 M_{\odot}$ , but uncertainties in contamination affected the IMF measurement at higher masses. For example, Jiang et al. found that it was not possible to derive a corrected KLF for region 2C (Figure 1) where the estimated NIR contamination was higher than the number of detected stars.

X-ray surveys, on the other hand, suffer relatively little contamination (§2.5), and the statistical link between X-ray luminosities and masses (§3) permits an association between the X-ray Luminosity Function (XLF) and the IMF. This idea was recently proposed (Feigelson & Getman 2005) and applied to *Chandra* populations in the OMC-1 (Grosso et al. 2005), Cep B/Cep OB3b (Getman et al. 2006a) and NGC 6357 (Wang et al. 2006) regions. Through their independent analyses, Getman et al. further confirm the tight connection between the XLF and the IMF.

As the total band luminosity systematically underestimates the true emission for obscured objects due to the absence of soft band photons, we restrict our analysis to the X-ray luminosities in the hard (2–8) keV energy band: the observed luminosity  $L_h$  and that corrected for absorption  $L_{h,c}$ . These quantities are available for  $\sim 600$  of the brighter sources in M17 (§2.3).

Following the approach taken in Getman et al. (2006a) and in §3.1, we divide the 886 M17 ACIS X-ray sources into 514 lightly obscured and 372 heavily obscured samples using a threshold of median energy  $E_{median} = 2.5$  keV, corresponding to  $A_V \sim 10$  mag. Figure 7 shows the spatial distributions of these two samples and Figure 9 shows the XLF comparison analysis for these samples using the absorption corrected X-ray luminosity  $L_{h,c}$ . For brevity, the similar analysis using  $L_h$  is not described in detail. The  $\sim 5\%$  contamination due to unrelated Galactic or extragalactic sources (§2.5) is ignored in the following analysis.

The lightly obscured Orion Nebula Cluster (ONC) has both the XLF and IMF accurately measured (Feigelson et al. 2005; Getman et al. 2006a). We assume here, as in Getman et al. (2006a) and Wang et al. (2006), that the XLFs of young stellar clusters have the same powerlaw slope at high luminosity and thus the ONC can reasonably serve as a calibrator for more distant clusters. XLFs should be relatively insensitive to age effects; Preibisch & Feigelson (2005) found only a slight ( $\sim 0.3$  in  $\log L_t$ ) decline in luminosity between 1 and 10 Myr old ONC populations. Specifically, the ONC comparison sample consists of 839 COUP cloud members, excluding OB stars and sources with absorbing column density  $\log N_H > 22.0 \text{ cm}^{-2}$ . The ONC sample is nearly complete down to  $0.1 M_{\odot}$  and about 50% complete within the low-mass stellar-sub-stellar range of  $0.03\text{-}0.1 M_{\odot}$  (Preibisch et al. 2005b; Getman et al. 2006a).

Luminosities are available for 70% (361 out of 514) and 63% (234 out of 372) of the lightly and heavily

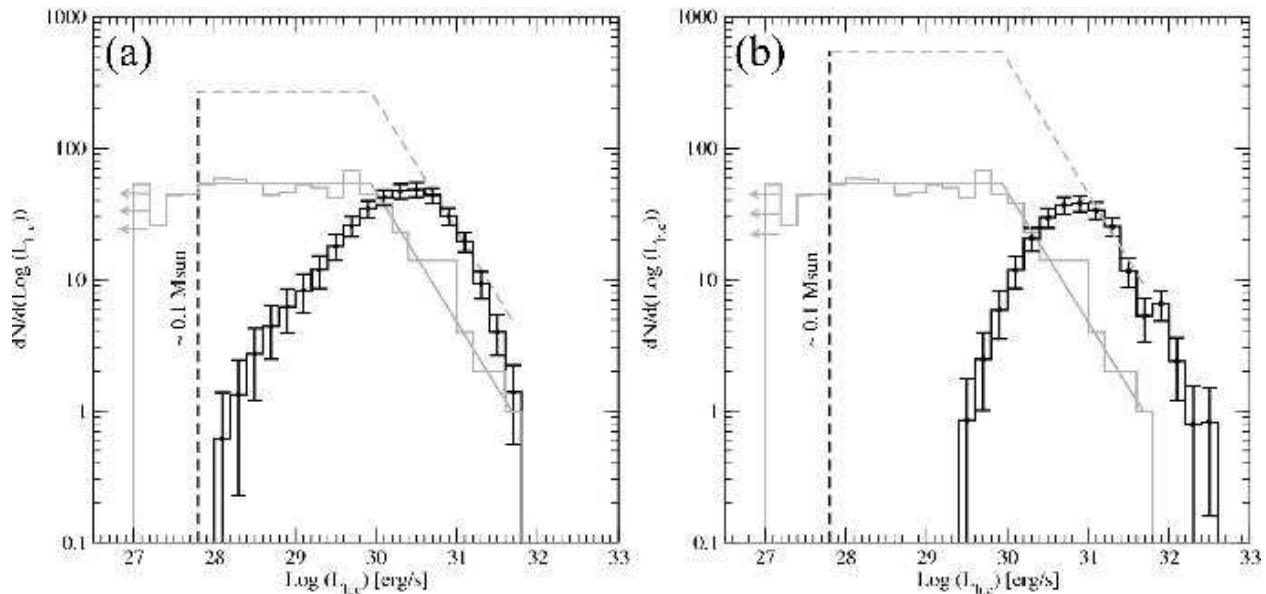


Fig. 9.— Hard band X-ray luminosity functions (corrected for absorption) of the lightly obscured (black histogram with error bars, left panel) and heavily obscured (right panel) samples of X-ray sources in M17. A calibration XLF from the Orion Nebula Cluster is shown as the gray histogram; luminosities below  $10^{27}$  ergs/s occupy the left-most bin. Regression lines to the ONC XLF (gray, solid lines) were scaled upward to match the M17 XLFs (gray, dashed lines). The ONC sample is 100% complete down to  $\sim 0.1 M_{\odot}$  (black dashed line).

obscured M17 samples, respectively. Uncertainties,  $\Delta \log L_{h,c}$ , are estimated for each luminosity based on the number of detected counts, using the simulated flux vs. flux uncertainty correlation from Figure 12 of Getman et al. (2006a).

Examination of Figure 9 shows that the ONC and M17 XLFs are nearly parallel at the high luminosity end, and the M17 source counts turn over due to completeness limits around  $\log L_{h,c} \sim 30.5$  ergs  $s^{-1}$  ( $M \sim 1.7 M_{\odot}$ ) for the lightly obscured sample and  $\log L_{h,c} \sim 30.9$  ergs  $s^{-1}$  ( $M \sim 2.6 M_{\odot}$ ) for the heavily obscured sample. We thus scale the ONC XLF regression line vertically upward to estimate the total population of M17 in the ACIS field. Due to systematic uncertainties, the XLF- $L_h$  and XLF- $L_{h,c}$  analyses provide slightly different estimates for the total population of the lightly obscured sample in M17 down to  $0.1 M_{\odot}$ , so we report a range for this quantity of 2500 – 3500 stars. About 60% of this population lies in the concentrated NGC 6618 cluster. Similar uncertainty for the heavily obscured population gives an estimated range of 5000 – 7000 obscured objects. Thus the total estimated population of young objects in M17 down to  $0.1 M_{\odot}$  within the  $17' \times 17'$  ACIS-I field is 7500–10500 stars.

## 4. X-rays from embedded populations

### 4.1. The M17-UC1 region

Radio and IR studies have shown that star formation around the M17 HII region is most active in the M17-SW cloud. The best-studied subregion is around the massive binary IRS 5N and 5S with separation  $5''$  (e.g. Felli et al. 1984; Johnson, Depree, & Goss 1998; Chini, Nielbock, & Beck 2000; Nielbock et al. 2001). IRS 5N has bolometric luminosity  $L_{bol} \sim 5000 L_{\odot}$  peaking in the MIR and ionizes the rapidly evolving ultracompact HII region M17-UC1  $\Leftrightarrow$  G15.04-0.68. IRS 5S with  $L_{bol} \sim 2000 L_{\odot}$  is radio-quiet and less absorbed. They appear to be massive Class I protostars, probably early-B stars. The interstellar matter around these central stars is complex with dense dusty cloud clumps and an arc-shaped ionization front.

The top panels of Figure 10 show the deep  $K$  and *Chandra* images of IRS 5 and its vicinity. ACIS #322 did not arise from the source finding process but was manually added to the catalog at the known position of the MIR source IRS 5N  $\Leftrightarrow$  UC 1. Although its formal detection significance (column 13 of Table 2) is low (0.9), confidence that X-ray emission is seen at that position is bolstered by the fact that the 5 nearby X-ray photons are harder ( $E_{median} = 4.7$  keV) than the local background ( $E_{median} = 3.5$  keV). IRS 5S (#309) is definitely present with 19 photons. Its X-ray spectrum indicates absorption of  $\log N_H \sim 22.8$   $\text{cm}^{-2}$  and intrinsic (absorption-corrected) hard band luminosity  $\log L_{h,c} \sim 30.9$   $\text{ergs s}^{-1}$ . This source was recently resolved into 3 components using a high-resolution  $K$ -band image (Chini et al. 2005); the X-ray source is spatially associated with the brightest  $K$ -band component.

A cluster of  $\sim 20$  X-ray stars is present within  $20''$  (0.15 pc) radius of the IRS 5 binary, most with NIR counterparts. These sources are heavily absorbed and have intrinsic X-ray luminosities near the top of the XLF. Source #324 is associated with the NIR star B 279 ( $K = 10.75$  mag) which is likely responsible for powerful methanol and OH masers (Norris et al. 1987). It emits  $\log L_{h,c} \sim 30.9$   $\text{ergs s}^{-1}$  with absorption  $\log N_H \sim 22.4$   $\text{cm}^{-2}$ . Source #334 is associated with the IR star B 273 with  $K = 10.3$  mag and strong CO bandhead absorption but no emission lines (Chini et al. 2005). It emits  $\log L_{h,c} \sim 30.5$   $\text{ergs s}^{-1}$  with  $\log N_H \sim 22.4$   $\text{cm}^{-2}$ . Chini et al. interpret this source as an FU Orionis type object, a massive young star with heavy accretion.

This concentration of  $\sim 20$  X-ray luminous stars around IRS 5 has about 1/5 the number of similarly luminous stars seen in the lightly obscured NGC 6618 cluster (§3.2), implying that the total population of the embedded cluster is  $\sim 300$  stars. Source #329, one of the weaker X-ray sources in the region, showed flaring behavior and is probably one of these lower mass stars. However, this inference is quite uncertain, and inconsistent with the relatively small population found in the Becklin-Neugebauer region behind the Orion Nebula which is similar to the M17-SW IRS 5/UC1 complex. In Orion, the deep COUP image shows only a sparse cluster of lower mass stars accompanying the IR-luminous group of proto-B stars (Grosso et al. 2005). We look forward to more directly measuring the population around IRS 5 in an upcoming deeper *Chandra* observation.

A group of dense molecular cores (Peak 3 in the survey of Vallée & Bastien 1996) and masers are concentrated about  $30''$  west of M17-UC1. Johnson, Depree, & Goss (1998) argue that this region is the one most recently triggered by the shock from the main M17 HII region. Two ACIS sources (#239 and #244) are positionally coincident with the luminous Class I IR source Anon 1 (§4.4), reported by Nielbock et al. (2001) to have an extremely steep spectral index. The properties of source #239 suggest it is the more likely true association; it is unusually X-ray luminous, constant, and heavily absorbed ( $\log L_{h,c} \sim 31.7$   $\text{ergs s}^{-1}$  and  $\log N_H \sim 23.5$   $\text{cm}^{-2}$ ), and has no identified NIR or MIR counterpart. The observed absorption is roughly

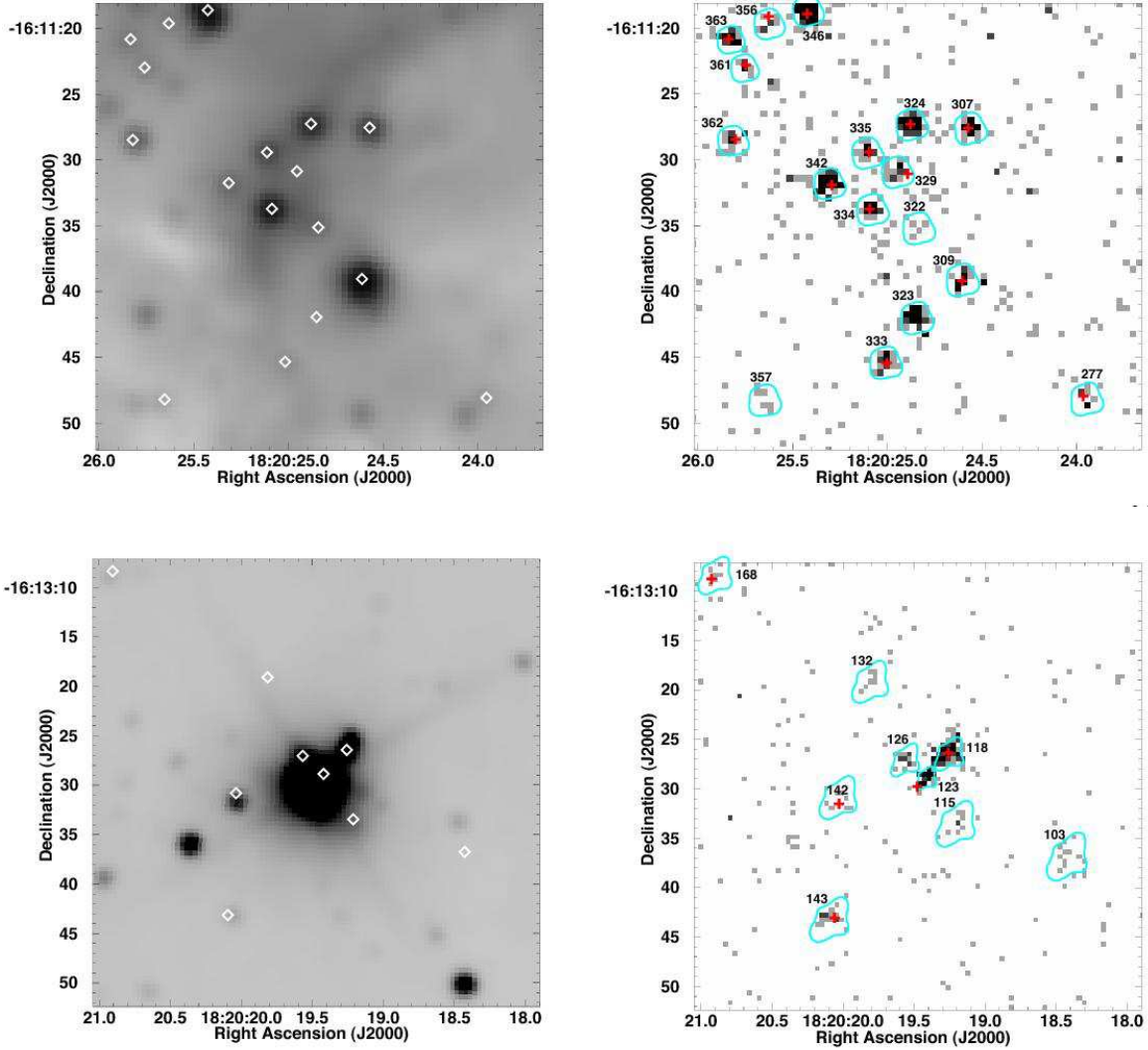


Fig. 10.— M17-UC1 (upper panels, §4.1) and the Kleinmann-Wright Object (lower panels, §4.2) seen in the SIRIUS *K*-band (left) and *Chandra* X-ray (right) images. The X-ray gray scales span 1 to 21 counts (upper right) and 1 to 9 counts (lower right) in  $0.5'' \times 0.5''$  pixels. ACIS sources are marked by diamonds (left) and sequence numbers (right); source extraction regions matching the *Chandra* Point Spread Function are shown in blue. SIRIUS counterparts (+) range from 9 to 14 mag (upper left) and from 7.5 to 15.5 mag (lower left) in *K*. The radio arc of ionized gas associated with M17-UC1 can be faintly seen in the *K*-band image (upper left). ACIS #309 matches the brightest IR component of IRS 5S.

half of the estimated total absorption through Peak 3 (Hobson et al. 1993), consistent with the star lying at the center of the core. The second ACIS source, #244, shows flare-like variability (Figure 3) and more typical properties ( $\log L_{h,c} \sim 31.1$  ergs s<sup>-1</sup>,  $\log N_H \sim 22.2$  cm<sup>-2</sup>,  $K \sim 12$  mag counterpart), suggestive of a young star lying in front of the star forming cores though still inside the M17 giant molecular cloud.

#### 4.2. The Kleinman-Wright Object and its cluster

The lower panels of Figure 10 show the deep  $K$  and *Chandra* images around the IR-luminous star known as the Kleinmann-Wright Object (KWO) or M17-IRS1 (Kleinmann & Wright 1973). IR study reveals a photosphere with  $T_{eff} = 25,000$  K and  $L_{bol} = 5 \times 10^3 L_\odot$  with strong variable hydrogen emission lines (Chini et al. 2004a). It is modeled as a Herbig Be star of spectral type B0V lying inside a dusty envelope with  $M \sim 10 M_\odot$ ,  $r \sim 0.1$  pc, and  $N_H \sim 2 \times 10^{22}$  cm<sup>-2</sup>. It may be the most heavily absorbed and youngest Herbig Be star known, with a Class I protostellar IR spectral energy distribution. Chini et al. resolve a nearby bright NIR source (KWO component 2) lying 1.2'' northwest of the Herbig Be star (KWO component 1). Chini et al. further find a concentrated cluster of about 150 heavily reddened  $JHK$  stars within 0.7 pc (70'') of the KWO.

ACIS source #123, with 31 counts, lies 1.2'' northwest of SIRIUS source 15128; SIRIUS does not resolve the two components described by Chini et al. (2004a), although the SIRIUS J-band image appears elongated to the northwest, in the direction of the ACIS source. Comparing the SIRIUS and ACIS positions to components 1 and 2 of the KWO, based on positions obtained by Chini et al. in the  $i$ -band with the ESO NTT telescope, it appears that the SIRIUS source closely matches KWO component 1 (the Herbig Be star, which is brighter in the NIR), while ACIS #123 closely matches KWO component 2. The Chini et al. positions are systematically offset from the ACIS position and the SIRIUS position (after registration to ACIS/2MASS) by  $\sim 1''$  to the southwest. The KWO Herbig Be star is not detected in this *Chandra* observation. Chini et al. (2004a) report that component 2 ( $\Leftrightarrow$  ACIS #123) is probably a member of the KWO cluster. It exhibits  $\log L_{h,c} \sim 31.0$  ergs s<sup>-1</sup> and  $\log N_H \sim 22.5$  cm<sup>-2</sup> equivalent to  $A_V \sim 20$  mag. The situation resembles that of the Becklin-Neugebauer Object in the OMC-1 where a previously unknown lower-mass companion greatly outshines the young B star in X-rays (Grosso et al. 2005).

A dozen other ACIS sources are present within 30'' of the KWO, a higher density than generally seen in the M17-SW cloud though less rich than seen around IRS 5/UC 1 (§4.1). Most of these sources have  $11 < K < 15$  mag counterparts consistent with intermediate-mass stars in the embedded cluster. As with UC1, an upcoming deeper *Chandra* observation should detect more members of the cluster around the KWO and perhaps the Herbig Be star itself.

#### 4.3. The M17-North cloud

The M17-North cloud cores are dusty molecular concentrations extending over 2' at a location around 10' north of the bright M17 HII region (Wilson et al. 2003). Star formation here is probably occurring without triggering by the HII region. It has five embedded IR sources; radio and ionized line emission suggest that IRS 3 is a late-O star behind the cloud core (Klein et al. 1999). IRS 1 and 3 are off the ACIS field; IRS 2 is at the field edge; IRS 4 and 5 are not detected in the *Chandra* image. However, the ACIS image (Figure 2) and the smoothed map of obscured ACIS sources (Figure 7, right panel) show a density enhancement of a dozen absorbed sources. For example, source #618 lying 10'' from M17-North IRS 4 has  $\log L_h \sim 30.8$  ergs s<sup>-1</sup>

and  $\log N_H \sim 22.5 \text{ cm}^{-2}$  without any known counterpart. Two sources (#660 and 665) lie  $6''$  from each other, again without  $K$ -band counterparts.

Assuming a standard XLF (§3.2, Figure 9), the presence of this group of X-ray luminous stars implies that dozens or hundreds of lower mass stars are present. As with the IRS 5/UC1 and KWO clusters, the population of the clusters cannot be reliably discerned from the present shallow X-ray exposure. However, we note that the (probably untriggered) M17-North group appears to be spread over a larger region ( $\sim 2'$  or 1 pc) than the (probably triggered) clusters in the M17-SW cloud.

#### 4.4. Protostar candidates

*Chandra* studies of nearby low-mass star forming regions (such as the Ophiuchus, Taurus, and Serpens clouds) have established that Class I protostars are X-ray emitters with typical luminosities of  $\sim 10^{30} \text{ ergs s}^{-1}$ , flaring light curves, and hard spectra (e.g. Imanishi et al. 2001; Getman et al. 2005a; Preibisch 2004). The case for X-ray emission from Class 0 sources is problematic (Tsujimoto et al. 2005; Getman et al. 2006b). Systematic studies of X-ray protostars in MSFRs, however, have not yet emerged.

From the *JHK* study of Jiang et al. (2002), 157 candidate Class I protostars were reliably identified from strong  $K$ -band photometric excesses. About half lie in the North Bar and South Bar in the HII region, while the other half are widely distributed across their field. Others can be identified by MIR excesses in the GLIMPSE survey.

Table 7 lists the 64 *Chandra* sources associated with protostellar candidates satisfying one or more of the following criteria:

1. Strong  $K$ -band excess in the  $(J - H)$  vs.  $(H - K)$  diagram beyond the locus of reddened Class II T Tauri stars (Figure 5).
2. Excess in the shortest wavelength band of the *Spitzer* IRAC detector. Observations of Taurus-Auriga young stars with reliable classifications show that the color criterion  $K - [3.6] > 1.5$  mag isolates Class 0-I protostellar systems from Class II-III T Tauri systems (Hartmann et al. 2005).
3. Excess in the second IRAC band with  $[3.6] - [4.5] > 0.7$  mag also separates protostars from T Tauri stars (Hartmann et al. 2005).

Uncertainties on the  $K - [3.6]$  and  $[3.6] - [4.5]$  colors were calculated, and only sources exceeding the stated color thresholds by more than 1 standard deviation are reported. X-ray luminosities in the hard band are reproduced from Table 3 when available; for the fainter sources, we approximate  $\log L_h \sim 29 \text{ ergs s}^{-1}$ , based on the ratio between counts and  $L_h$  for heavily absorbed brighter stars in Table 3. The luminosities range up to  $10^{31.0} \text{ ergs s}^{-1}$ , similar to the distribution of luminosities of Class I sources in the  $\rho$  Ophiuchi cloud (Imanishi et al. 2001).

Only 13 out of 157 Class I candidates identified by  $K$ -band excess (criterion 1 above) are detected. The paucity of extreme  $K$ -band excess sources can also be seen in the NIR color-color diagram discussed in §2.4.2 (Figure 5). The median  $K$  magnitude ( $\sim 13.5$ ) for the 13 X-ray detected sources is 1 magnitude brighter than the median for the 157 Class I NIR candidates, suggesting that, at the sensitivity limits of our observation, only the higher-mass end of the protostar XLF is detected. An upcoming longer *Chandra* observation should detect lower-mass Class I candidates.

An additional 51 Class I candidates in Table 7 identified by colors from longer wavebands (criteria 2 and 3 above), more sensitive to circumstellar disks, are detected. Many of these are highly obscured; half have  $E_{median} > 3$  keV (corresponding to  $A_V \gtrsim 15$  mag). These 51 sources (and perhaps some of the  $\sim 80$  X-ray sources without counterparts described in §2.4.1) represent a significant population of Class I candidates that were not previously available from NIR studies.

Table 7. Photometrically selected X-ray emitting candidate protostars

Seq	CXOU	K (mag)	$\log L_h$ ( $\text{erg s}^{-1}$ )	$\log N_H$ ( $\text{cm}^{-2}$ )	$E_{median}$ (keV)	Photometric Criteria		
						JH,HK	K-[3.6]	[3.6]-[4.5]
(1)	(2)	(3)	(4)	(5)	(6)	(7)	(8)	(9)
7 <sup>a</sup>	182000.65–161112.0	10.88	30.40	22.0	2.0	...	✓	...
21 <sup>a</sup>	182006.33–160453.7	12.52	29:	...	3.3	...	✓	...
26	182008.21–161040.9	13.72	30.33	22.9	2.8	...	✓	...
30 <sup>a</sup>	182008.44–161409.6	11.62	30.71	21.8	1.9	...	✓	...
47	182011.77–160512.2	14.35	29:	...	2.3	...	✓	...
51 <sup>a</sup>	182012.31–160447.7	10.35	30.27	22.3	2.3	...	✓	...
53	182012.44–160610.0	15.73	29:	...	1.1	✓	...	...
57 <sup>a</sup>	182012.96–161308.4	12.46	29:	...	2.0	...	✓	...
58	182013.09–161238.1	...	29:	...	3.4	...	...	✓
60	182013.48–160912.2	14.45	29:	...	1.8	...	✓	...
74	182015.80–161033.2	14.99	29:	...	2.3	...	✓	...
81	182016.54–161003.0	13.83	30.99	23.1	4.1	...	✓	...
94 <sup>a</sup>	182017.82–160453.4	13.67	31.11	22.3	3.3	...	✓	...
95	182017.82–161401.2	13.75	30.79	22.8	3.7	...	✓	...
105 <sup>a</sup>	182018.44–161419.0	12.22	30.52	22.6	2.0	...	✓	...
106	182018.51–161421.4	12.76	30.38	22.2	2.6	...	✓	...
108	182018.65–160607.8	14.07	29:	...	4.1	...	✓	...
109	182018.83–161424.8	...	30.45	22.8	3.6	...	...	✓
113 <sup>a</sup>	182019.06–160629.6	12.96	30.84	22.9	3.1	...	✓	...
117	182019.24–160800.3	13.01	30.44	22.5	2.7	...	✓	✓
128	182019.60–161038.8	11.92	30.45	23.2	4.8	✓	...	...
137 <sup>a</sup>	182019.95–160805.2	12.44	29:	...	3.1	...	✓	...
156	182020.53–160456.3	14.15	30.84	22.6	3.1	...	✓	...
179 <sup>a</sup>	182021.25–160944.3	12.45	29:	...	2.5	...	✓	...
200 <sup>a</sup>	182021.79–161042.0	12.81	30.72	22.6	2.6	...	✓	...
201 <sup>a</sup>	182021.82–161123.6	11.36	29:	...	4.4	...	✓	...
207	182021.97–161100.6	13.31	29:	...	3.1	✓	...	...
209	182022.01–161024.8	14.06	29.99	22.3	2.0	✓	...	...
221	182022.40–161403.9	13.29	29:	...	3.2	...	✓	...
234	182022.70–160951.5	13.88	30.36	22.6	2.7	✓	...	...
235	182022.70–161613.8	14.90	29:	...	3.5	...	✓	...
304	182024.51–160644.3	15.06	30.56	22.7	2.7	...	✓	...
305 <sup>a</sup>	182024.54–160737.6	12.00	30.18	22.2	3.7	...	✓	...
324 <sup>ab</sup>	182024.87–161127.5	10.75	30.74	22.4	2.7	✓	...	...
328	182024.93–160459.5	14.38	29:	...	3.2	...	✓	...
363 <sup>b</sup>	182025.82–161121.0	13.61	30.32	22.2	2.1	✓	...	...
372	182025.95–160938.2	13.63	29:	...	2.5	...	✓	...
380	182026.12–160455.9	14.24	31.07	22.8	3.6	...	✓	...
438 <sup>a</sup>	182027.62–161043.3	12.25	29:	...	3.8	...	✓	...
472	182028.28–161130.5	11.08	30.52	22.4	2.6	✓	...	...

The two sources from Table 6 identified as Class I (#324 and #650) are two of the  $K$ -band excess sources in Table 7. An additional 21 sources in Table 7 also appear in Table 6. Assuming that the protostar criteria defined above supersede the estimated disk/envelope evolutionary classes in Table 6, these 23 sources (marked by note  $a$  in Table 7) define a new sample of X-ray selected intermediate- and high-mass protostars; none are known OB stars. These stars especially warrant further study.

Nielbock et al. (2001) report an independent survey for high-mass Class I stars in M17 based on ground-based 10  $\mu\text{m}$  and 20  $\mu\text{m}$  imaging. Of their 22 luminous IR sources, we detect the 9 listed in Table 8 (nominally

Table 7—Continued

Seq	CXOU	K (mag)	$\log L_h$ ( $\text{erg s}^{-1}$ )	$\log N_H$ ( $\text{cm}^{-2}$ )	$E_{median}$ (keV)	Photometric Criteria		
						JH,HK	K-[3.6]	[3.6]-[4.5]
(1)	(2)	(3)	(4)	(5)	(6)	(7)	(8)	(9)
498	182028.95–160957.7	13.26	30.43	22.4	2.2	...	✓	...
500	182029.01–160831.5	14.52	29:	...	2.9	✓	...	...
535	182029.80–161125.4	12.46	29.72	22.2	1.8	...	✓	...
562	182030.18–161216.5	14.15	29.86	22.4	2.3	✓	...	...
595 <sup>a</sup>	182030.88–160905.1	11.47	30.55	21.9	2.1	...	✓	...
596	182030.90–160954.7	12.69	29:	...	2.3	...	✓	...
607 <sup>a</sup>	182031.09–161126.1	12.42	30.43	22.0	2.6	...	✓	...
610	182031.23–160218.2	12.71	30.83	22.7	3.1	...	✓	...
637	182031.70–160612.1	14.64	29:	...	4.3	...	✓	...
643	182031.79–160349.3	14.26	29:	...	2.9	...	✓	...
650 <sup>a</sup>	182031.89–161616.5	9.57	30.07	20.6	1.7	✓	✓	...
652	182031.94–160239.7	13.13	31.30	22.8	3.8	...	✓	...
654 <sup>a</sup>	182031.97–160925.1	11.26	30.50	21.9	2.6	...	✓	...
668 <sup>a</sup>	182032.47–161047.2	13.54	29:	...	4.4	...	✓	...
677 <sup>a</sup>	182033.17–160746.6	12.10	29:	...	2.7	...	✓	...
679	182033.32–161050.9	13.63	29:	...	3.1	...	✓	...
682 <sup>a</sup>	182033.42–161042.7	11.79	29:	...	3.4	...	✓	...
709	182034.79–161053.8	11.66	30.47	21.8	1.9	...	✓	...
718	182035.34–161325.4	13.58	29:	...	2.3	✓	...	...
757 <sup>a</sup>	182037.62–160332.6	12.00	30.95	22.3	2.7	...	✓	✓
762	182037.99–160925.8	12.78	30.62	21.8	2.0	...	✓	...
789	182040.93–161111.7	15.67	29:	...	1.3	✓	...	...
782	182039.62–161146.5	12.41	30.70	22.8	3.1	...	✓	...
784	182039.83–160500.1	15.41	30.46	22.8	3.3	...	✓	...

Note. — **Columns 1–2:** Source identification from Table 1. **Column 3:**  $K$ -band magnitudes from Jiang et al. (2002). **Columns 4–5:** X-ray spectroscopic parameters from Table 3, when available. For faint sources, a value of  $\log L_h \sim 29 \text{ ergs s}^{-1}$  is assumed (see text). **Column 6:** Median X-ray energy from Table 1. **Columns 7–9:** Selection criteria from §4.4.

<sup>a</sup>Source is also classified as an intermediate- or high-mass star (Table 6).

<sup>b</sup>These protostars lie in the M17-SW IRS 5 cluster around the ultracompact HII region UC1.

including the tentative *Chandra* detection of IRS 5N). The X-ray non-detections are not systematically fainter in the IR or more obscured. Four of the sources in Table 8 are cataloged OB stars (ACIS #186, 233, 296, and 488), but the remaining five stars (ACIS #128, 239, 309, 322, and 398) should be added to the 23 described above as X-ray detected intermediate- and high-mass protostar candidates. Only the first of those, #128, also appears in our list of candidate protostars (Table 7). However it is not identified (in Table 6) as massive based on its NIR colors; it is a distinct outlier in the *JHK* color-color diagram (Figure 5) and is a hard X-ray source. Source #239, has no NIR counterpart; #309 and #398 appear in Table 6 but not in Table 7. Source #322 ( $\Leftrightarrow$  IRS 5S; §4.1), has a SIRIUS counterpart but unreliable *JHK* photometry.

All the sources in Table 8 have X-ray luminosities around  $10^{30}$  ergs  $s^{-1}$ . This is typical of late-O and early-B stars without strong radiatively accelerated winds (Stelzer et al. 2005). In some cases, the X-ray emission probably arises from unresolved low mass companions. None of these 9 stars are powerful wind sources like the central O4+O4 binary (§5.2). A useful comparison can be made to the cluster of proto-B stars in the Becklin-Neugebauer region of the Orion Molecular Cloud 1 (OMC-1). In OMC-1, one star (Source n) has  $\log L_h \gtrsim 30$  ergs  $s^{-1}$  and three others are detected around  $\log L_h \sim 29$  ergs  $s^{-1}$  (Grosso et al. 2005). In M17, there are a dozen stars similar to Source n. These stars are not confined to the well-studied M17-UC1 and KWO clusters; indeed, several appear on the western side of the image away from the M17 HII region. This supports the claim that star formation in the M17 cloud is widely distributed, as indicated by the widespread distribution of *JHK* protostars seen by Jiang et al. (2002).

Finally, three interesting high-mass sources merit comment. Source #488 ( $\Leftrightarrow$  IRS 15) has recently been described by Chini et al. (2006) as a newly-formed 26  $M_\odot$  star (spectral type B0.5V) that has stopped accreting but is still surrounded by a huge remnant disk. Its X-ray spectral properties are similar to other early-B stars in M17. No X-ray source is found associated with M17-SO1 (M17 silhouette object 1), an intermediate- or high-mass star with a dusty envelope and bipolar reflection nebula (Chini et al. 2004b; Sako et al. 2005a). CEN 92, a reddened, massive binary system with  $L_{IR} > 10^5 L_\odot$  and a circumstellar IR-bright shell (Chini et al. 2005), is also undetected in X-rays. Chini et al. note that CEN 92 and IRS 5N (ionizing M17-UC1) might be similar objects; both are emission-line stars and IRS 5N might be binary.

#### 4.5. Distributed star formation across the molecular cloud

A number of heavily obscured X-ray stars lie in other dense molecular regions of M17-SW. Vallée & Bastien (1996) identify six peaks in dust and molecular emission maps as dense cores with sizes  $10 - 30''$  ( $0.1 - 0.3$  pc), masses  $70 - 470 M_\odot$ , densities  $1 - 8 \times 10^5 \text{ cm}^{-3}$  and absorbing columns of  $1.5 - 3 \times 10^{23} \text{ cm}^{-2}$ . ACIS sources #236 in Peak 1, #97 in Peak 2, #177 in Peak 4, and #275 in Peak 5 all have intrinsic X-ray luminosities around  $\log L_{h,c} \sim 30.5 - 31$  ergs  $s^{-1}$  and absorptions around  $\log N_H \sim 22.3 - 22.6 \text{ cm}^{-2}$ . The luminous source #239  $\Leftrightarrow$  Anon 1 in Peak 3 was discussed earlier in §4.1 and Table 8. None of these molecular gas concentrations appears to have produced rich stellar clusters, but the high X-ray luminosities of the detected stars implies that more sources with lower luminosities are present.

We can examine the X-ray source list for heavily obscured stars that have not been studied at other wavelengths. Due to the short exposure, only the stars with  $\log L_h \gtrsim 30.5$  ergs  $s^{-1}$  are sufficiently bright to permit quantitative estimation of high levels of obscuration. Six ACIS sources have spectral fits with  $\log N_H \geq 23.3 \text{ cm}^{-2}$  equivalent to  $A_V \gtrsim 100$  mag: #37, 135, 239, 246, 255, and 706. Two of these (#239 and 246) reside in the M17-UC1 cluster while the others are not in known molecular cores.

Altogether, we support the evidence of Jiang et al. (2002) and others that star formation is widely

Table 8. X-ray emitting high-mass Class I sources from Nielbock et al. (2001)

Seq	CXOU	Name	K (mag)	$\alpha_{K,N}$	$L_{IR}$ ( $L_{\odot}$ )	SpTy	$\log L_h$ ( $\text{erg s}^{-1}$ )	$\log N_H$ ( $\text{cm}^{-2}$ )
(1)	(2)	(3)	(4)	(5)	(6)	(7)	(8)	(9)
128	182019.60–161038.8	B 353	11.92	2.1	75	...	30.45	23.2
186	182021.43–160939.1	CEN 35	10.42	0.8	<140	B3	30.42	22.1
233	182022.69–160833.9	CEN 16 <sup>a</sup>	9.10	1.3	<275	B0:	30.69	21.7
239	182022.87–161148.5	Anon 1	...	3.3	590	...	30.78	23.5
296	182024.39–160843.3	CEN 31 <sup>a</sup>	9.40	2.3	910	O9.5	29.58	21.6
309	182024.60–161139.2	IRS 5S	9.34	2.5	1900	...	30.50	22.8
322	182024.83–161135.3	IRS 5N <sup>b</sup>	...	4.2	4775	...	29:	...
398	182026.62–161136.5	IRS 10	10.56	1.5	55	...	29.99	22.5
488	182028.65–161211.6	IRS 15 <sup>a</sup>	10.08	3.0	1405	B0.5	30.78	22.2

Note. — **Columns 1–2:** Source identification from Table 1. **Column 3:** Counterpart identification from Nielbock et al. (2001). **Column 4:** *K*-band magnitudes from Jiang et al. (2002). **Column 5:** Spectral index from Nielbock et al. (2001). **Column 6:** Infrared luminosity from Nielbock et al. (2001). **Column 7:** Spectral type. **Columns 8–9:** X-ray spectroscopic parameters from Table 3.

<sup>a</sup>These stars are surrounded by resolved infrared-bright dusty disks (Chini et al. 2005, 2006).

<sup>b</sup>Source #322 is tentative (§4.1) and its luminosity is assumed.

distributed across the cloud in addition to concentrations around M17-UC1, the KWO, and M17-North. This implies either that star formation triggered by the passage of the ionization front of the large M17 HII region does not always produce concentrated clusters and/or that much of the star formation in the cloud was not triggered.

## 5. X-rays from massive stars

Individual O stars have long been known to emit soft X-rays at levels  $L_x \propto 10^{-7} L_{bol} \sim 10^{31-33}$  ergs  $s^{-1}$  (Chlebowski et al. 1989; Berghoefer et al. 1997; Sana et al. 2006), arising from a myriad of weak shocks within their radiatively accelerated winds (Lucy & White 1980; Pallavicini et al. 1981; Owocki & Cohen 1999). While this soft ( $kT \sim 0.5$  keV), slowly varying X-ray component dominated early studies of O stars, recent studies reveal discrepancies with X-ray line widths, inferred densities, and temperatures (Waldron & Cassinelli 2001). In particular, a moderately hard component ( $kT \sim 2 - 3$  keV) may be present which is sometimes rotationally modulated and/or shows rapid variability (Feigelson et al. 2002; Schulz et al. 2003; Stelzer et al. 2005; Schulz et al. 2006). While not fully understood, this component has been attributed to a large-scale magnetically confined (or at least channeled) wind shock that diverts radial outflow into an equatorial disk, causing an X-ray emitting shock (Babel & Montmerle 1997; Gagné et al. 2005). A luminous hard X-ray component, sometimes reaching  $L_h \sim 10^{33}$  ergs  $s^{-1}$  and  $kT > 10$  keV, can be produced by wind-wind collisions in close massive binaries, particularly if one component is a Wolf-Rayet star (e.g. Skinner et al. 2002; Pollock et al. 2005; Skinner et al. 2006), or possibly by a non-thermal inverse Compton process (Chen & White 1991). An emerging class of late-O/early-B emission line stars known as “ $\gamma$  Cas analogs” (Smith & Balona 2006; Rakowski et al. 2006) show very hard X-ray spectra ( $kT > 8$  keV) and variable X-ray lightcurves, perhaps due to some combination of winds, magnetic fields, and disk processes (Smith et al. 2004). Wind-generated X-rays become insignificant in stars cooler than early-B types, but these systems are sometimes detected in X-rays due to lower mass pre-main sequence companions (e.g. Stelzer et al. 2005; Sana et al. 2006) or perhaps due to their own intrinsic emission (e.g. Stelzer et al. 2006).

M17 provides an excellent laboratory for study of these OB wind-generated X-rays due to the large population of coeval and codistant massive stars in a single field. The main limitation is that we cannot uniformly measure their soft X-ray components due to heavy absorption towards some systems.

Table 9 gives the X-ray properties of all published O and early B stars in the region (from TFM03, with IRS 15 added from Chini et al. 2006)<sup>9</sup>. The stars are listed in order of decreasing mass; see the table notes for descriptions of the tabulated quantities. While all of the O stars in Table 9 are detected with *Chandra*, only 19 of the 34 B0–B3 stars are detected.

Figure 11 shows a close-up view of the cluster center where many of the OB stars are concentrated. Figure 12 shows the X-ray spectra of the components of the O4+O4 binary and four other OB stars, illustrating the diversity of plasma properties. Note that all but one of these spectra show very hard thermal plasma components with  $kT > 4$  keV. As mentioned above, such hard X-ray emission is most commonly seen in colliding wind binaries; a famous example is  $\eta$  Carinae (Corcoran et al. 2004).

---

<sup>9</sup> The two O stars listed in TFM03 as *Chandra* non-detections (CEN 102 and CEN 34) were determined by Hanson, Howarth, & Conti (1997) to be background red giants based on their NIR brightness and the presence of CO bandhead absorption in their IR spectra. The B stars CEN 95 and CEN 33, also not detected in X-rays, were similarly identified by Hanson et al. to be background sources. These four sources are omitted from Table 9.

Table 9. X-ray properties of cataloged OB stars in NGC 6618

Optical Properties					X-ray Properties						
Name	SpTy	SIRIUS	K	$\log L_{bol}$	Seq	$\Delta\phi$	NetCts	$\log N_H$	kT	$\log L_h$	$\log L_{t,c}$
(1)	(2)	(3)	(mag)	( $L_{\odot}$ )	#	( $''$ )	(8)	( $\text{cm}^{-2}$ )	(keV)	( $\text{erg s}^{-1}$ )	( $\text{erg s}^{-1}$ )
(1)	(2)	(3)	(4)	(5)	(6)	(7)	(8)	(9)	(10)	(11)	(12)
CEN 43	O3-O4	10396	8.18	5.8	675	0.2	82	22.1	2.0	31.02	31.53
CEN 1a	O4	...	6.59:	5.7	536	...	1912	22.4	0.9+15	32.37	33.16
CEN 1b	O4	...	6.59:	5.7	543	...	3866	22.3	0.7+10.4	32.78	33.28
CEN 2	O5	10399	7.49	5.5	701	0.1	250	21.2	1.6	31.14	31.69
CEN 37	O3-O6	10398	7.88	5.5	574	0.2	90	22.4	0.6	30.42	32.25
OI 345	O6	14703	9.18	5.3	433	0.0	263	22.0	0.6	30.32	32.06
CEN 18	O7-O8	28446	7.84	5.1	366	0.2	128	21.8	4.4	31.02	31.31
CEN 25	O7-O8	7877	8.94	5.1	593	0.1	16	21.9	0.7	29.53	31.00
OI 352	O8	...	6.82	5.0	732	...	1375	22.2	0.5+4.4	32.00	32.95
CEN 16	O9-B2	28651	9.10	4.8	233	0.4	73	21.7	3.5	30.69	31.01
CEN 61	O9-B2	7833	9.23	4.8	567	0.1	44	22.3	0.6	30.05	31.72
CEN 3	O9	10401	7.59	4.8	720	0.2	108	21.6	0.6	29.72	31.34
OI 174	O9	...	7.80	4.8	12	0.5	121	22.1	0.5	30.10	32.04
CEN 31	O9.5	27457	9.40	4.7	296	0.1	10	22.0	2:	28.81	30.31
CEN 92	B0	14714	9.10	4.5	...	...	...	...	...	<29.0	<29.5
CEN 28	B0	8849	11.40	4.5	647	0.1	4	21:	2:	28.5:	28.8:
OI 582	B0	...	...	4.5	875	...	19	20:	1.7	29.69	30.20
IRS 15	B0.5	5988	10.08	4.3	488	0.0	71	22.2	2.2	30.78	31.30
CEN 57	B1	14554	9.58	4.0	347	0.2	117	22.1	2.5	31.00	31.44
CEN 101	B1	9090	11.39	4.0	496	0.0	111	22.0	1.8	30.76	31.32
CEN 97	B1	13963	10.78	4.0	507	0.0	134	22.2	2.9	31.11	31.52
CEN 100	B1	17147	10.85	4.0	608	0.0	223	22.1	3.9	31.41	31.75
CEN 45	B1	4442	10.81	4.0	726	0.2	11	21.8	2:	29.71	30.19
CEN 51	Early B	14187	9.79	3.5	...	...	...	...	...	<29.0	<29.5
CEN 24	B2	15126	8.42	3.5	...	...	...	...	...	<29.0	<29.5
CEN 49	B2	14649	9.72	3.5	...	...	...	...	...	<29.0	<29.5
CEN 48	B2	13124	10.98	3.5	...	...	...	...	...	<29.0	<29.5
CEN 90	B2	14345	11.51	3.5	406	0.1	79 <sup>e</sup>	22.2	1.8	30.79	31.39
CEN 85	B2	6104	10.62	3.5	466	0.0	538	22.3	4.8	31.86	32.19
CEN 84	B2	6109	11.11	3.5	495	0.2	8	21:	2:	28.8:	29.1:
CEN 96	B2	14492	10.81	3.5	...	...	...	...	...	<29.0	<29.5
CEN 89	B2	7390	11.33	3.5	...	...	...	...	...	<29.0	<29.5
CEN 99	B2	9160	11.58	3.5	638	0.3	88	21.8	2.2	30.67	31.12
CEN 17	B3	12345	12.33	3.2	182	0.2	12 <sup>e</sup>	21.9	0.7	29.06	30.47
CEN 93	B3	14349	9.59	3.2	...	...	...	...	...	<29.0	<29.5
CEN 35	B3	14179	10.42	3.2	186	0.1	30	22.1	3.0	30.42	30.81
CEN 75	B3	23809	11.99	3.2	...	...	...	...	...	<29.0	<29.5
CEN 94	B3	12342	11.47	3.2	...	...	...	...	...	<29.0	<29.5
CEN 91	B3	14141	11.25	3.2	312	0.1	86	22.1	3.7	30.94	31.29
CEN 83	B3	12337	11.28	3.2	350	0.0	309 <sup>f</sup>	22.1	5.0	31.55	31.85
CEN 14	B3	14893	12.16	3.2	...	...	...	...	...	<29.0	<29.5
CEN 26	B3	13500	10.53	3.2	376	0.1	78	22.3	1.9	30.81	31.38
CEN 74	B3	27036	11.77	3.2	399	0.2	6	21.:	2:	28.7:	29.0:
CEN 46	B3	7804	9.47	3.2	450	0.8	6	21.:	2:	28.7:	29.0:
CEN 47	B3	9089	10.80	3.2	...	...	...	...	...	<29.0	<29.5
CEN 65	B3	3592	11.50	3.2	...	...	...	...	...	<29.0	<29.5
CEN 27	B3	7284	9.90	3.2	...	...	...	...	...	<29.0	<29.5
CEN 44	B3	1183	13.86	3.2	...	...	...	...	...	<29.0	<29.5

Note. — **Column 1:** This list is obtained from Appendix A of TFM03 (with IRS 15 added) which gives optical cross-identifications, positions and spectral types. The stars are listed first in order of decreasing mass, and then by right ascension. CEN = Chini, Elsaesser, & Neckel (1980), OI = Ogura & Ishida (1976). The CEN 1 O4+O4 binary (§5.2) is also known as Kleinmann’s Anonymous Star (Kleinmann 1973) and CEN 3 is BD -16°4818. The B3 stars CEN 50, CEN 58, CEN 81, and CEN 82 are omitted because accurate positions are not available. The stars CEN 33  $\Leftrightarrow$  B 324, CEN 34  $\Leftrightarrow$  B 358, CEN 95  $\Leftrightarrow$  B 266, and CEN 102  $\Leftrightarrow$  B 305 are omitted because they are likely to be background red giants (Hanson, Howarth, & Conti 1997); none of these sources was detected in X-rays.

**Column 2:** Spectral types are from Hanson, Howarth, & Conti (1997), Chini, Elsaesser, & Neckel (1980), and SIMBAD.

**Columns 3–4:** Source numbers and K-band magnitudes are from Jiang et al. (2002).

**Column 5:** Bolometric luminosities are estimated from calibrations of  $L_{bol}$  with spectral type, Martins et al. (2005) for O3–O9.5 stars and de Jager & Nieuwenhuijzen (1987) for B stars. No use is made of available photometry.

**Column 6:** *Chandra* source number, from Table 1.

**Column 7:** Offset (in arcseconds) between the *Chandra* and *SIRIUS* sources. Both fields are aligned to the 2MASS astrometric frame.

**Columns 8–12:** X-ray properties from Table 3: extracted counts after background subtraction; column density and plasma energy from fits to the ACIS spectra (: in  $\log N_H$  values are approximated from median energy (Feigelson et al. 2005); : in kT are assumed); observed hard band luminosity (2–8 keV); inferred total band luminosity corrected for absorption (0.5–8 keV). Upper limits to luminosities are matched to the fainter sources in Table 3.

<sup>a</sup>We adopt the nomenclature CEN 1a and CEN 1b for the O4+O4 binary components of Kleinmann’s Anonymous Star (§5.2) which are resolved by *Chandra*. These sources do not appear in the *SIRIUS* catalog due to crowding and/or saturation. The K-band magnitudes shown are estimated by splitting the  $K = 5.84$  measurement from Chini & Wargau (1998) into two equal halves.

<sup>b</sup>This star is saturated in the *SIRIUS* data and does not appear in the catalog. We use here position and photometry from the 2MASS catalog: 2MASS 18203586–1615431 with  $J=7.97$ ,  $H=7.21$  and  $K=6.82$ .

<sup>c</sup>This star is outside the field of view of the *SIRIUS* data. We use here position and photometry from the 2MASS catalog: 2MASS 18200299–1602068 with  $J=8.68$ ,  $H=8.09$ , and  $K=7.80$ .

<sup>d</sup>This star is outside the field of view of the *SIRIUS* data. The available position is too inaccurate to reliably match to 2MASS.

<sup>e</sup>The X-ray emission may be variable.

<sup>f</sup>The X-ray emission is definitely variable; see Figure 3 for light curve.

### 5.1. OB Star Luminosities

The most fundamental question concerning OB X-ray emission for single stars is whether the X-ray production scales with the wind power, which in turn is expected to scale with the bolometric luminosity. Figure 13a compares X-ray and bolometric luminosities for the cataloged M17 OB population. The X-ray

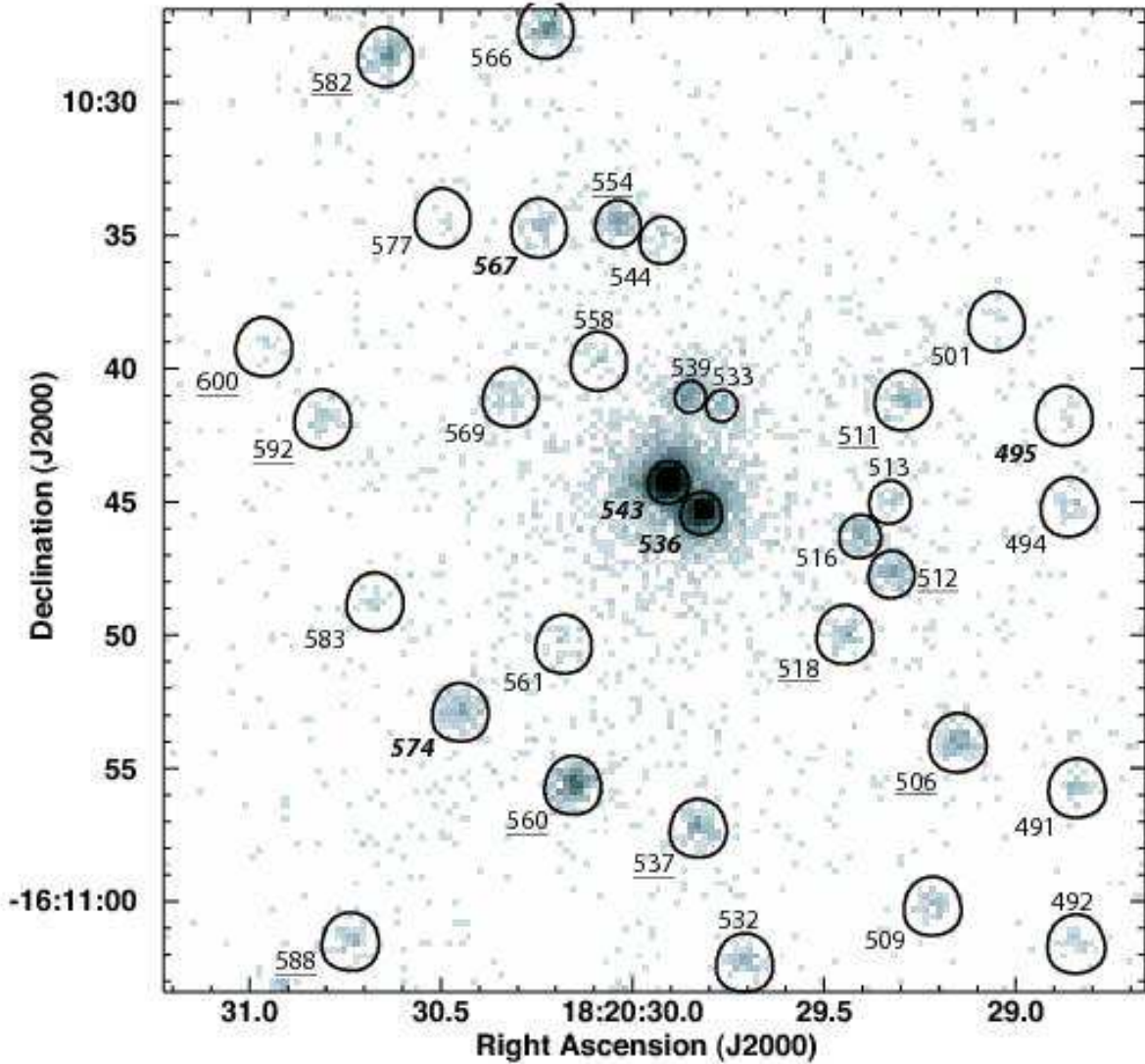


Fig. 11.— ACIS image of the central region of the NGC 6618 cluster with source sequence numbers and extraction regions indicated. This image is shown at high-resolution with  $0.25'' \times 0.25''$  pixels. Sources #536 and #543 (bold-italic) are the two O4 components of Kleinmann’s Anonymous Star (§5.2). Sources #495, 567, and 574 (bold-italic) are also known OB stars (Table 9). Sources with underlined labels are listed in Table 6 as candidate new intermediate- or high-mass stars.

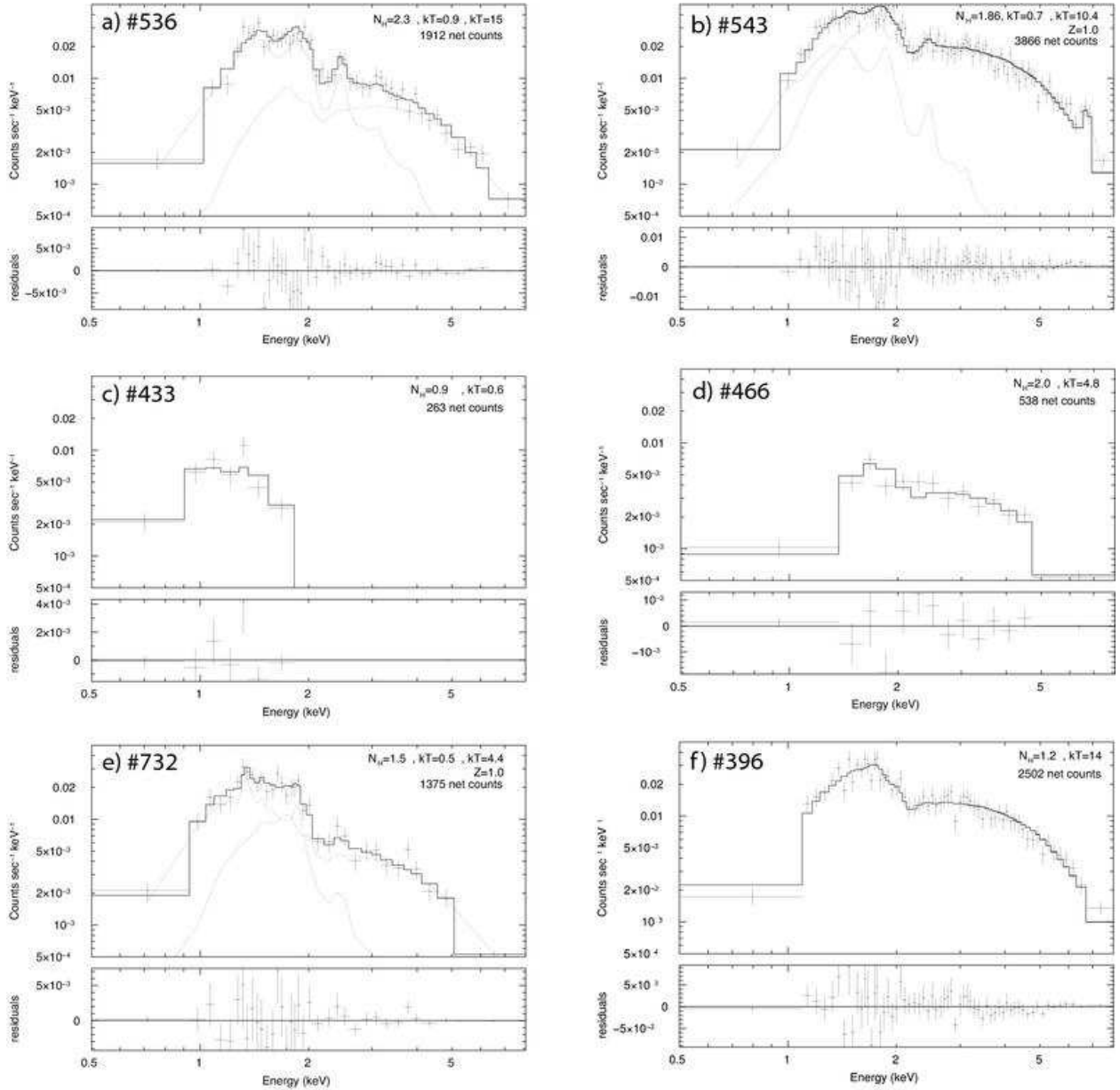


Fig. 12.— Thermal plasma models for the X-ray spectra of selected OB stars in M17. The absorbing column density  $N_H$  is shown in units of  $10^{22} \text{ cm}^{-2}$ ; plasma temperature is shown in units of keV. Elemental abundances were  $Z = 0.3Z_\odot$  unless otherwise specified. Panels a, b, and e are two-temperature models; model components are shown separately as dotted curves. (a,b) Spectral models for the binary components of Kleinmann’s Anonymous Star (#536 and #543, §5.2). In these two-temperature models, both O4 stars show a typical soft plasma; both also show a much harder plasma component most likely caused by colliding winds from an unresolved binary component (e.g. Pollock et al. 2005). (c) A soft spectrum from the O6 star OI 345 (#433). (d) A B2 star (#466) with a hard spectrum; this star lies at the center of NGC 6618 (§3.1). (e) A hard spectrum from the O8 star OI 352 (#732). (f) A hard spectrum from the unidentified luminous source #396 (§5.3).

luminosity shown,  $L_{t,c}$ , is over the full (0.5–8 keV) band, corrected for absorption. We adopt  $L_{bol}$  values here based on calibrations between spectral types and bolometric luminosities for main sequence OB stars (Martins et al. 2005; de Jager & Nieuwenhuijzen 1987). No attempt is made to use available photometry with absorption and bolometric corrections as the available measurements and reddening estimates are incomplete and unreliable.

We used the ASURV survival analysis package (Isobe et al. 1986)<sup>10</sup> to perform statistical tests for correlation between  $L_{t,c}$  and  $L_{bol}$ , with proper statistical treatment (generalized Kendall’s tau correlation test) of the available upper limits. The correlation among M17 sources was very significant (null hypothesis probability  $P < 0.01\%$ ), supporting the long-standing  $L_x \propto 10^{-7} L_{bol}$  relationship (Chlebowski et al. 1989; Berghoefer et al. 1997). Most of the lower luminosity members are undetected; this group would be underrepresented in a plot that did not include X-ray upper limits based on a sample defined at other wavebands.

<sup>10</sup>Available from the Center for Astrostatistics at <http://astrostatistics.psu.edu/statcodes>

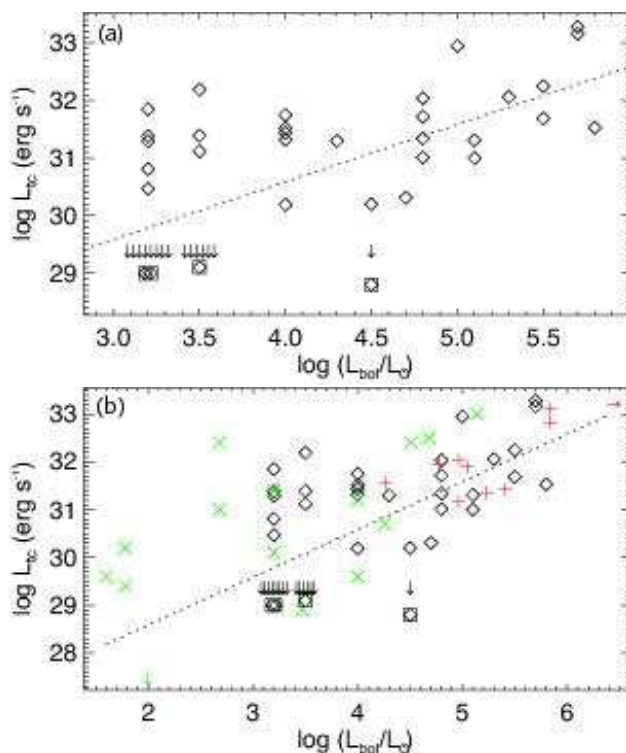


Fig. 13.— Relationship between X-ray and bolometric luminosities for M17 OB stars in Table 9. Arrow tails represent estimated upper/lower limits; overlapping points are artificially displaced horizontally for readability. Boxed points represent estimated values. The dotted line represents the model  $L_{t,c} = 1 \times 10^{-7} L_{bol}$ . (a) Broad-band (0.5–8 keV) X-ray luminosity corrected for absorption vs. bolometric luminosity. (b) M17 OB stars (same symbols as in panel a) shown with Pismis 24 OB stars (red pluses and red arrow) from Wang et al. (2006) and Orion Nebula Cluster OB stars (green  $\times$ 's and green arrow) from the COUP study (Stelzer et al. 2005).

For comparison, Figure 13*b* shows the M17 OB stars in context with the OB stars in the Pismis 24 cluster in NGC 6357 (Wang et al. 2006) and in the Orion Nebula Cluster (Stelzer et al. 2005), with  $L_{bol}$  for these sources estimated from spectral types via the same method used for the M17 sources. The red arrow represents a lower limit for  $L_{bol}$  for the Wolf-Rayet + O7 binary WR93 in NGC 6357 and the green arrow represents an upper limit to the X-ray emission from a COUP B star. The  $L_{t,c}$  value for the Orion source  $\theta^1$  Ori C was replaced by a more accurate value reported by Gagné et al. (2005). This plot demonstrates that the M17 OB stars display a similar correlation between  $L_{t,c}$  and  $L_{bol}$ , with similar scatter, to that seen in the other two populations. As in the COUP sample, more scatter is seen in the M17 B stars than in the O stars; these B stars have emission comparable to lower mass pre-main sequence stars and sometimes that emission may actually come from unresolved low-mass companions rather than from the B stars themselves. Only one of these M17 sources is variable: the B3 star #350 ( $\Leftrightarrow$  CEN 82) shows factor of  $\sim 2$  variations during the 12 hour exposure (Figure 3). The behavior does not resemble the common fast-rise-slow-decay shape seen in low-mass stellar flares, so it is possible that it arises from large-scale shocks in a magnetically channeled wind (e.g. Gagné et al. 2005). Results shown in Figure 13 are consistent with those found for NGC 6231 by Sana et al. (2006).

## 5.2. The central O4+O4 binary

*Chandra* resolves (Figure 11) the two luminous components of Kleinmann’s Anonymous Star (Kleinmann 1973), the binary O4+O4 system with separation  $1.8''$  ( $\sim 3000$  AU projected) and total mass  $M \sim 140 M_{\odot}$  at the top of the stellar IMF of NGC 6618. The spectral types for these stars were originally determined by *UBVRI* photometry (Chini, Elsaesser, & Neckel 1980) using images where the two stars were not resolved, thus the identical spectral types is an assumption. Hanson, Howarth, & Conti (1997) obtained a NIR spectrum for the unresolved pair and deduced an IR spectral type of O3–O4, again with no information on the individual components. Given that these early O stars provide substantial ionization to power the M17 complex and lie near the center of the NGC 6618 cluster, independent spectral types for the two components via improved NIR and visual spectroscopy are clearly needed.

ACIS sources #536 and #543, the X-ray counterparts to the O4 stars, are the brightest and most luminous X-ray stars in the cluster with intrinsic total band (0.5–8 keV) luminosities  $\log L_{t,c} \sim 33.2$  and  $33.3$  ergs  $s^{-1}$ , respectively. We see no enhanced X-ray emission between the two O4 stars, implying that there is not a strong shock between their winds; this result is expected given their large separation. The light curves show that the X-ray emission from each source is constant within  $\sim 10\%$  during the 12 hour exposure.

Two-temperature thermal plasma models were needed to account for each O4 star’s broad X-ray spectrum, and each star shows a strong hard component with emission extending beyond the 8 keV reflectivity limit of the *Chandra* mirrors (Figure 12*a,b*). We recorded twice as many ACIS counts for source #543 as for #536 <sup>11</sup>. In both sources, the hard component contributes substantially to the intrinsic flux. For #543, 96% of the hard-band intrinsic flux comes from the  $kT = 10$  keV plasma; this component contributes 26% of the soft-band and 52% of the full-band flux ( $\log L_{t,c} \sim 33.0$  ergs  $s^{-1}$ ). For #536, 71% of the hard-band

---

<sup>11</sup>Source #543 may suffer slight photon pile-up with  $\sim 0.3$  counts per frame, but a careful analysis of spectra from annular regions in the PSF wings of this source did not yield substantially different spectral fit parameters; although the core might be slightly piled up, there are not enough counts in the wings to yield a measurable change in the fit parameters when core events are excluded.

flux is due to the  $kT = 13$  keV component, while just 10% of the soft-band and 25% of the full-band flux ( $\log L_{t,c} \sim 32.5$  ergs  $s^{-1}$ ) comes from this hard plasma.

Skinner et al. (2002) provide a particularly cogent and helpful review of the possible causes of hard X-ray emission in massive stars. They describe an *XMM-Newton* observation of the Wolf-Rayet star WR 110, which displays the expected soft plasma ( $kT = 0.55$  keV) seen in single massive stars and an additional hard component with a poorly constrained temperature of  $kT > 3$  keV. They assess several models, including magnetically-confined wind shocks, and finally conclude that wind shocks with an unseen binary companion are the most likely cause of the hard component.

Another model mentioned by Skinner et al. (2002) involves non-thermal hard X-ray emission caused by inverse Compton scattering of UV photons from the star off of relativistic charged particles created in the wind shocks (Chen & White 1991). Although the WR 110 data are too poor to constrain this model, we can apply it to the M17 O4 stars. Fitting the fainter O4 star (#536) with a power law instead of a hard thermal component (keeping  $N_H$  and the soft plasma component the same as in the original fit) yields an acceptable fit, only slightly worse than the two-temperature thermal plasma fit, with a power law photon index of  $\Gamma = 1.3$ . Although this power law slope is not well-constrained by these data, it is consistent with the slope of 1.5 predicted by Chen & White (1991). The full-band intrinsic luminosity for this power law component is  $\log L_{t,c} \sim 32.4$  ergs  $s^{-1}$ , three orders of magnitude brighter than the prediction of Chen & White (1991). However, Skinner et al. (2002) note that this luminosity is strongly dependent on the magnetic field strength of the star and its wind temperature and mass loss rate. Thus, inverse Compton scattering could be an alternative explanation to colliding winds for source #536, but extreme physical parameters would be required to generate such a high luminosity.

In contrast, fitting the brighter O4 star (#543) with this soft plasma + power law model yields an unacceptable fit; this source has an Fe line that the power law model cannot reproduce (see Figure 12*b*). This Fe line is strong evidence that the 10 keV plasma in source #543 has a thermal origin, most likely caused by colliding winds between the O4 star and an as yet undiscovered binary companion. Since the Fe line in source #543 argues that its hard component is thermal, it is reasonable to assume that the hard component seen in the other O4 star (source #536) is also thermal; it is probably just too faint for its Fe line to be seen in this observation.

This implies that each O4 component of Kleinmann’s Anonymous Star may itself be a massive binary and that the system actually consists of at least 4 massive stars. It is remarkable that these two X-ray sources show such similar and yet highly unusual spectra; thermal plasmas this hot are not seen even in Wolf-Rayet colliding-wind binaries or in  $\eta$  Carinae. Only the “ $\gamma$  Cas analogs” (Smith & Balona 2006; Rakowski et al. 2006; Smith et al. 2004) show such hard X-ray spectra, yet M17’s O4 stars do not show the variable lightcurves typical of these objects. Some complex process, likely involving both colliding winds in close binaries and unusual magnetic field properties, may be necessary to explain M17’s O4 stars. Again, visual and NIR spectroscopy of these two stars is highly warranted.

The NGC 6618 O4 stars and later OB stars (Figure 12) thus give new examples of the extremely hot plasmas that can be generated in powerful O star winds. The luminous, hard emission of these stars has implications for the study of Galactic massive star formation in the X-ray band. Emitting  $\sim 10^{31.5}$  ergs  $s^{-1}$  above 5 keV, such stars can be detected in reasonable *Chandra* exposures anywhere in our half of the Galactic disk, even if they lie behind several spiral arms and are embedded in dense molecular clouds; they can even be studied in the Magellanic Clouds. Recently studied examples have been found in the MSFRs NGC 6231, NGC 3576, Wd 1, W3, W51A, and R136 in 30 Doradus (Sana et al. 2006; Townsley 2006c; Skinner et al.

2006; Townsley et al. 2005, 2006b).

### 5.3. Possible new OB stars

*Chandra* data have the potential for identifying new OB stars in MSFRs, either in the rich clusters illuminating HII regions or deeply embedded in the surrounding molecular cloud. Recent *Chandra* studies of RCW 38 and NGC 6357 have identified 31 and 24 candidate new OB stars, respectively (Wolk et al. 2006; Wang et al. 2006). Such stars are bright in the NIR and already appear in IR catalogs, but cannot be easily distinguished from reddened field stars (e.g. red giants, which are generally X-ray faint) without X-ray study.

Jiang et al. (2002) find about 1000 OB candidates from IR photometry, but many of those are likely foreground or background stars. X-ray emission should help to discriminate interlopers from M17 OB stars. In Table 6, we narrow these candidates to 143 X-ray selected sources that have masses  $> 2 M_{\odot}$  based on the NIR color-magnitude diagram in Figure 6. Twenty-nine of these are known OB stars from Tables 8 or 9, but the remaining 114 sources are candidate massive stars. Two of these sources, #51 and #163 (marked in Figure 6), appear to be previously unremarked highly obscured O stars with  $A_V \sim 40$ . Spectroscopy of these OB candidates is warranted to confirm their spectral types.

Two alternative indicators of candidate OB stars have been employed (e.g. Wang et al. 2006): high X-ray luminosity, and X-ray detection coupled with bright *K*-band magnitude. There are just four X-ray sources (described below) in our sample with  $\log L_{t,c} > 32.0$  ergs  $s^{-1}$  that are not known O stars (Tables 8 or 9); none of them appears in our list of candidate protostars (Table 7).

**ACIS #187 ( $\Leftrightarrow$  B335)** This source, located in the South Bar, appears in Table 6, where it is estimated to be an early B star ( $M \sim 11 M_{\odot}$ ). No X-ray variability is seen. Its X-ray luminosity and spectral characteristics are similar to the known B2 star CEN 85 ( $\Leftrightarrow$  ACIS #466), so it is plausibly a new high-mass M17 star.

**ACIS #230** This source is located near the top of the ACIS field, west of M17 North. It shows no X-ray variability and its IR colors do not imply that it is massive. Its X-ray spectral parameters are essentially identical to #187 and #466, however, suggesting that it too may be massive.

**ACIS #396** Ranking by detected counts, this source is the second brightest X-ray source in the field, located in the South Bar near the HII region interface. It is not listed as a bright NIR source, but IR photometry can be affected by nebular emission. Its X-ray lightcurve is classified as “definitely variable” but this variability is not flare-like. This hard X-ray source is equally well fit by a very hard thermal plasma ( $kT > 10$  keV, Figure 12f) or a power law with photon index  $\Gamma = 1.55$ ; both fits give the same absorption and flux. Although its NIR colors do not indicate a massive star, this source’s X-ray characteristics are similar to the most massive stars in M17. Its flat X-ray spectrum could indicate that it is a bright AGN, but its location near the ionization front argues against that interpretation.

**ACIS #655 ( $\Leftrightarrow$  B148)** This source, located near the center of NGC 6618 (unfortunately in a chip gap), is quite faint for most of the observation, but exhibits the strongest flare in the whole sample (see Figure 3). This “superflare” behavior has been seen in low-mass stars in several star-forming regions (e.g., Grosso et al. 2004; Wang et al. 2006; Getman et al. 2006a; Favata et al. 2005). From Table 6, source #655 is estimated to be an intermediate-mass star ( $M \sim 2 M_{\odot}$ ), suggesting that the flare may

be from an unresolved lower-mass companion. It is unlikely that source #655 is a new high-mass member of M17.

The final indicator of OB candidacy that we consider—X-ray detection coupled with bright ( $K < 10$ )  $K$ -band magnitude—produces 28 candidates. Seventeen of these are known massive stars and two are likely foreground stars: #281  $\Leftrightarrow$  B293  $\Leftrightarrow$  CEN 7 (spectral type F8) and #854  $\Leftrightarrow$  TYC 6265-1977-1 (spectral type G with large parallax). ACIS #600 ( $\Leftrightarrow$  B 163) is listed by Hanson, Howarth, & Conti (1997) as a candidate young stellar object. The remaining sources are ACIS #1, 9, 35, 402, 650, 698, 852, and 875, widely distributed across the ACIS field of view. These are all listed in Table 6.

#### 5.4. Protoplanetary Disks Around Higher-Mass M17 Stars

As discussed in §1 and Feigelson et al. (2006), X-ray surveys of young stellar populations give samples that are largely unbiased with respect to the presence or absence of protoplanetary disks. They thus provide an unusual opportunity to study disk evolution in coeval populations. Here we address this issue in a restricted fashion, considering only inner disks revealed through a color excess in  $JHK$  photometry (§2.4.2) arising from their heated inner edges; such disks are present mainly in actively accreting Class I and II young stellar systems. Our analysis is insensitive to centrally-cleared, outer disks emitting only at longer wavelengths.

The stellar population we consider here is our X-ray-selected sample of intermediate- and high-mass stars (Table 6 in §2.4.2). This X-ray sample is not complete even for the 1 Myr old NGC 6618 population. Table 6 is missing disk/envelope evolutionary classifications for some known massive stars (e.g. the O4+O4 binary) due to imperfections in the  $JHK$  photometry (§2.4.2). Half of the cataloged early B stars in the NGC 6618 cluster are undetected (§5) in X-rays, and a larger fraction of late-B stars will be missing. Our shallow X-ray data miss much of the massive population just now forming and thought to possess disks, e.g. many of the high-mass Class I sources studied by Nielbock et al. (2001) and Hoffmeister et al. (2006), M17-SO1 (Chini et al. 2004b), and CEN 92 (Chini et al. 2005). Despite this incompleteness, our X-ray sample of higher mass stars in the coeval NGC 6618 population should be largely unbiased with respect to the presence of inner disks.

Our sample thus consists of the 138 stars in Table 6 with disk/envelope evolutionary classifications. A remarkably low fraction (12%, or 16/138) are designated Class I or Class II, indicating  $K$ -band excesses consistent with inner disks. A similar result emerged from the recent *Chandra* study of the rich Pismis 24 cluster illuminating the NGC 6357 HII region, where the X-ray selected NIR Class III:II ratio was  $\sim 25:1$  among intermediate-mass stars (Wang et al. 2006). Considering that the NGC 6618 cluster is thought to be only  $\sim 1$  Myr old (§1), we infer that the inner disks around its more massive stars evolved very rapidly. A similar conclusion was reached by Hillenbrand et al. (1993) and Hernández et al. (2005) in their studies of young stellar clusters with many disk-free intermediate-mass stars. It also suggests that studies of nearby accreting Herbig Ae/Be disks with strong NIR emission (Waters & Waelkens 1998) may characterize only a small fraction of the underlying population of coeval stars. Disk-free stars are often missing from IR-selected catalogs of pre-main sequence populations.

## 6. Summary

Extended X-ray emission had been detected from the M 17 HII region by the *Einstein*, *ROSAT*, and *ASCA* X-ray observatories since the 1980s, but the finding had not been reported until the *Chandra X-ray Observatory* revealed a wealth of morphological detail. Our earlier study focused on the outflowing 10 MK plasma attributed to shocked O star winds (TFM03), while the present study concentrates on the stellar population. In a 40 ks ACIS-I exposure obtained in 2002, we find 886 unresolved X-ray sources with a wide range of intrinsic X-ray luminosities ( $L_{h,c} \simeq 10^{28}$  to almost  $10^{33}$  erg s $^{-1}$  in the hard 2 – 8 keV band) and absorptions (column densities  $N_H < 10^{20}$  to  $10^{24}$  cm $^{-2}$ ). Nearly 90% of the sources have counterparts in NIR (2MASS, SIRIUS) or MIR (*Spitzer* GLIMPSE) images; the remaining sources are divided between background contaminants and newly discovered members of the cloud population. With *Chandra*, the identification of X-ray sources with individual stars is unambiguous (median offset 0.24'' from NIR sources) except for components of multiple systems.

The spatial distribution of X-ray stars suggests a more complex morphology of star formation than is generally discussed from optical- and IR-derived surveys. In addition to the central NGC 6618 cluster and three well-studied embedded groupings (M17-UC1, KWO, and M17-North), we find evidence for a new embedded cluster (designated M17-X) located 4' (2 pc) north-northwest of NGC 6618 (Figure 7b). A 5'-long arc of several dozen X-ray stars along the interface between the M17 HII region and the M17-SW molecular cloud core is clearly traced, delineating recently triggered star formation and confirming the similar structure seen in NIR by Jiang et al. (2002). Substructures on scales of 0.1 pc are seen both within the central NGC 6618 cluster and in the embedded populations. These suggest that the populations are dynamical and young, and that equilibrium has not been reached. Our data support the argument of Jiang et al. (2002) and others for widely distributed star formation that is not concentrated into clusters. This is seen in both the heavily and lightly obscured X-ray populations.

We use our detailed knowledge of the Orion Nebula Cluster population and XLF to calibrate the observed XLF of the ACIS M17 field. The inferred total population of heavily obscured stars is 5000 – 7000 down to 0.1 M $_{\odot}$ , outnumbering the lightly obscured ( $A_V \lesssim 10$  mag) population of 2500 – 3500 stars which are mostly concentrated in the central NGC 6618 cluster. These values are consistent with the  $\sim 3600$  Class I-III young stars counted by Jiang et al. (2002) in their NIR survey sensitive to  $K < 19$  mag.

Forty percent of the ACIS sources are heavily obscured, defined here by median energy  $E_{median} > 2.5$  keV which is roughly equivalent to  $A_V > 10$  mag. Concentrations of 10 – 20 sources are seen around each of the three well-studied star formation subregions in the field: IRS 5/UC1, the KWO, and M17-North. Some high- $L_{IR}$ , high-mass embedded sources are detected in X-rays (e.g. IRS 5S and Anon 1 near M17-UC1, IRS 2, CEN 31, IRS 15), but others are not (the KWO, M17-SO1, CEN 92). The situation for the most famous embedded objects is complicated: IRS 5N which ionized M17-UC1 is only tentatively detected with  $< 5$  photons; the KWO Herbig Be star is undetected but a nearby member of the KWO cluster is seen.

A much greater number of heavily obscured stars are seen outside of the three known concentrations. Many are located in the North Bar and South Bar where the HII region ionization front is propagating into the cloud, but others appear in more distant molecular cloud cores or distributed more-or-less uniformly across the field. At our current completeness limit for heavily obscured stars (roughly estimated in §3.2 as  $\log L_{h,c} \gtrsim 30.9$  ergs s $^{-1}$ ), only the tip of the embedded XLF is detected. An upcoming deeper *Chandra* observation should identify hundreds more heavily obscured stars and elucidate any clustering patterns of the embedded stellar population.

All of the cataloged O stars but only half of the cataloged early B stars (B0–B3) in the field are detected in this short 40 ks ACIS exposure. These OB stars show intrinsic X-ray luminosities consistent with the long-standing  $L_x \propto 10^{-7} L_{bol}$  relationship, with scatter similar to that found for the NGC 6357, NGC 6231, and Orion Nebula Cluster populations.

Only the O4+O4 binary components, which are resolved at 1.8'' separation, are very X-ray luminous, emitting  $\sim 2 \times 10^{33}$  ergs s<sup>-1</sup> in the total band, 20 – 30% of which appears in the penetrating hard band. Although there is no evidence for a shock between the winds from the two resolved components, each component itself exhibits remarkably hard thermal plasma emission even harder than that usually seen in colliding wind binaries. This suggests that Kleinmann’s Anonymous Star may be a system of at least 4 massive stars, two pairs of colliding-wind binaries both with extraordinary wind and/or magnetic properties.

Many B stars have X-ray luminosities scattered in the  $29 < \log L_t < 31$  ergs s<sup>-1</sup> range, overlapping the low-mass pre-main sequence XLF. Most of these stars are thus not readily distinguished from lower mass stars in the X-ray band and, not infrequently, the emission likely comes from a low-mass companion. Many likely new OB stars are found by the association of *Chandra* sources with NIR sources.

Our final result concerns the frequency of inner protoplanetary disks around the X-ray selected high- and intermediate-mass stars. X-ray selection is effective in establishing the underlying population of these stars in a disk-unbiased fashion. We find that only  $\sim 10$ –15% of NGC 6618’s OBA stars have disks with *K*-band excesses.

We appreciate several helpful comments from the anonymous referee. Support for this work was provided to Gordon Garmire, the ACIS Principal Investigator, by the National Aeronautics and Space Administration (NASA) through NASA Contract NAS8-38252 and *Chandra* Contract SV4-74018 issued by the *Chandra X-ray Observatory* Center, which is operated by the Smithsonian Astrophysical Observatory for and on behalf of NASA under Contract NAS8-03060. This publication makes use of data products from the Two Micron All Sky Survey, which is a joint project of the University of Massachusetts and the Infrared Processing and Analysis Center/California Institute of Technology, funded by NASA and the National Science Foundation. This work is based in part on observations made with the *Spitzer Space Telescope*, which is operated by the Jet Propulsion Laboratory, California Institute of Technology under a contract with NASA. This publication makes use of data products from the *Midcourse Space Experiment*. This research made use of the SIMBAD database and VizieR catalogue access tool, operated at CDS, Strasbourg, France. We would have been lost without the invaluable tools of NASA’s Astrophysics Data System, and without CIAO, XSPEC, and ds9.

*Facilities:* CXO (ACIS).

### A. Estimation of Matching Reliability

Because the SIRIUS, 2MASS, and GLIMPSE catalogs have far more entries than our X-ray catalog, some of the associations between X-ray and IR sources reported in Table 5 are expected to be false positives, i.e. false associations found by chance positional coincidence. To estimate the number of false positives expected when matching to a specific IR catalog, it is useful to view the X-ray catalog as a mixture of two populations: an “associated population” of X-ray sources where a “true” counterpart **does** exist in the IR catalog, and an “isolated population” of X-ray sources where **no** counterpart exists.

We can easily simulate the behavior of the matching algorithm for the isolated population by applying

an offset between the catalogs, running the algorithm, and tabulating the results. The offset must be large enough to “break” all the true associations, but excessive offsets should be avoided in order to preserve the relative spatial distributions of the two catalogs. We interpret the matches produced by this simulation as “false positives.” We refer to the X-ray sources which (correctly) did not produce matches as “true negatives.”

With slightly more effort we can simulate the behavior of the matching algorithm for the associated population by creating a “fake” IR counterpart for each X-ray source, running the algorithm, and tabulating the results. Each fake IR position is randomly offset from the corresponding X-ray position by sampling the appropriate offset distribution, taken to be Gaussian with variance equal to the sum of that source’s X-ray position variance and an IR position variance chosen randomly from the IR sources reported in Table 5. We attempt to eliminate the actual associations from the IR catalog by removing the counterparts reported in Table 5. We also randomly offset the catalogs as described above because the “background” population in the IR catalog may be suppressed in the regions around the pruned sources (due to observational limitations). We interpret the matches produced by this simulation as falling into two categories: “correct matches” to the fake entry we created, and “incorrect matches” to some other source which lies closer by chance. We refer to the X-ray sources which (incorrectly) did not produce matches as “false negatives.”

By repeating the simulations many times, we estimate the probabilities of each of the five match types described above. These probabilities, reported in Table 10, can be used to characterize Table 5 only if we can estimate the true mixture ratio between the isolated and associated populations, i.e. the number of X-ray sources having no counterparts (thus susceptible to falsely matching the background IR sources) vs. the number of X-ray sources having true counterparts (thus susceptible to only those background IR sources that lie closer than the true match). We estimate the “associated fraction” for each catalog ( $f_{A_{2MASS}}$ ,  $f_{A_{SIRIUS}}$ ,  $f_{A_{GLIMPSE}}$ ) by considering the number of X-ray sources for which no match was reported in Table 10 (410 for 2MASS, 159 for SIRIUS, 662 for GLIMPSE). Those “negative” matches are a mixture of the true negative and false negative match types in the simulations (columns 4 and 5 in Table 10):

$$\begin{aligned} 410 &= 7.6 f_{A_{2MASS}} + 865.5 (1 - f_{A_{2MASS}}) \\ 159 &= 7.6 f_{A_{SIRIUS}} + 739.2 (1 - f_{A_{SIRIUS}}) \\ 662 &= 8.8 f_{A_{GLIMPSE}} + 861.6 (1 - f_{A_{GLIMPSE}}) \end{aligned}$$

Table 10. Simulations of matching algorithm

Catalog (1)	Associated Population			Isolated Population	
	Correct Matches (2)	Incorrect Matches (3)	False Neg. (4)	True Neg. (5)	False Pos. (6)
2MASS	874.2	4.2	7.6	865.6	20.4
SIRIUS	849.9	28.5	7.6	739.2	146.8
GLIMPSE	872.7	4.6	8.8	861.6	24.4

Note. — **Columns 2–4:** Expected number of population (1) match types. **Columns 5–6:** Expected number of population (2) match types.

After solving for these associated fractions ( $f_{A_2MASS} = 0.53$ ,  $f_{ASIRIUS} = 0.79$ ,  $f_{AGLIMPSE} = 0.23$ ), we can characterize the expected flaws in Table 5. For example, the expected number of reported matches which are wrong is estimated as a weighted sum of “incorrect matches” from the associated population plus “false positives” from the isolated population:

$$\begin{aligned} 4.2 f_{A_2MASS} &+ 20.4 (1 - f_{A_2MASS}) &= 12 &(2.5\%) \\ 28.5 f_{ASIRIUS} &+ 146.8 (1 - f_{ASIRIUS}) &= 53 &(7\%) \\ 4.6 f_{AGLIMPSE} &+ 24.4 (1 - f_{AGLIMPSE}) &= 20 &(9\%) \end{aligned}$$

Note that these are averages across the catalog; the reliability of individual matches is complex since it depends on both the position uncertainties (e.g. larger uncertainties lead to larger matching “footprints” which have larger susceptibility to spurious matches) and on the local density of IR sources (e.g. crowded regions are more likely to generate spurious matches).

## REFERENCES

- Allen, L. E., Hora, J. L., Megeath, S. T., Deutsch, L. K., Fazio, G. G., Chavarria, L., & Dell, R. W. 2005, in IAU Symp. 227, Massive Star Birth: A Crossroads of Astrophysics, ed. R. Cesaroni et al. (Cambridge: Cambridge Univ. Press), 352
- Arnaud, K. A. 1996, in ASP Conf. Ser. 101, Astronomical Data Analysis Software and Systems V, ed. G. H. Jacoby & J. Barnes (San Francisco:ASP), 17
- Babel, J., & Montmerle, T. 1997, ApJ, 485, L29
- Baraffe, I., Chabrier, G., Allard, F., & Hauschildt, P. H. 1998, A&A, 337, 403
- Berghoefter, T. W., Schmitt, J. H. M. M., Danner, R., & Cassinelli, J. P. 1997, A&A, 322, 167
- Bessell, M. S., & Brett, J. M. 1988, PASP, 100, 1134
- Broos, P. S., Townsley, L. K., Getman, K., & Bauer, F. E. 2002, ACIS Extract, An ACIS Point Source Extraction Package (University Park: The Pennsylvania State Univ.) [http://www.astro.psu.edu/xray/docs/TARA/ae\\_users\\_guide.html](http://www.astro.psu.edu/xray/docs/TARA/ae_users_guide.html)
- Bumgardner, T. E. 1992, M.S. thesis, Ohio State Univ., Columbus
- Cardelli, J. A., Clayton, G. C., & Mathis, J. S. 1989, ApJ, 345, 245
- Cash, W. 1979, ApJ, 228, 939
- Chen, W., & White, R. L. 1991, ApJ, 366, 512
- Chlebowski, T., Harnden, F. R., Jr., & Sciortino, S. 1989, ApJ, 341, 427
- Chini, R., Elsaesser, H., & Neckel, T. 1980, A&A, 91, 186
- Chini, R. & Wargau, W. F. 1998, A&A, 329, 161
- Chini, R., Nielbock, M., & Beck, R. 2000, A&A, 357, L33

- Chini, R., Hoffmeister, V. H., Kämpgen, K., Kimeswenger, S., Nielbock, M., & Siebenmorgen, R. 2004a, *A&A*, 427, 849
- Chini, R., Hoffmeister, V., Kimeswenger, S., Nielbock, M., Nürnberger, D., Schmidtobreck, L., & Sterzik, M. 2004b, *Nature*, 429, 155
- Chini, R., Hoffmeister, V. H., Nielbock, M., Scheyda, C. M., Nürnberger, D., Feigelson, E. D., Getman, K., & Townsley, L. K. 2005, in *IAU Symp. 227, Massive Star Birth: A Crossroads of Astrophysics*, ed. R. Cesaroni et al. (Cambridge: Cambridge Univ. Press), 145
- Chini, R., Hoffmeister, V. H., Nielbock, M., Scheyda, C. M., Steinacker, J., Siebenmorgen, R., Nürnberger, D. 2006, *ApJ*, 645, L61
- Churchwell, E., et al. 2004, *ApJS*, 154, 322
- Corbelli, E., Palla, F., & Zinnecker, H. 2005, *The Initial Mass Function 50 Years Later*, *Astrophysics & Space Science Library Volume 327* (Dordrecht: Springer)
- Corcoran, M. F., et al. 2004, *ApJ*, 613, 381
- de Jager, C., & Nieuwenhuijzen, H. 1987, *A&A*, 177, 217
- Elias, J. H., Frogel, J. A., Matthews, K., & Neugebauer, G. 1982, *AJ*, 87, 1029
- Elmegreen, B. G., & Lada, C. J. 1977, *ApJ*, 214, 725
- Elmegreen, B. G., Lada, C. J., & Dickinson, D. F. 1979, *ApJ*, 230, 415
- Ezoe, Y., Kokubun, M., Makishima, K., Sekimoto, Y., & Matsuzaki, K. 2006, *ApJ*, 638, 860
- Favata, F., Flaccomio, E., Reale, F., Micela, G., Sciortino, S., Shang, H., Stassun, K. G., & Feigelson, E. D. 2005, *ApJS*, 160, 469
- Feigelson, E. D., & Montmerle, T. 1999, *ARA&A*, 37, 363
- Feigelson, E. D., Broos, P., Gaffney, J. A., Garmire, G., Hillenbrand, L. A., Pravdo, S. H., Townsley, L., & Tsuboi, Y. 2002, *ApJ*, 574, 258
- Feigelson, E. D., & Getman, K. V. 2005, in *Astrophysics & Space Science Library Volume 327, The Initial Mass Function: 50 Years Later*, ed. E. Corbelli, F. Palla, & H. Zinnecker (Dordrecht: Springer), 163
- Feigelson, E. D., et al. 2005, *ApJS*, 160, 379
- Feigelson, E., Townsley, L., Gudel, M., & Stassun, K. 2006, in *Protostars & Planets V*, ed. B. Reipurth et al. (Tucson: Univ. Arizona Press), in press (astro-ph/0602603)
- Felli, M., Massi, M., & Churchwell, E. 1984, *A&A*, 136, 53
- Flaccomio, E., Micela, G., & Sciortino, S. 2006, *A&A*, 455, 903
- Freeman, P. E., Kashyap, V., Rosner, R., & Lamb, D. Q. 2002, *ApJS*, 138, 185
- Gagné, M., Oksala, M. E., Cohen, D. H., Tonnesen, S. K., ud-Doula, A., Owocki, S. P., Townsend, R. H. D., & MacFarlane, J. J. 2005, *ApJ*, 628, 986

- Getman, K. V., Feigelson, E. D., Grosso, N., McCaughrean, M. J., Micela, G., Broos, P., Garmire, G., & Townsley, L. 2005a, *ApJS*, 160, 353
- Getman, K. V., et al. 2005b, *ApJS*, 160, 319
- Getman, K. V., Feigelson, E. D., Townsley, L., Broos, P., Garmire, G., & Tsujimoto, M. 2006a, *ApJS*, 163, 306
- Getman, K. V., Feigelson, E. D., Garmire, G., Broos, P., & Wang, J. 2006b, *ApJ*, submitted (astro-ph/0607006)
- Grosso, N., Montmerle, T., Feigelson, E. D., & Forbes, T. G. 2004, *A&A*, 419, 653
- Grosso, N., et al. 2005, *ApJS*, 160, 530
- Hanson, M. M., Howarth, I. D., & Conti, P. S. 1997, *ApJ*, 489, 698
- Hartmann, L., Megeath, S. T., Allen, L., Luhman, K., Calvet, N., D'Alessio, P., Franco-Hernandez, R., & Fazio, G. 2005, *ApJ*, 629, 881
- Henning, T., Klein, R., Launhardt, R., Lemke, D., & Pfau, W. 1998, *A&A*, 332, 1035
- Hernández, J., Calvet, N., Hartmann, L., Briceño, C., Sicilia-Aguilar, A., & Berlind, P. 2005, *AJ*, 129, 856
- Hillenbrand, L. A., Massey, P., Strom, S. E., & Merrill, K. M. 1993, *AJ*, 106, 1906
- Hobson, M. P., Padman, R., Scott, P. F., Prestage, R. M., & Ward-Thompson, D. 1993, *MNRAS*, 264, 1025
- Hoffmeister, V. H., Chini, R., Scheyda, C. M., Nürnberger, D., Vogt, N., & Nielbock, M. 2006, *A&A*, 457, L29
- Hong, J., van den Berg, M., Schlegel, E. M., Grindlay, J. E., Koenig, X., Laycock, S., & Zhao, P. 2005, *ApJ*, 635, 907
- Imanishi, K., Koyama, K., & Tsuboi, Y. 2001, *ApJ*, 557, 747
- Isobe, T., Feigelson, E. D., & Nelson, P. I. 1986, *ApJ*, 306, 490
- Jardine, M., Cameron, A. C., Donati, J.-F., Gregory, S. G., & Wood, K. 2006, *MNRAS*, 367, 917
- Jiang, Z. et al. 2002, *ApJ*, 577, 245
- Johnson, C. O., Depree, C. G., & Goss, W. M. 1998, *ApJ*, 500, 302
- Klein, R., Henning, T., & Cesarsky, D. 1999, *A&A*, 343, L53
- Kleinmann, D. E. 1973, *Astrophys. Lett.*, 13, 49
- Kleinmann, D. E. & Wright, E. L. 1973, *ApJ*, 185, L131
- Kraemer, K. E., Shipman, R. F., Price, S. D., Mizuno, D. R., Kuchar, T., & Carey, S. J. 2003, *AJ*, 126, 1423
- Lada, C. J. 1987, in *IAU Symp. 115, Star Forming Regions*, ed. M. Peimbert & J. Jugaku (Dordrecht: D. Reidel Publishing Co.), 1
- Lada, C. J., Depoy, D. L., Merrill, K. M., & Gatley, I. 1991, *ApJ*, 374, 533

- Lada, C. J., & Adams, F. C. 1992, *ApJ*, 393, 278
- Lucy, L. B., & White, R. L. 1980, *ApJ*, 241, 300
- Martins, F., Schaerer, D., & Hillier, D. J. 2005, SF2A-2005: Semaine de l’Astrophysique Francaise, 633
- Massi, M., Felli, M., & Churchwell, E. 1988, *A&A*, 194, 116
- Meixner, M., Haas, M. R., Tielens, A. G. G. M., Erickson, E. F., & Werner, M. 1992, *ApJ*, 390, 499
- Meyer, M. R., Calvet, N., & Hillenbrand, L. A. 1997, *AJ*, 114, 288
- Morrison, R., & McCammon, D. 1983, *ApJ*, 270, 119
- Muno, M. P., Bauer, F. E., Bandyopadhyay, R. M., & Wang, Q. D. 2006a, *ApJS*, 165, 173
- Muno, M. P., Law, C., Clark, J. S., Dougherty, S. M., de Grijs, R., Portegies Zwart, S., & Yusef-Zadeh, F. 2006b, *ApJ*, 650, 203
- Nielbock, M., Chini, R., Jütte, M., & Manthey, E. 2001, *A&A*, 377, 273
- Norris, R. P., Caswell, J. L., Gardner, F. F., & Wellington, K. J. 1987, *ApJ*, 321, L159
- Ogura, K. & Ishida, K. 1976, *PASJ*, 28, 35
- Owocki, S. P., & Cohen, D. H. 1999, *ApJ*, 520, 833
- Pallavicini, R., Golub, L., Rosner, R., Vaiana, G. S., Ayres, T., & Linsky, J. L. 1981, *ApJ*, 248, 279
- Pollock, A. M. T., Corcoran, M. F., Stevens, I. R., & Williams, P. M. 2005, *ApJ*, 629, 482
- Preibisch, T. 2004, *A&A*, 428, 569
- Preibisch, T., et al. 2005a, *ApJS*, 160, 401
- Preibisch, T., et al. 2005b, *ApJS*, 160, 582
- Preibisch, T., & Feigelson, E. D. 2005, *ApJS*, 160, 390
- Rakowski, C. E., Schulz, N. S., Wolk, S. J., & Testa, P. 2006, *ApJ*, 649, L111
- Reale, F., Peres, G., & Orlando, S. 2001, *ApJ*, 557, 906
- Rebull, L. M., Stauffer, J. R., Ramirez, S. V., Flaccomio, E., Sciortino, S., Micela, G., Strom, S. E., & Wolff, S. C. 2006, *AJ*, 131, 2934
- Reid, M. A., & Wilson, C. D. 2006, *ApJ*, 644, 990
- Rieke, G. H., & Lebofsky, M. J. 1985, *ApJ*, 288, 618
- Sako, S., et al. 2005, *Nature*, 434, 995
- Sana, H., Rauw, G., Naze, Y., Gosset, E., & Vreux, J.-M. 2006, *MNRAS*, 372, 661
- Schulz, A., Lenzen, R., Schmidt, T., & Proetel, K. 1981, *A&A*, 95, 94
- Schulz, N. S., Canizares, C., Huenemoerder, D., & Tibbets, K. 2003, *ApJ*, 595, 365

- Schulz, N. S., Testa, P., Huenemoerder, D. P., Ishibashi, K., & Canizares, C. R. 2006, *ApJ*, in press (astro-ph/0608420)
- Siess, L., Dufour, E., & Forestini, M. 2000, *A&A*, 358, 593
- Smith, R. K., Brickhouse, N. S., Liedahl, D. A., & Raymond, J. C. 2001, *ApJ*, 556, L91
- Skinner, S. L., Zhekov, S. A., Güdel, M., & Schmutz, W. 2002, *ApJ*, 572, 477
- Skinner, S. L., Zhekov, S. A., Palla, F., & Barbosa, C. L. D. R. 2005, *MNRAS*, 361, 191
- Skinner, S. L., Simmons, A. E., Zhekov, S. A., Teodoro, M., Damineli, A., & Palla, F. 2006, *ApJ*, 639, L35
- Smith, M. A., Cohen, D. H., Gu, M. F., Robinson, R. D., Evans, N. R., & Schran, P. G. 2004, *ApJ*, 600, 972
- Smith, M. A., & Balona, L. 2006, *ApJ*, 640, 491
- Stelzer, B., Flaccomio, E., Montmerle, T., Micela, G., Sciortino, S., Favata, F., Preibisch, T., & Feigelson, E. D. 2005, *ApJS*, 160, 557
- Stelzer, B., Micela, G., Hamaguchi, K., & Schmitt, J. H. M. M. 2006, *A&A*, 457, 223
- Testi, L., Felli, M., Persi, P., & Roth, M. 1998, *A&AS*, 129, 495
- Townsley, L. K., Broos, P. S., Nousek, J. A., & Garmire, G. P. 2001, *Nuclear Instr. & Methods*, 486, 751
- Townsley, L. K., Feigelson, E. D., Montmerle, T., Broos, P. S., Chu, Y.-H., & Garmire, G. P. 2003, *ApJ*, 593, 874
- Townsley, L. K., Broos, P. S., Feigelson, E. D., & Garmire, G. P. 2005, in *IAU Symp. 227, Massive Star Birth: A Crossroads of Astrophysics*, ed. R. Cesaroni et al. (Cambridge: Cambridge Univ. Press), 297
- Townsley, L. K., Broos, P. S., Feigelson, E. D., Brandl, B. R., Chu, Y.-H., Garmire, G. P., & Pavlov, G. G. 2006a, *AJ*, 131, 2140
- Townsley, L. K., Broos, P. S., Feigelson, E. D., Garmire, G. P., & Getman, K. V. 2006b, *AJ*, 131, 2164
- Townsley, L. K. 2006c, in *Proc. of the STScI May Symposium, Massive Stars: From Pop III and GRBs to the Milky Way*, ed. M. Livio (Cambridge: Cambridge Univ. Press), (astro-ph/0608173)
- Tsujimoto, M., Kobayashi, N., & Tsuboi, Y. 2005, *AJ*, 130, 2212
- Tsujimoto, M., Hosokawa, T., Feigelson, E. D., Getman, K. V., & Broos, P. 2006, *ApJ*, accepted
- Tsunemi, H., Mori, K., Miyata, E., Baluta, C., Burrows, D. N., Garmire, G. P., & Chartas, G. 2001, *ApJ*, 554, 496
- ud-Doula, A., Townsend, R. H. D., & Owocki, S. P. 2006, *ApJ*, 640, L191
- Vallee, J. P. & Bastien, P. 1996, *A&A*, 313, 255
- van Dyk, D. A., Connors, A., Kashyap, V. L., & Siemiginowska, A. 2001, *ApJ*, 548, 224
- Volk, K., Kwok, S., Stencel, R. E., & Brugel, E. 1991, *ApJS*, 77, 607
- Wachter, K., Leach, R., & Kellogg, E. 1979, *ApJ*, 230, 274

- Waldron, W. L., & Cassinelli, J. P. 2001, *ApJ*, 548, L45
- Wang, J., Townsley, L., Feigelson, E. D., Getman, K. V., Broos, P., Garmire, G. P., & Tsujimoto, M. 2006, *ApJS*, submitted
- Waters, L. B. F. M., & Waelkens, C. 1998, *ARA&A*, 36, 233
- Weisskopf, M. C., Brinkman, B., Canizares, C., Garmire, G., Murray, S., & Van Speybroeck, L. P. 2002, *PASP*, 114, 1
- Wilson, T. L., Hanson, M. M., & Muders, D. 2003, *ApJ*, 590, 895
- Wolk, S. J., Harnden, F. R., Flaccomio, E., Micela, G., Favata, F., Shang, H., & Feigelson, E. D. 2005, *ApJS*, 160, 423
- Wolk, S. J., Spitzbart, B. D., Bourke, T. L., & Alves, J. 2006, *AJ*, 132, 1100
- Zacharias, N., Urban, S. E., Zacharias, M. I., Wycoff, G. L., Hall, D. M., Monet, D. G., & Rafferty, T. J. 2004, *AJ*, 127, 3043